POLITECNICO DI MILANO
SCHOOL OF CIVIL AND ENVIRONMENTAL ENGINEERING

MASTER OF SCIENCE IN CIVIL ENGINEERING

MASTER THESIS

AN EXPERIMENTAL STUDY ON BLASTFURNACE SLAG ACTIVATED WITH QUICKLIME AND MAGNESIA

Andrea CAVALLARI
ID: 928093

ADVISOR:
Prof. Liberato FERRARA

CO-ADVISORS:
Prof. Aveline DARQUENNES
Prof. Kinda HANNAWI-SALMO

ACADEMIC YEAR 2021/2022

Contents

List of Figures

List of Tables

Sinossi

L'industria del cemento è responsabile del 5-7% delle emissioni artificiali di CO_2 risultando il terzo settore industriale più impattante [15]. Diversi leganti idraulici alternativi o complementari al clinker sono stati studiati e il loro uso è già previsto dalle normative: loppa granulata d'altoforno, fumo di silice, ceneri volanti, pozzolane artificiali e naturali. In particolare i cementi misti clinker-loppa d'altoforno promettono le più alte riduzioni di impatto ambientale perché utilizzano in grande quantità un sottoprodotto della siderurgia che altrimenti dovrebbe essere smaltito come rifiuto industriale [28]

Nella normativa EN 206 l'uso della loppa d'altoforno è previsto in miscela con il clinker [58] in quanto le proprietà idrauliche della loppa sono latenti, cioè per manifestarsi necessitano della presenza di un attivatore alcalino, ruolo rivestito dal clinker [6]. In ottica di totale eliminazione del clinker attivatori come idrossido di sodio e metasilicato di sodio sono stati studiati ma l'interesse è anche caduto su calce e magnesia, prodotti relativamente economici e ampiamente disponibili sul mercato [24]. Il presente lavoro ha testato l'utilizzo di calce in purezza e non, di magnesia, di clinker e di loro miscele come attivatori su provini di malta. Sono stati osservati gli effetti della natura dell'attivatore su lavorabilità, resistenza, rigidezza, porosità, velocità di presa, calore di idratazione, deformazioni da ritiro ed espansione, composizione chimica della pasta idratata. Nel complesso si sono ottenute resistenze a compressione comprese tra 20 e 30 Mpa a 90 giorni di stagionatura e si è verificato che l'uso di MgO può compromettere l'integrità della pasta e la resistenza meccanica.

PAROLE CHIAVE: Gound-Granulated-Blastfurnace-Slag, Alkali-Activated Slag, CaO, MgO

Abstract

Cement industry is the third largest producer of CO_2 being responsible of 5-7% of the world emissions[15]. Many alternative and complementary hydraulic binders have been studied and introduced in the norms: ground-granulated-blastfurnace-slag (GGBFS), silica fume, fly ashes, artificial and natural pozzolanas[58]. In particular BFS-clinker cements have shown tha highest potential of environmental impact reduction because they uses in high quantities a byproduct of metallurgy that otherwise would have to be disposed as industrial waste [28].
In the standard EN206 the use of BFS is proposed together with clinker[58] because the latent hydraulic properties of BFS need the presence of an alkaline activator, as clinker, to occur[6].
The purpose of totally eliminating the use of clinker has lead to the study of other activators as sodium hydroxide and sodium metasylicate but quite recently CaO and MgO, relatively cheap and widely present on the market, have been taken into consideration[24].
The present work focuses on the use of quicklime, magnesia, clinker and their mix to activate BFS in mortar samples. The effects of the nature of the activator have been observed on chemical composition of the hydrated paste, porosity, setting time, hydration heat, delayed deformation, strength and stiffness. In general the achieved compressive strength is between 20 and 30 MPa after 90 days of curing and the fact that the presence of additive MgO can compromise the integrity of the cement paste and the strength has been observed.

KEYWORDS: Gound-Granulated-Blastfurnace-Slag, Alkali-Activated Slag, CaO, MgO

Ringraziamenti

Devo ammettere che questo piccolo paragrafo è sempre il più difficile, forse anche più difficile di compilare codici su codici, fare conti, pensare a come mettere giù i risultati in maniera più chiara e meno pedante possibile per poi finire che non ci capisce nulla neanche il sottoscritto autore di questo testo. Farò quindi uno sforzo di ricordare tutte le persone con cui ho lavorato e quelle che mi sono state vicine un questo impegnativo anno di lavoro di cui questa tesi è il risultato.

Un sincero ringraziamento va alle docenti con cui ho lavorato in Francia: la prof.ssa Aveline Darquennes et la prof.ssa Kinda Hannawi che mi hanno accolto nel gruppo di lavoro con grande gentilezza e disponibilità. Alla pari devo ringraziare i dottorandi e gli altri studenti in stage di ricerca che mi hanno aiutato molto insegnandomi come utilizzare gli strumenti, come interpretare i risultati dei test e con cui ho condiviso consigli e materiale, oltre a preparazioni di base come riempire la bombola di azoto liquido che sta nella sala 16. Grazie mille Lina, Sounean, Fatima, Jousé, Jules, Dalal. Ma soprattutto devo ringraziare Lei che mi ha dedicato una quantità enorme di tempo e di pazienza nonostante il lavoro di un dottorando nel campo dei materiali cementizi sia molto impegnativo. Ti devo veramente tanto, grazie. Un laboratorio non è fatto solo da professori, dottorandi e stagisti, ma anche da tecnici che si occupano delle apparecchiature, sempre pronti ad insegnarne l'utilizzo e dare una mano. Meritate anche voi un grande ringraziamento, Jean-Luc, Jean-Ives, Raphaël, Franc, David, Christian. Poi siete anche simpatici quindi meglio!

I primi mesi di questa esperienza all'estero sono stati tosti a causa delle limitazioni per il covid che in Francia erano molto severe: coprifuoco alle 19 e non si poteva fare niente se non andare al parco e al supermercato. Voglio quindi ringraziare anche voi, perché il vedersi regolarmente per pranzo, un viaggetto fuori porta o le festicciole in residenza mi hanno permesso di finire i primi mesi sano di mente. Grazie mille Matteo, Erfan, Ramin, Amir, Josephine, Zuka, Ana, Shabina, Zihao, Cai, Yang, Sela e Kaisa, vi auguro ogni bene e magari un giorno ci incontreremo di nuovo. Un sincero grazie ai miei amici dell'Insa e gli altri miei compagni di erasmus del Poli, Costantino, Elena e Mohamed con i quali non ci annoiava mai al mitico FOY. Cavolo, come faccio a elencare tutte le persone che ho conosciuto in questo anno di erasmus? Quante saranno? Almeno un centinaio sicuro... Dai, ringrazio tutti in blocco: grazie della compagnia e dei bei momenti ragazzi, vi auguro buona fortuna e soprattutto bevete di meno che la cirrosi epatica è una cosa seria (cit. Michele Luca Favale)!.

Cari parenti, amici, compagni di corso e annessi e connessi, adesso vengo a voi. Spero non vi offendiate se vi ho lasciato per ultimi perché non lo siete affatto per importanza. Comincio con i mitici compagni di corso, grandi amici e compagni di esaurimento nervoso: Pierluigi, Ivan e Cristiana. Grazie per le ospitate, le notti in patio, il soggiorno in Puglia e le tante altre cose che abbiamo condiviso. E finalmente arrivo ai cari vecchi amici di Busto Garolfo di cui ho veramente sentito la mancanza durante la mia permanenza a Rennes: grazie mille per la vostra

amicizia e qualche volta fatevelo un giro in Bretagna che è un così bel posticino!
Il più grande dei ringraziamenti va però alla mia famiglia senza il cui sostegno e grande pazienza non sarei riuscito a concludere questo grande percorso.

Acknowledgements

This thesis is the result of one entire year of working in the laboratory of INSA Rennes, an adventure that have been funny, intersting, stimulating and exhausting at the same time, that made me learn how to manage such complex and long tasks by myself. But I did not succeed in that (or at least I whish!) alone without the help of a lot of people. The first great thanks go to my "French professors", prof. Aveline Darquennes and Kinda Hannawi, who have welcomed me in their research group and taught me a lot, always available to give suggestions. The other students doing PhD and internships help me a lot by explaining how to do manipulations, how to interpret the results of the tests, giving an hand in the preparation of the test material (can anybody help me with the liquid nitrogen please?) or simply sharing the bibliographic material. Fatima, Dalal, Lina, Sounean, Runqi (hope not to have written your name wrong!), Josué, Jules, Véran, thanks a lot. But a special thanks goes to Lei. Man, I have no idea of how much time you have dedicated to me and I owe you a lot, I wish you the best. And I must remember the technicians of the laboratory too that taught me how to use the test machines and helped me in doing some manipulations: Jean-Luc, Jean-Yves, Raphaël, Franck, Christian, David, thanks a lot and hope to see you soon.

The first months of this great adventure have been quite hard because of the covid restrictions that were very tough. Practically the life was limited to the laboratory, the supermarket, the park and the open-air market Saturday morning. Probably I would have become insane if I had not met you, guys. Ana, Zuka, Shabina, Zihao, Cai, Yang, Sela, Matteo, Amir, Erfan, Ramin, Kaisa, thanks a lot for all the good time spent together. Maybe one day we will meet again. Thanks to the other friends that I met at INSA Rennes, both students from my university, Costantino, Elena, Mohamed, INSA itself and from all Europe and the world. Thanks for the lunches and dinner together, the trips with the BEAR Club, the parties in the student dormitory, the FOY and the bars in the city center. And of course all the people that I met in town coming from every part of the world! I am not able to remember everyone because you are really too many. Good luck to everyone and drink less!

Thanks to my classmates that shared their way with me. Pierluigi, Ivan, Cristiana, thanks for your friendship, the nights spent at university, the parties, the nervous breakdowns and many other things that I am not able to remember.

And at last, I thank the most important people of this long and boring list. Without the unconditional support my family this long study period and this great experience abroad would not have been possible. Thanks, eternally.

Chapter 1

Introduction

1.1 The historical development of cements and the current European standard

The standard UNI EN 197-1, the Italian national annex of the standard EN 197-1, defines cement as *an hydraulic binder, i.e. a finely ground inorganic material that, if mixed with water, forms a paste which hardens under the effect of chemical reactions and hydration processes and which, once hardened, keeps its strength and stability even under water.*

Hydraulic binders are being used since very ancient time. Probably the most famous example is the *opus caementicium* used by the ancient Romans which was a mix of extinguished quicklime, pozzolanic ashes or brick powder and water. The study of the hydraulic binders applying the scientific method started in the mid of the 18^{th} century when Smeaton observed that the presence of clay in the limestone has a very important role in providing hydraulic characteristics to the lime. Between 1812 and 1818 Vicat confirmed the assumption made by Smeaton and showed that the hydraulic properties of the lime are due to the combination of quicklime with silica and alumina contained in the clay and that it is possible to produce artificial hydraulic limes from limestone and clay.

After the studies made by Smeaton many tentatives to increase the quantity of clay and the heating temperature were done until Johnson realized, in 1844, that it is necessary to heat at temperature higher than 1400°C to obtain significant improvements in the mechanical performance. The results of the Johnson's experience are nowadays used to distinguish between cements and hydraulic binders: the production process of the first ones reaches a temperature of 1450°C to form the liquid phase rich of tricalcic aluminate and tetracalcic ferroaluminate, for the latter the peak temperature is not enough to form the liquid phase.

The material science has improved a lot after the studies of Vicat reaching a better knowledge of the hardening process of binders. Some of them have *hydraulic properties* because they harden by reacting with water and others have *pozzolanic properties* because they do not react directly with water but with calcium hydroxide, properties that was unknowingly used by the ancient Romans. Nowadays a great variety of cements is available and mixing hydraulic and pozzolanic binders is not uncommon. Furthermore other materials having hardening properties have been discovered and adopted in the engineering practice.

The current European standard EN 197-1 [57] proposes many materials to compose a cement:

- Clinker (K) is the hydraulic binder derived from the heating of limestone and clays according to the experience of Johnson

- GGBFS (S) is a secondary product of primary ferrous metallurgy during which iron ore is produced; it appears as a glassy powder and its hydraulic properties are called *latent* because they need suitable activation

- Silica fume (D) derives from the production of silicon and iron-silicon alloys in electric arch furnaces and it has pozzolanic properties

- Pozzolanas are materials of natural origins, usually volcanic or sedimentary, that reacts with $Ca(OH)_2$ to form calcium-silicate and calcium-aluminate compounds. Pozzolanas can be activated by heat treatment (designation Q in the norm) or used in their natural state (designation P)

- Fly ashes (FA) are obtained by electrostatic or mechanical precipitation of dust-like particles from the flue gases from furnaces fired with pulverised coal. Two types are distinguished: siliceous fly ashes (V) which have pozzolanic properties and calcareous fly ashes (W) which have hydraulic and/or pozzolanic properties

- Burnt shale (T) is specifically burnt oil shale at a temperature of approximately 800°C; it shares some phases in common with the clinker

- Limestone (L, LL) is calcium carbonated that can be mixed with clay and it is essentially inert

- other secondary components

The standard classifies common use cements in 5 categories according to their compositions:

- Portland cements (CEMI) are composed at least the 95% by clinker

- Composite portland cements (CEMII) are a mix of different materials but the dose of clinker is at least 65%, many subclasses are defined according to the mixed phases and their proportions

- Blast furnace cements (CEMIII) contain a quote of granulated blast furnace slag varying between 36 and 95% while the remaining part is clinker; 3 subclasses are defined

- Pozzolanic cements (CEMIV) are a mix of clinker and pozzolanic materials in variable doses; clinker has the function to provide the $Ca(OH)_2$ necessary to the activation of the pozzolanic reaction

- Composite cements (CEMV) are a mix of hydraulic and pozzolanic materials but, differently from the big CEMII family, the dose of clinker is lower than 65%

The standard proposes other designation according to the mechanical strength offered by the cement after 28 days, the hardening velocity and the resistance to sulfate attack.
In the current standard clinker is always present even in small quantities. As previously highlighted the production of clinker reaches very high temperature causing a very large energy consumption; moreover the calcination of limestone produces great quantities of CO_2. For these reasons the production of clinker is very polluting and we have to consider the extraction of resources and the logistic chain specific for cement industry that provoke more pollution.

Blast furnace slag is a promising substitute of clinker because it is able to reach high strength with little clinker doses and it is a waste of metallurgy that would have to be disposed if it was not exploited. The challenge of substituting clinker with blast furnace slag is finding a suitable activator able to provide good mechanical performances and being cheap enough to be economically competitive. Many activators are being studied but the present work will focus on commonly used materials as magnesia (MgO) and quicklime (CaO).

1.2 Industrial production process of clinker, MgO and CaO

The production of cement is an industrial process diffused on a large scale because of the great demand of concrete and mortar as construction materials. As previously said clinker is produced by a dedicated industrial sector while other materials having binding properties are essentially wastes, nowadays called *secondary products* because of their usefulness, of other industrial processes. In this section the production process of clinker, GGBFS, magnesia and quicklime will be described to better understand the cause of the environmental impact of these materials.

1.2.1 The production process of clinker

The production process of ordinary portland cement (OPC) is shown in fig.1.1. Clinker is obtained by limestone ($CaCO_3$) and clay (hydrate-alumina-silicate $xAL_2O_3 \cdot ySiO_2 \cdot zH_2O$ containing some iron-oxydes). The grinding of the raw materials can be done in dry or wet conditions. The powder is then dried, preheated and passed in a cylindrical rotatory kiln having a diameter comprised in general between 3 and 6 m and a length sometimes higher than 100 m. The rotatory kiln is internally covered with refractory materials and has a 3-5% inclination to allow the motion of the material during the slow rotation (1-2 rounds/min). A burner at the end extremity of the kiln and the introduction of air coming from the final cooling phase provide heat to the furnace. As clinker advances through the kiln, the temperature gradually increases until 1450°C which is kept for 15 min. Different chemical reactions reactions take place at different temperature ranges:

- at 100°C free water starts evaporating
- at 500°C the release of chemically bound water in the clay starts
- at 600°C the decomposition of $CaCO_3$ begins and carbon dioxyde is released
- the bicalcic silicate (C_2S) starts forming at 900-1200°C
- at temperature higher than 1250°C the C_2S reacts with quicklime forming the tricalcic-silicate (C_3S)
- in the same range of temperatures the liquid phase composed by tricalcic aluminate and tetracalcic ferroaluminate forms

After the passage in the kiln the material is rapidly cooled with air obtaining the clinker which is mixed with gypsum (maximum 5% in mass) and milled before packaging.

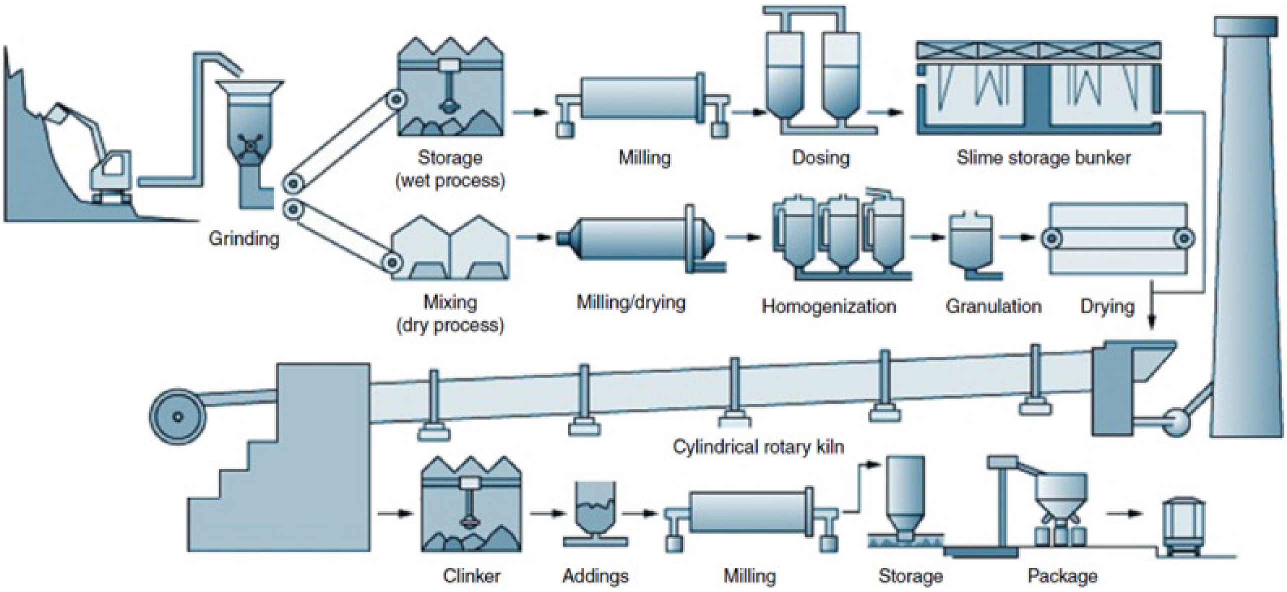

Figure 1.1: Production process of clinker [13]

1.2.2 The production of blast furnace slag

Iron minerals, coke and limestone are introduced in the blast furnace and heated to start the reaction of reduction of iron oxides. Two liquid phases of different density depose at the bottom of the blast furnace: the heaviest one is the iron ore and the higher is the blast furnace slag which are spilled in different circuits. The blast furnace slag is rapidly cooled with water and milled, obtaining the GGBFS.

GGBFS is a white glassy powder formed by calcium, silicon and aluminum oxides. Its chemical structure is not so different from clinker and, thanks to the rapid cooling treatment, GGBFS has hydraulic properties that are latent because it does not react with water if alkaline substances having the role of activator are not present.

The use of GGBFS in high doses provides many advantages like a lower environmental impact, lower porosity of the cement paste and higher resistance to sulfate attack. The new challenge to further improve the environmental impact is fining alternative activator to clinker that could be easily applied to the construction industry.

1.2.3 The production of MgO

Magnesium oxide can be derived from the calcination of magnesite and brucite or the calcination of magnesium hydroxide extracted from seawater.

The extraction of magnesium oxide from seawater or high-magnesium brines is a very complex industrial process that implies the use of a strong base to rise the pH up to the precipitation point of magnesium hydroxide that can be later calcinated to produce MgO.

The calcination of magnesite and brucite is a much simpler process quite similar to the production of clinker but reaching far lower temperatures. Brucite starts decomposing around 350°C, varying because of the presence of impurities, while the decomposition of magnesite at the pressure of 1 atm starts between 402 and 750°C, based on the crystalline form that it can

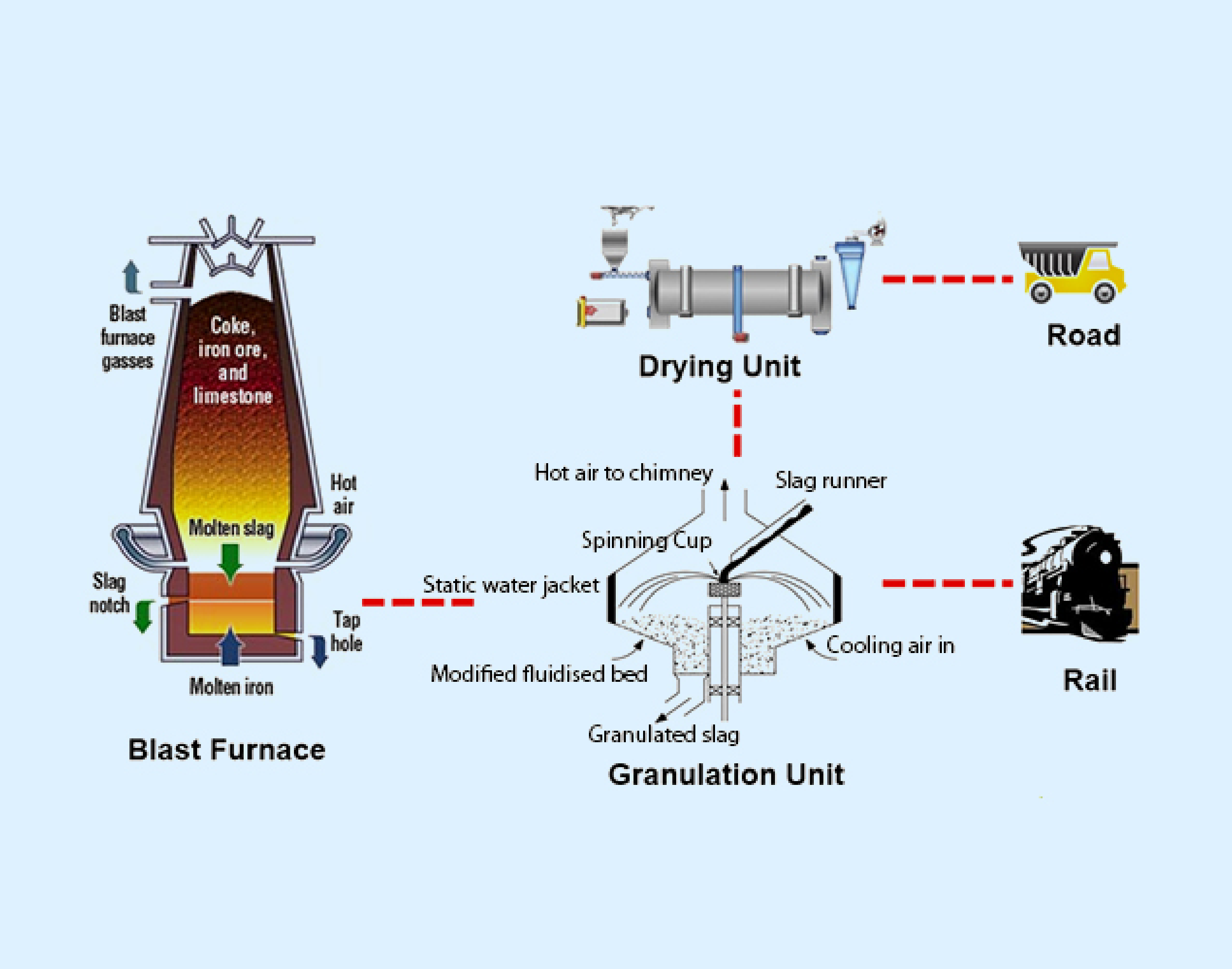

Figure 1.2: Industrial production of GGBFS [47]

present. The decomposition reactions are:

$$Mg(OH)_2 \rightarrow MgO + H_2O \tag{1.1a}$$
$$MgCO_3 \rightarrow MgO + CO_2 \tag{1.1b}$$

Industry uses a great variety of furnaces to calcinate magnesite and brucite: the most common ones are the *multiple heart furnace*, the *rotatory kiln furnace* and the *shaft kiln*.

The multiple hearth furnace

A multiple hearth furnace consists of a vertical cylindrical steel shell lined with refractory which encloses a series of horizontal circular hearths, usually in number comprised between 10 and 14. A central shaft extends the full height of the furnace and typically supports four cantilever rabble arms equiped with blades or plows, which plow the material on the hearth and convey it to the lower hearth. Heat is provided by direct flame in certain hearths or via the injection of hot gas externally combusted. The feeding material is continuously inserted from above the furnace. The scheme of a multiple hearth furnace is showed in fig.1.3.

This type of furnace is able to to control the temperature very well, its temperature range is 816-1038°C and requires between 6330 and 8440 MJ of energy per ton of MgO produced.

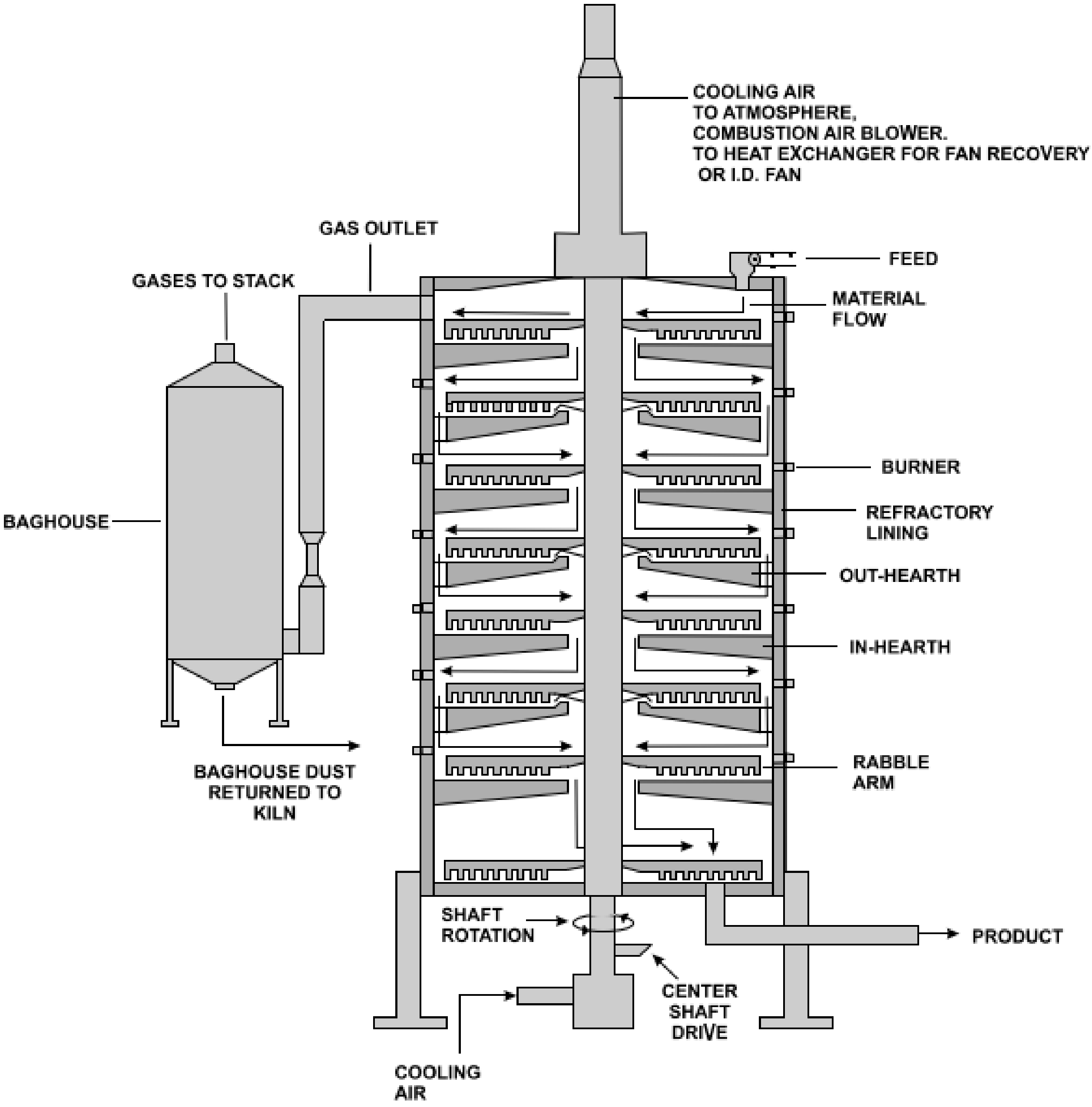

Figure 1.3: Scheme of a multiple-hearth furnace [9]

The horizontal rotatory kiln furnace

The kiln used for the production of magnesia is very similar to the one used for the production of clinker, being a cylinder long between 110 and 140 m, inclined at an angle of 3 to 4°, a typical diameter of 2.4-2.7 and rotating at about 1.5 rpm. Magnesite is fed into the upper back-end countercurrent to the combustion gasses while the flame is generated at the lower front-end.

Depending on the design the firing temperature may reach 1650°C with a residence time of 3 to 6 hours.
The rotatory kiln is very flexible and can produce from low-burned to high-burned magnesia. The burner can be fed by gas, oli or solid fuel as petroleum coke or coal. The energy consumption depends upon the type of product being fired and the required firing temperature.

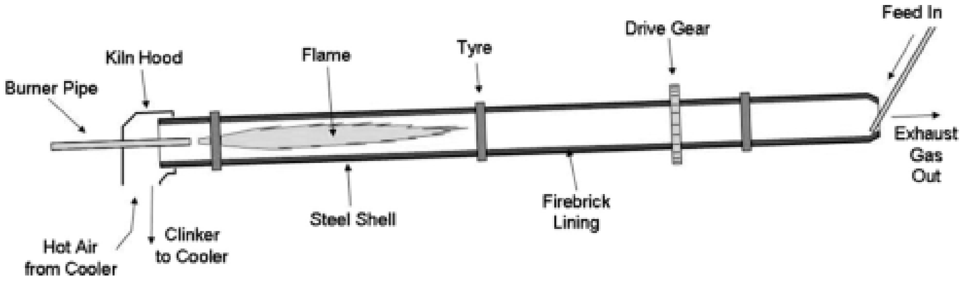

Figure 1.4: Scheme of a rotatory kiln furnace [9]

Shaft kiln furnace

A shaft kiln is essentially a vertical refractory-lined cylinder or ellipse. The ore is charged in at the top of the furnace along with, in some cases, a solid fuel such as coke or anthracite coal.

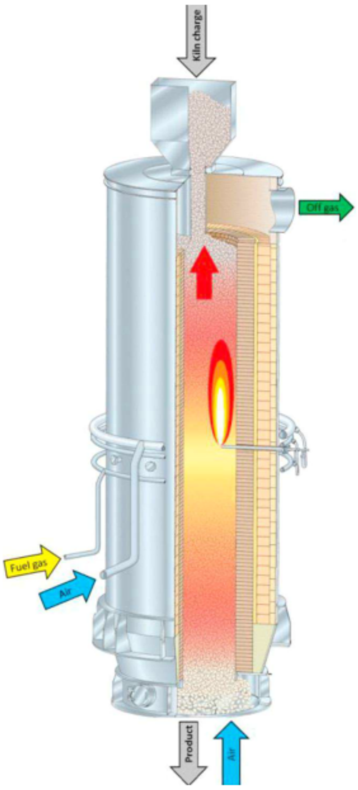

Figure 1.5: Scheme of a shaft kiln furnace [9]

1.2.4 The production of CaO

Quicklime is produced by burning crushed limestone in the rotatory kiln used for magnesia at 1100°C [52]. The decomposition reaction produces CaO and CO_2:

$$CaCO_3 \rightarrow CaO + CO_2 \tag{1.2}$$

After the heating quicklime is crushed and milled.

1.3 Environmental impact of the cement production and mitigation strategies

Concrete is the most used construction material in the world because of its low cost and its great flexibility: it can be used to build structural elements, tunnels, foundations, it can be cast or sprayed on surfaces. The global production of cement reached 3300 MT in 2010 and and grew to 4174 MT in 2016, a 24.6% increment in just 6 years [27]. As explained in section 1.2.1 the production of clinker consumes a lot of resources and the chemical reactions taking place in the rotatory kiln have CO_2 as product, which is the main greenhouse gas responsible of climate change.
We will start analyzing the environmental impact and the energy consumption in the different phases of the production process of cement, then we will analyze the main solutions that are being studied and applied to reduce them.

1.3.1 Energy consumption and CO_2 emissions of the production process of the portland cement

The energy consumption of a cement rotatory kiln varies between 2.9 and 4 $MJ/kg_{clinker}$, based on the combustible used and the efficiency of the kiln. Globally the total energy required varies between 4.5 and 8 MJ/kg_{cement}, taking into account all the production phases, the material extraction and the transports. On the side of the CO_2 emissions the calcination of limestone and clay emit 530 kg of CO_2 per ton of cement while the total emissions vary between 840 and 1150 kg according to the thermal efficiency of the kiln and the used combustible[5]. Mohamad et al. [27] report that the production of cement consumes absorbs almost 12 to 15% of total industrial energy utilization and is responsible of 5 to 8% of the global CO_2 annual emissions. The cement industry is also responsible of the emissions of non-negligible quantities of other polluting substances:

- particulate matter as PM10 and PM2.5, responsible of severe problems to the human respiratory system and chronic obstructive pulmonary disease
- NOx, produced by the combustion of fossil fuels and biomass, which are very powerful greenhouse gases
- SO_2 which is one of the responsible of acid rains
- VOCs, includinc toxic dioxins, furans and PCBs

Huntzinger and Eatmon [20] tried to perform a life-cycle assessment of Portland cement manufacturing in the United States of America, evaluating all the aspects of the cement industry, from resources extraction to final packaging and considering not only the CO_2 emissions but also of other polluting substances. The authors have analyzed 4 products/processes:

1. Traditional Portland cement
2. Blended cement (natural pozzolanas, fly ash)
3. Portland cement when a portion of the process related emissions are captured back using sequestration in waste materials (CKD [*])
4. Portland cement when CKD is recycled back into the kiln

At the end of their analysis the authors have estimated that the 99% of the total environment impact of the production of traditional Portland cement is the cement itself and the impact of the packaging and the after-production logistic is irrelevant compared to the other phases as weel as the initial resources extraction (1.16%). The biggest contributions to the total environmental impact come from the use of combustible, energy and the calcination of limestone and clay: any reduction strategy meant to be effective has to focus on these aspects of cement production.

1.3.2 Main mitigation strategies

The main mitigation strategies adopted act on three aspects of cement production:

- nature of the combustible used
- efficiency of the industrial process
- nature of the final binder

The first aspect can be improved by the use of more efficient fuels or biomass of agricultural origins the combustion of which releases the CO_2 that has been previously consumed by the processes of growth and photosynthesis of the plants. Others organics products as used tires, plastics, animal flours and exhausted oils can be used avoiding their disposal in waste dumps. The efficiency of the industrial process can be improved by using more efficient kilns and optimizing the grinding and milling phases, which consume the most of energy albeit in the electrical form.

The optimization of the industrial process and the use of more ecological fuels can reduce significantly the environmental impact of cement production but it is not able to reduce the emission of CO_2 related to the calcination of limestone and clay because it is an intrinsic effect of the chemical reactions exploited in the production of clinker. CO_2 can be captured in solid products that need to be disposed but this does not reduce its production, simply it transforms a problem in another problem. The only way to reduce the emission related to the calcination is to use complementary and alternative binders to eliminate or drastically reduce the use of

---

[*] Cement Kiln Dust

clinker.

In section 1.1 we have seen that the current standards propose many products that can be used to replace clinker in relevant percentages. Moretti and Caro [28] performed a life cycle assessment on the Italian cement industry considering 11 plants and the main cement classes produced in Italy. Their study has estimated that CEMIII is the cement type having the lowest global warming potential, followed by CEMIV. The reason is that these cements have a lower clinker content that the ordinary Portland cement and CEMII and recycle waste and secondary products of other industrial processes. The study analyses the CEMIII/A and the CEMIV/A and B that are not the ones containing the lowest doses of clinker so we can suppose that CEMIII/B, CEMIII/C and CEMV/C have a lower global warming potential.

1.4 Scope of this work

The analysis of the industrial production process and the environmental impact of the cements present in the current standards has shown that the most effective approach to reduce as much as possible the greenhouse gases emissions is to reduce the use of clinker by substituting it with recycled and waste materials. This leads to a multiple environmental advantage: reduction of the wastes to dispose, reduction of the fuel consumption, reduction of the CO_2 emitted during calcination, reduction of the extraction of materials from the quarries and reduction of the transportation needed to make the cement industry work.

Blast furnace slag, fly ashes, silica fume and the other material behave in different ways from clinker: latent hydraulic properties, pozzolanic reactions, slower hardening time, less porous structure of the cement paste and other characteristics. Currently their use in total absence of clinker is quite rare but the scientific and technological research is active in trying to do so.

The present study is inserted in this research sector and will focus on blast furnace slag activated with magnesia and quicklime. MgO is already use as mineral addition but the use of CaO has activator has not been studied until recently. CaO is a material used since very ancient times and it is cheap and can be found very easily on the market, so it is interest to try using it as alkaline activator for BFS.

Chapter 2

State of art

2.1 The chemical composition and the hydration of GGBFS

The ternary diagram in fig.2.1 shows that the chemical composition of GGBFS is similar to clinker but contains more silica, more alumina and less quicklime. Silica and quicklime are present in percentage generally comprised between 32 and 42%, alumina between 7 and 16% and Fe_2O_3 below 2%. MgO is present in relevant quantities between 7 and 14% while other components as Na_2O, K_2O, TiO_2, Mn_2O_3, P_2O_5 and SO_3[a] are present in quantities below 2% of the mass.

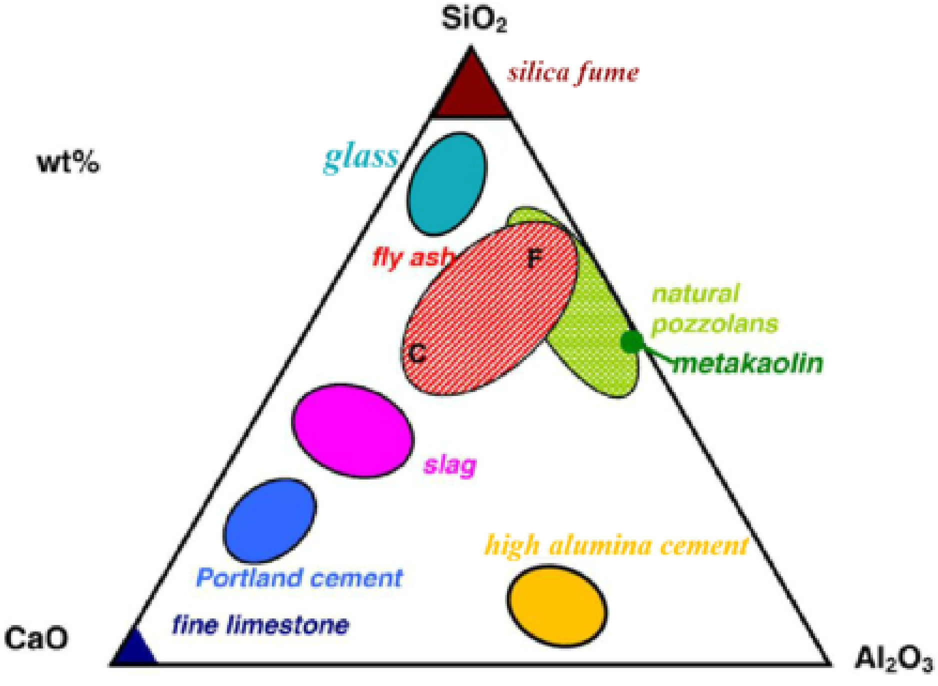

Figure 2.1: CaO-Al_2O_3-SiO_2 ternary diagram (wt% based) of common cementitious materials [25]

As reported by Li [39] and Bertolini and Carsana [6] GGBFS needs an alkaline environment to activate. It is well known that the alkali already present in the clinker or produced by its hydration, as KOH, NaOH, $Ca(OH)_2$and $CaSO_4$ are able to activate the hydration of GGBFS, and for this reason GGBFS in common cement is used together with clinker. Na_2CO_3, Na_2SO_4 and Na_2SiO_3 are able to activate th GGBFS as well.

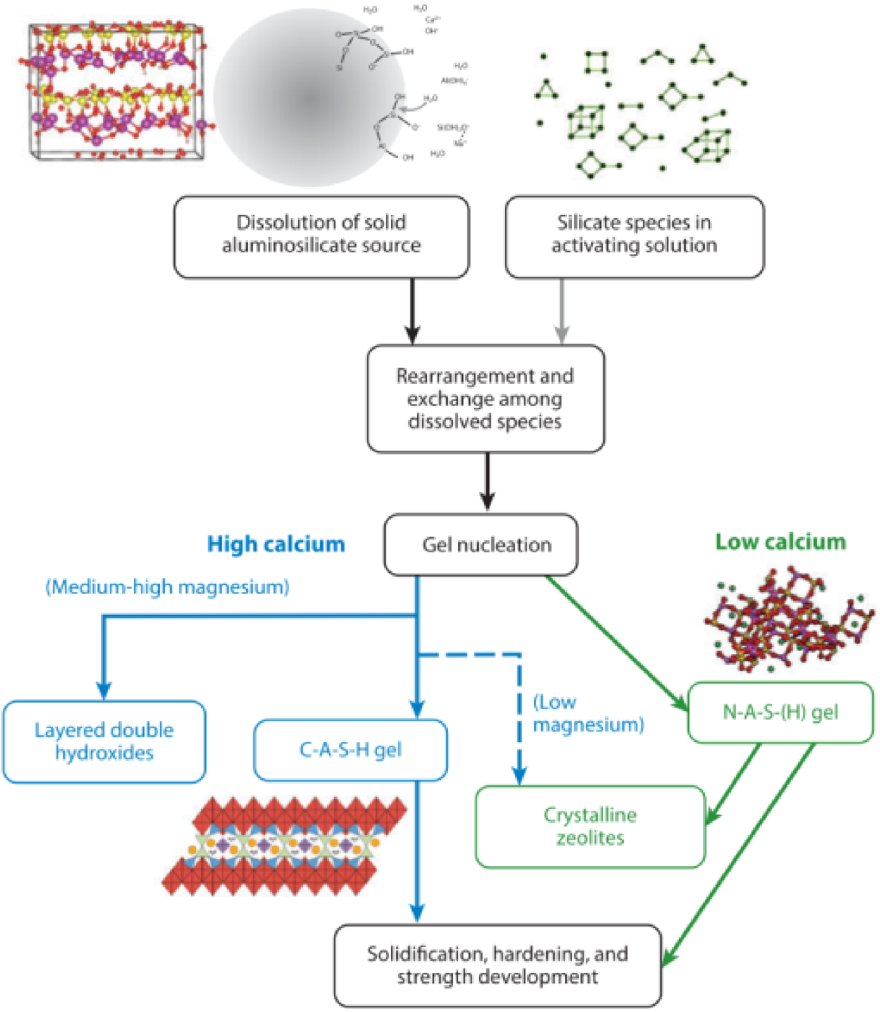

Figure 2.2: Process and reaction products of alkaline activation of a solid aluminosilicate precursor [39]

Fig.2.2 shows schematically the hydration mechanism of slag and fly ashes. The process starts with the dissolution of the solid aluminosilicate phase in a strongly alkaline environment ($pH > 13$). Being a high-calcium precursor, the hydration of slag results in the formation of calcium aluminum silicate hydrates (C(A)SH) type gel and layered double hydroxides as hydrotalcite and hydrotalcite-like phase [39, 34].

2.1.1 The importance of the activator

The choice of the activator is not related only to the needed pH because it has influence on the hydration process and the mechanical performance of the final paste. NaOH accelerates early-age activation but tends to present a barrier to advanced reactions, therefore limiting the later-age strength. In contrast Na_2SiO_3 is a slower activator but improves long-term strength, because NaOH-activated systems present a more porous microstructure. Furthermore using an activator having a molar ratio SiO_2/Na_2O in the range of 1.0-1.5 is found to provide the densest microstructure and the highest strength for both slag and fly-ash-based alkali activated cements.

2.1.2 Effects of the slag composition

The content of MgO

Winnefeld et al. [35] studied the effects of slag composition on the hydration process and observed that a higher presence of MgO in sodium meta-silicate activated slag, up to 13.2%, leads to an increment in both the early-age and long-term strength, due to an increased hydration rate and the production of more C(A)SH gel and more hydrotalcite that reduces the porosity. This remarkable increment has not been found in NaOH-activated slags, so the advantage of a high MgO content can be exploited only choosing suitable activators. The authors also highlight that high MgO contents are known to provoke a loss of strength at later age, so an optimal content of MgO should be searched (2.3).

Al-Tabbaa and Jin [1] report that only Mg in glassy phase controls the formation of hydrotalcite and amorphous phase and that the inherent MgO in the slag composition decreases the Al uptake by C(A)SH. Strong correlation between MgO content and Mg/Al ratio of hydrotalcite has been found.

The authors report also that 3 sodium silicate activated slag having inherent MgO contents of 9.6, 12.1 and 18.6% used for concrete fabrication showed compressive strength of 26.2, 48.2 and 65.2 MPa after 28 days of curing and the 1 year strength improved too as inherent MgO content was increased.

The content of Al_2O_3

The content Al_2O_3 has an influence on the strength development too, albeit less evident than the MgO content. Sodium meta-silicate activated slags showed a slightly decrement in strength after 7 and 28 days of curing but the strength after 180 days is very similar to the other studied slags. The cause has been associated to a lower amount of C(A)SH and hydrotalcite as the presence of more Al_2O_3 lower the concentration of other oxides present in the slag. The influence of the presence of aluminum oxide is far less relevant with NaOH activation.

2.2 Additive MgO as activator for GGBFS

The reactivity of MgO is associated with its specific surface area (SSA) as explained at section 4.3.4 because it reflects the burning temperature in the manufacture process. Reactive MgO rapidly dissolves in water and creates an alkaline solution with a pH of 10-12 that is able to activate the hydration of GGBFS. MgO as sole activator of GGBFS has been hardly studied so far.

Several authors [22, 23, 29] investigated the hydration products and microstructure of MgO-GGBFS blends. The main hydration products are C-A-S-H gel and hydrotalcite. magnesium

Figure 2.3: Correlation between compressive strength and calcium, magnesium and silicon oxides content in slags activated with sodium meta-silicate and sodium hydroxide [35]

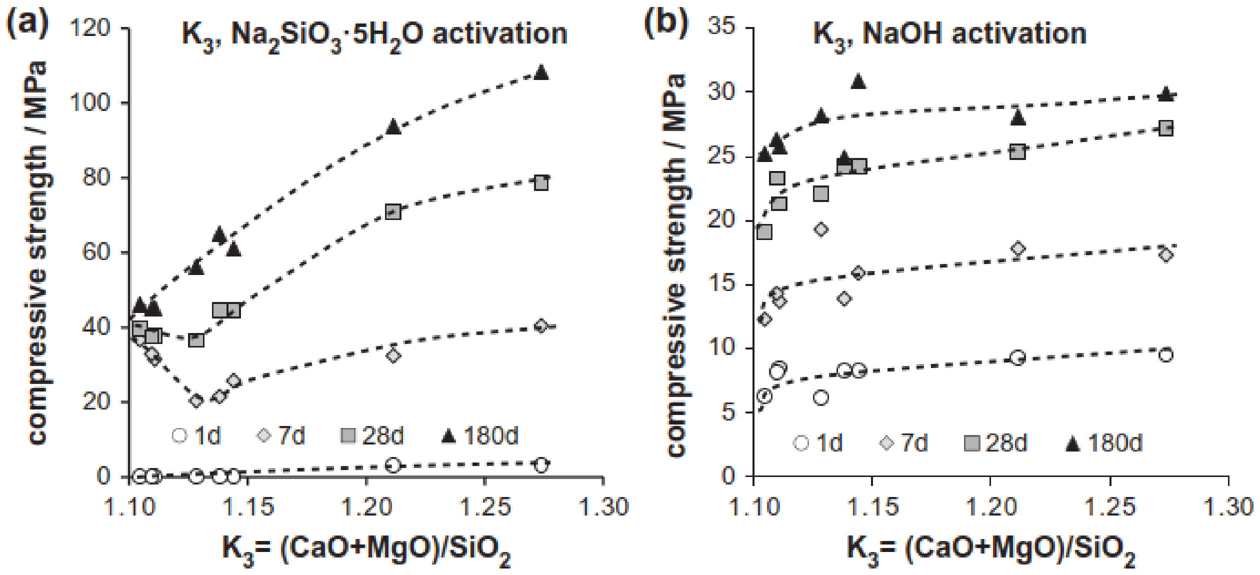

silicate hydrates (MSH) can be present but it is hardly distinguishable because of its low crystallinity and high miscibility with C-(A)-S-H and C-S-H. Additive MgO used as activator behaves quite similarly to inherent MgO in the formation of hydrotalcite: both the quantity and the Mg/Al ratio increase with the MgO dosage. pH was found to be the major controlling factor in the activation process, which is dependent on the reactivity and content of MgO in the blend as well as the content of CaO impurity in the MgO composition.
The reaction mechanism of the MgO-GGBFS blends was proposed as follows:

1. Reactive MgO dissolves in water producing Mg^{2+} and OH^- ions, followed by the breakdown of the glass structure of GGBFS due to alkaline conditions

2. The release of Ca, Si and Al ions forms C-A-S-H gel and meanwhile Mg with Al to form hydrotalcite and maybe with Si to form M-S-H

3. If the consumption rate of Mg^{2+} exceeds the dissolution of MgO brucite will not form, otherwise $Mg(OH)_2$ nucleation and growth occur

4. The presence of sulfates in the MgO or in the GGBFS may produce ettringite

Jin, Abdollahzadeh, and Al-Tabbaa [22] studied the hydration of a 8.5% MgO containing GGBFS activated with MgO products of different reactivity, origins and impurities. Together with the results just reported they noticed that an excessive quantities of hydrotalcite in the hydrated paste causes an over-expansion and volume instability that may be detrimental to the strength. Sulfates contained as impurities in MgO and inherent in GGBFS may form ettringite, whose presence has been reported by Park et al. [29] too. Fig.2.4 shows the XRD pattern obtained by Park et al. where the peaks associated to the different mineral phases are marked using the letters according to tab.2.1

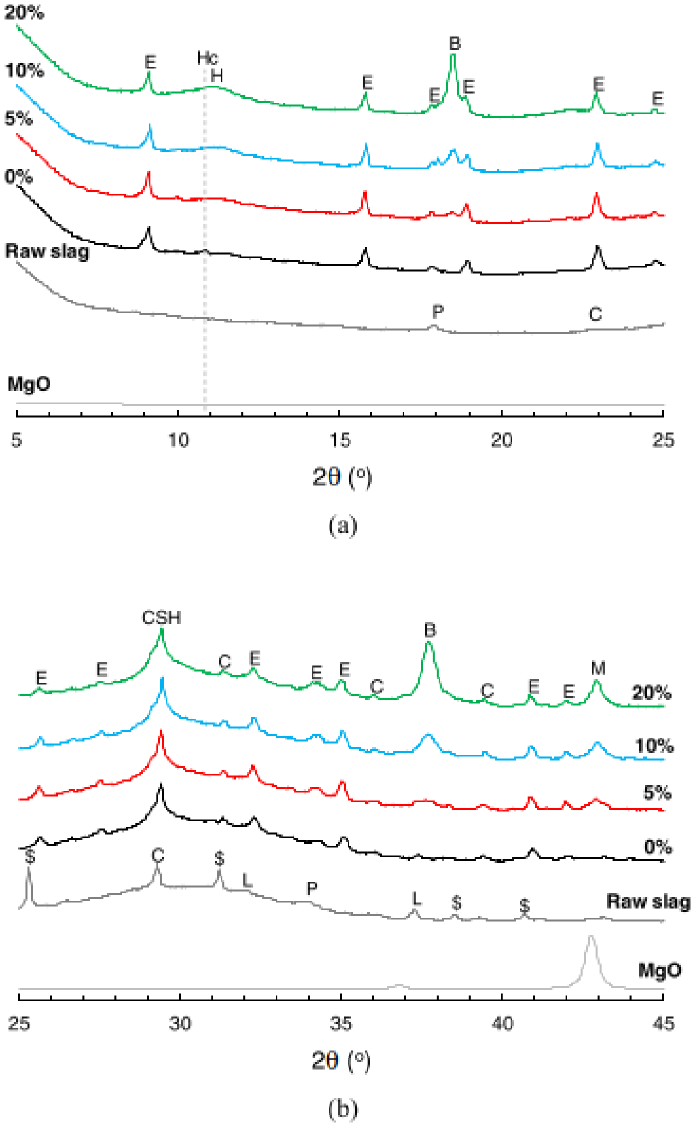

Figure 2.4: XRD of MgO activated GGBFS pastes with varying MgO doses [29]

The expansion caused by ettringite may provoke cracks at later ages and compromise the strength. In fact cracks have been found on scanning electron microscopy (SEM) images in both the most reactive and the second least reactive analyzed MgO but the crack propagation was more significant in the latter case: the author concluded that lower reactivity is more detrimental to the cement soundness in the long term due to the latent hydration of less reactive MgO. Because of the volume instability due to these expansive phenomena it is not granted that more reactive MgO provide higher compressive strengths, as shown in fig.2.5.

Mineral phase	Mark
M	MgO
P	$Ca(OH)_2$
$	Anhydrite
L	Lime
C	Calcite
B	Brucite
CSH	CSH-type gel
E	Ettringite
H	Hydrotalcite
Hc	Hemicarbonate
S	Monosulfate

Table 2.1: Mineral phase mark in XRD pattern [29]

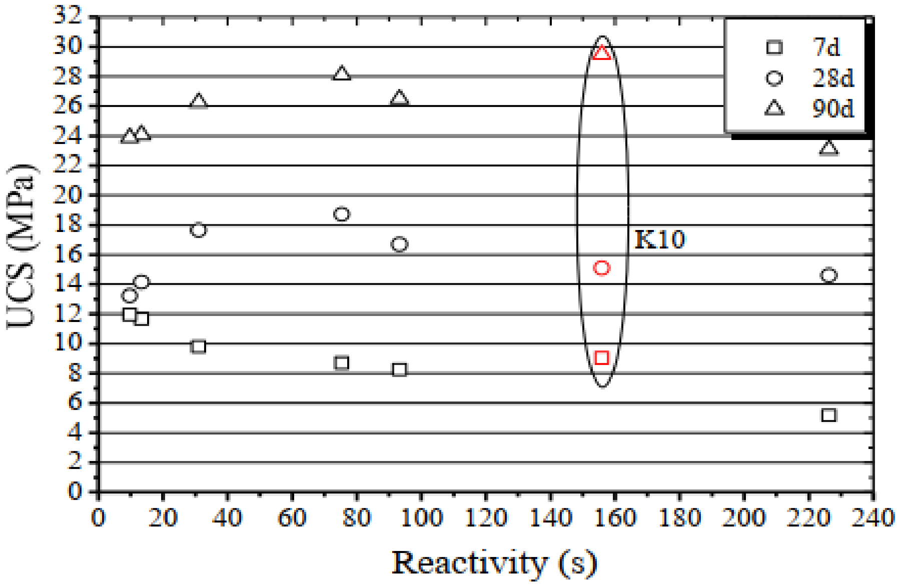

Figure 2.5: Unconfined compressive strength in MgO-GGBFS pastes as function of curing age and MgO reactivity [22]

Due to the high specific surface area of reactive MgO, the standard consistency of MgO-GGBFS pastes increases almost linearly with the MgO content when medium reactivity MgO was used. The setting time was significantly delayed when the MgO content increased to $\geq$ 30%. The optimal content of MgO in terms of compressive strength is between 15-30%.

2.3 Additive CaO as activator for GGBFS

The interest on the use of CaO and $Ca(OH)_2$ as activators grew quite recently because of the low price and great availability of this products on the market and their handling and stocking safety as compared to other alkali as NaOH and Na_2SO_3.

As already highlighted in section 1.1 the use of quicklime is very ancient and it is know to activate the pozzolanic reactions of many materials as fly ashes, silica fumes and natural pozzolanas. Its high reactivity with water allows to increase the pH of the solution quite rapidly and the use of this product as activator is possible.
The main hydration products of lime activated GGBFS are C-(A)-S-H, hydrotalcite, portlandite, akermanite, monocarboaluminate. Some carbonation is expected to be present [24, 17] as shown by the XRD patterns in fig.2.6 for different CaO-GGBFS compositions.

Figure 2.6: XRD patterns of CaO-GGBFS pastes having different w/b ratios, BFS specific surface area and curing conditions [17]

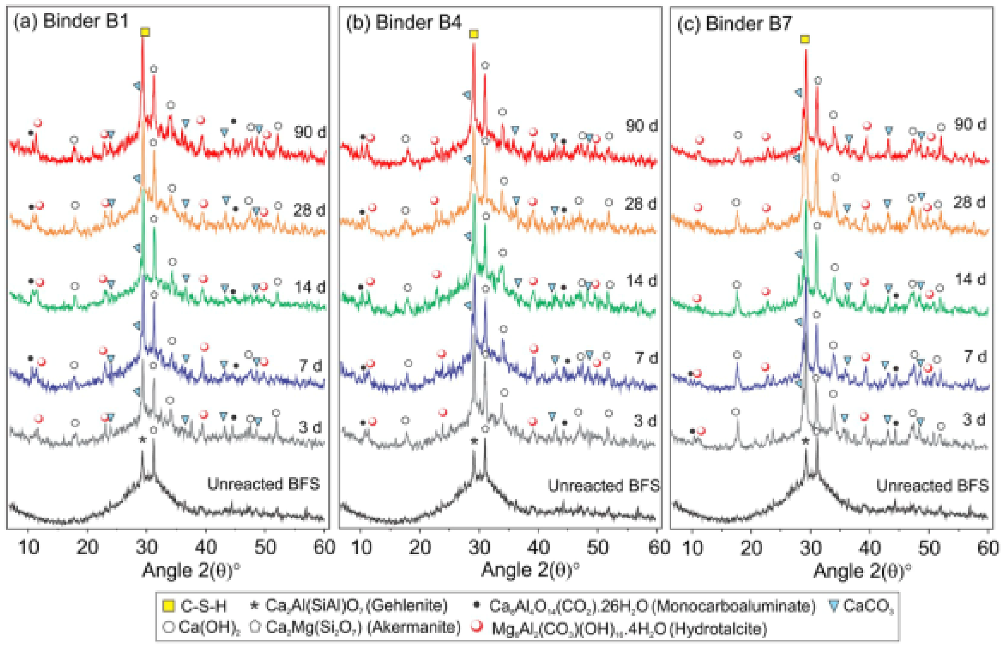

Kim et al. [24] suggested that CaO is a more suitable activator than $Ca(OH)_2$. They studied two composition of AAS pastes using an activator/binder ratio of 6.25% and a water/binder ratio equal to 0.4. One composition has been activated by CaO and the other by $Ca(OH)_2$. CaO activated slag reached a compressive strength of 42 MPa after 28 days, almost the double of the other composition which arrived at 23 MPa. At 56 days the first composition reached 53 MPa while the latter 24 MPa. CaO seems to be able to activate more BFS and to be less sensitive to carbonation; furthermore the initial dissolution heat of CaO is clearly much higher than $Ca(OH)_2$but the cumulative hydration heat over 72h is lower. It is worth noting that CaO consumes a certain quantity of water to form $Ca(OH)_2$ that dissolves in a more concentrated solution than using $Ca(OH)_2$ directly so we can expect similar results if we reduce the w/b of the $Ca(OH)_2$ in order that the two ratios after hydration of CaO were the same.
Jeong et al. [21] studied four CaO-GGBFS paste compositions using 4 slags that had very similar compositions in terms of the main components (CaO, SiO_2, Al_2O_3 and MgO), but different content of anhydrite ($CaSO_4$), gypsum, calcite, glass phase and different SSA (between 500 and 580 m^2/kg). The w/b was 0.4 for all the compositions. The compressive strength after 28 days of curing varied between 23 and 52 MPa and seems correlated with the increasing content of gypsum but not with the one of anhydrite and the SSA of the slag. The average pore size seems

to be more relevant to strength rather than the total pore volume because of the presence of a large fraction of unreacted slag. One composition showed many clusters of calcite that may be the cause of the low strength. The strength of the strongest composition is quite comparable to the results obtained by Kim et al. at double the age.
Burciaga-Díaz [17] tested 9 compositions of pastes changing the activator/binder (a/b) ratio, which is the ratio between the mass of activator and the total mass of binder (activator+GGBFS), from 6% to 10%, the w/b from 0.30 to 0.36, the curing temperature and tested two BFS having SSA of 360 and 450 m^2/kg. The unconfined compressive strength of the paste samples is shown in fig.2.7 After the compressive strength tests he applied the Taguchi method to optimize the composition and found that:

- 10% is the optimal a/b ratio to maximize strength
- 0.30 is the optimal w/b ratio
- 20°C i the optimal curing temperature
- using BFS having higher SSA improves the strength

The effect of the a/b ratio may explain while Kim et al. [24] and Jeong et al. obtained different results in terms of strength even using very similar slags. SSA, gypsum and glass phase content may have very important roles but these parameters are not presented in Kim's paper.

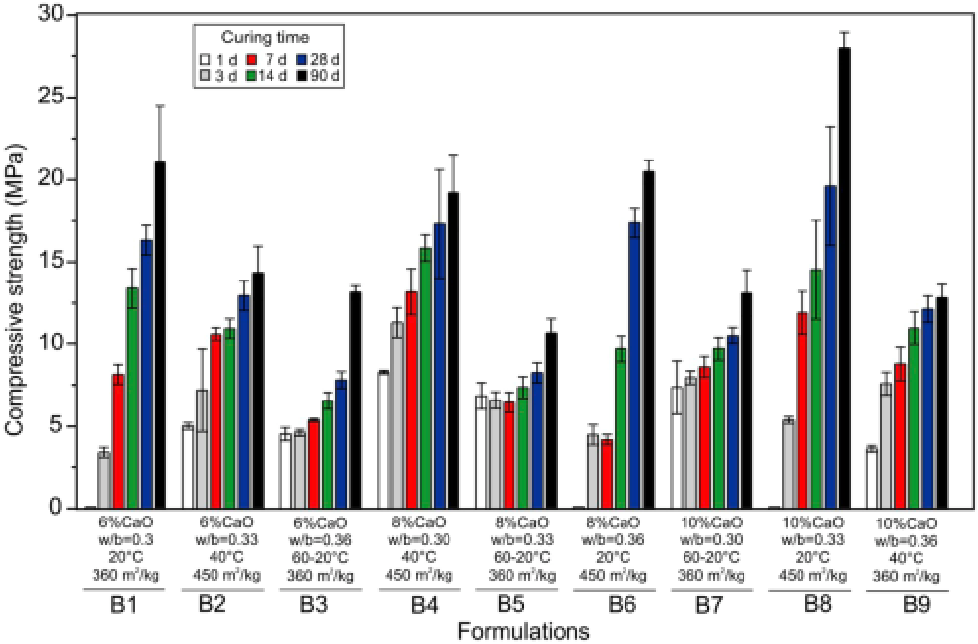

Figure 2.7: Compressive strength of CaO-GGBFS having different a/b, w/v ratios, curing temperature and BFS SSA [17]

Seo et al.[31] tried to incorporate CaO up to 5% in ternary Portland cement-slag-silica fume blends and observed that the effects are detrimental form the strength, in particular with a CaO dosage of 5% because of the formation of cracks. Steam cure worsens the problem even more.

2.4 The mix between CaO and MgO

The presence of CaO impurities in the activating MgO is known to improve the strength at early age thanks to an increment of the pH [1]. Gu et al. [19] compared 6 compositions of alkali activated slags having a/b ratio 10% and w/b 0.35 and 0.38. The activators were a mix of CaO and MgO each one varying between 0 and 10% of the total binder mass. Pure CaO activator reached the highest early-age strength while pure MgO the lowest, although the strength after 90 days were the same. A 1% CaO addition to MgO was able to improve the early-age strength but increasing the CaO/MgO ratio rapidly reduces the strength both at early and at long ages, reaching the minimum at 2/8. High CaO content provides higher pH that reaches the peak after 28 days of curing and remains almost constant until 90 days. MgO on the contrary starts with a lower ph that progressively rises. 0.5% and 1.5% CaO doses show a peak of pH after 28 days followed by a decrement. The results obtained by Gu et al. for w/b 0.38 are shown in fig.2.8.

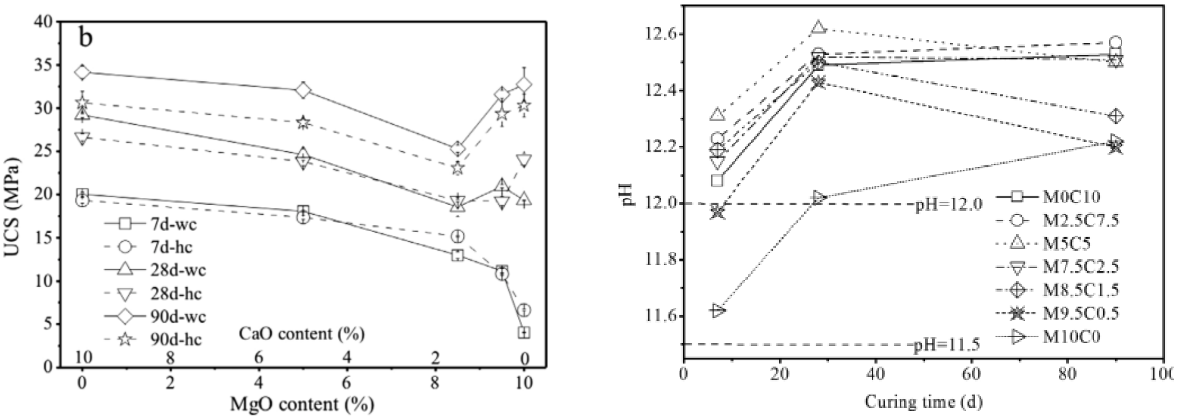

(a) Development of unconfined compressive strength

(b) Development of pH

Figure 2.8: Development of pH in CaO and MgO activated slag pastes [19]

Chapter 3

Experimental procedures

In this chapter we will describe the experimental tests that have been performed to study both the precursors and the hardened compositions. The analysis techniques will be presented starting from the ones used to characterize the microstructure, then the study of the reaction kinetics will be presented and finally the mechanical essays.

3.1 Density measure via pycnometer and isopropanol

The information provided by the manufacturers of chemical products should be verified to check the presence of impurities, especially if one is working with highly reactive alkali as quicklime and magnesia. The measure of the density is a very quick test that does not require any particular preparation and it has been performed on quicklime and magnesia. The pycnometer is a little recipient made by glass that is filled with a liquid, in our case isopropanol has been used because distilled water would have reacted with the alkali, a plug with a capillar closes the pycnometer letting some liquid to rise. The full pycnometer is weighed obtaining the measure m_1. A weighed quantity (m_2) of the powder sample is inserted into the pycnometer and other isopropanol is added to fill it again. The plug is put again and the pycnometer is weighed, obtaining m_3. The density is calculated as:

$$\rho = \frac{m_2}{m_1 + m_2 - m_3} \cdot \rho_{iso} \tag{3.1}$$

where ρ_{iso} is the density of the isopropanol (0.785 $\mathrm{g/cm^3}$).

3.2 Description of the mixing procedure

The mixing has been done using instruments complying to the norm. The characteristics of the mixer are defined in the norm and they are shown in fig. 3.1. The speed is indicated in tab. 3.1.

The mix of mortar has been done following the procedure:

1. dry mixing of sand, GGBFS and activators for 2 min. at low speed
2. introduction of 1/3 of the water, then mix for 20 s at low speed (repeat 2 times)
3. introduction of the remaining 1/3 water, mix for 2 min. at low speed

	Rotation [min^{-1}]	Planetary movement [min^{-1}]
Low speed	140 ± 5	62 ± 5
High speed	285 ± 10	125 ± 10

Table 3.1: Classification of mixing speed according to *NF EN 196-1* [56]

4. remove the mortar from the bowl, then mix at high speed for 1 min

The mortar is introduced in the molds by layers and vibrated 5 s to compact each layer. X-ray powder diffraction (XRD) requires paste samples while some other analysis, as ultrasonic hardening and semiadiabatic calorimetry, use fresh mortar sample that harden in the testing machine. The mixing procedure is thus adapted according to the specific test.
The samples for the tests involving hardened pastes and mortars are cured in wet room at 20°C and RH 100% for 3, 7, 28 and 90 days, with the exception of autogenous shrinkage which requires the sample to be sealed in aluminum paper. The details on the sample used and the curing conditions will be explained for each test.

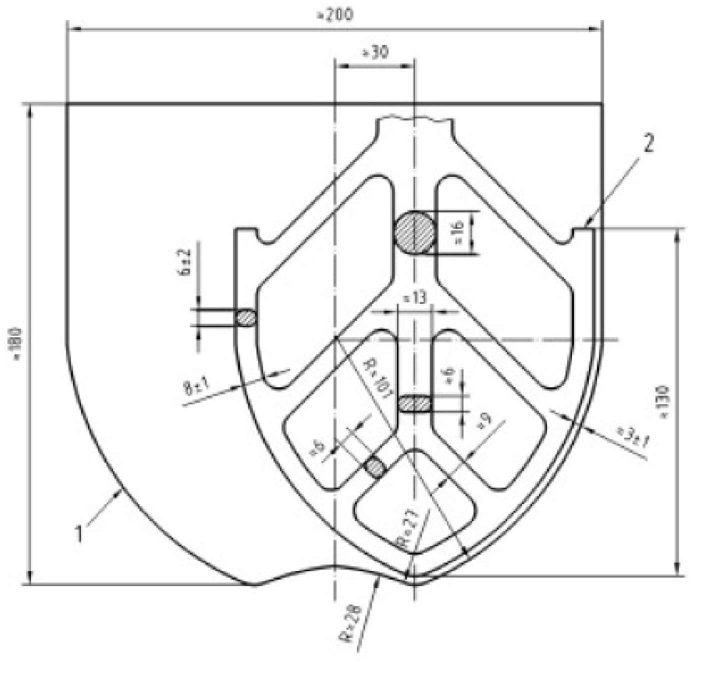

Figure 3.1: Scheme of the mixer in norm *NF EN 196-1* [56]

3.3 Fresh state behavior: Abram's cone and measure of the temperature

The consistency of concrete is a critical parameter because it strongly affects the placement of the material at fresh state: the more fluid the concrete is the easier it is able to incorporate the reinforcement and to compact itself, but at the same time segregation may become more likely.

A very fast and easy test to assess the consistency of ordinary concrete is the *slump test* performed using the Abram's cone. This test is taken as reference to classify the consistence of concrete based on its slump.
The specifications of Abrams cone are described in the standard *NF EN 12350-1* [53]:

- inferior base diameter: $(200 \pm 2)\,mm$
- superior base diameter: $(100 \pm 2)\,mm$
- height: $(300 \pm 2)\,mm$

And, according to the standard *NF EN 206/CN* [58], 5 consistency classes are defined based on the slump:

Class	Slump [mm]
S1	10 to 40
S2	50 to 90
S3	100 to 150
S4	160 to 210
S5	higher than 200

Table 3.2: Consistency classes according to EN 206

The initial temperature is measured using a Controlab Checktemp 1 termometer having an accuracy of 0.5°C and complying to the norm EN13485.

3.4 Characterization of the microstructure

The study of the microstructure is focused on the analysis of the chemical composition and the pore structure.
It is important to characterize the chemical composition of the precursors to verify the presence of impurities and thus the correspondence between the characteristics of the used product and the specifications provided by the manufacturer. Furthermore the reactivity of quicklime and MgO is related to their pore structure and in particular to their specific surface area [18][10].
The importance of characterizing the hydration products and the pore structure of the cement pastes resides in the necessity of justifying properties like delayed deformations, mechanical strengths and stiffness, ph, porosity etc. For example brucite, products of the reaction between MgO and water, is known to fill the pores and to be an expansive product [1] and its presence may be able to justify both an expansive behavior of the cement paste both a decrease of the porosity in time. Its presence can be justified through essays like X-ray diffraction to identify the crystalline phase, gas adsorption repeated at different ages to follow the changes in the porosity and thermogravimetric analysis to study its formation on a quantitative point of view.

3.4.1 X-ray powder diffraction

Theoretical basis of X-ray powder diffraction

This analysis technique has been developed since the end of the 19th century and is based on the elastic reflection of an X-ray impacting a crystalline lattice of atoms [7]. As figure 3.2 shows, a beam of X-rays impacting a crystalline lattice is partially reflected and partially diffracted, because some X-rays impact the external atoms of the lattice and some others penetrate across the space between these atoms and impact the more internal layers.

Figure 3.2: Constructive and destructive interaction according to Bragg's law [42]

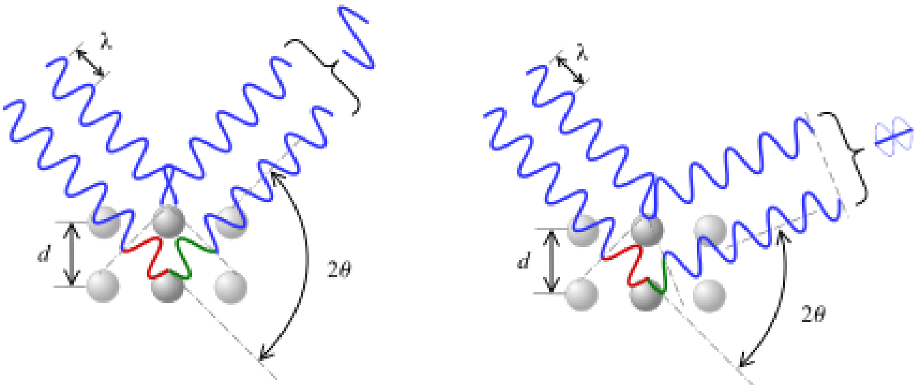

The phase shift between the reflected and the diffracted rays forms a constructive interference if and only if the conditions of the Bragg's law is fulfilled (equation 3.2) [16]

$$n\lambda = 2d\sin\theta \tag{3.2}$$

where:

- n is a positive integer, representing the order of diffraction
- *lambda* is the wavelength of the radiation
- d is the distance between the atomic layers
- θ is the angle of attack of the x-ray

In a diffractometer the powder sample is loaded in a small disc-like container and its surface is carefully flattened. The disk is tilted by the angle θ while a detector rotates around in on an arm at twice this angle as shown in figure 3.3

For the purpose of the present study the powder diffraction is used only to identify the the crystalline solids, so the obtained diffraction pattern is compared to the ones of already known solids. Generally speaking the solids having crystalline structures present patterns characterized by very sharp peaks, while amorphous solids are more similar to continuous and smooth curves. Some techniques are available to take more information and to estimate the single intensity of overlapping peaks and to determine the crystalline structure of the solid [11][8].

Many X-rays source are available for powder diffraction and, based of the nature of the solid to analyze, the most suitable one should be chosen to avoid fluorescence. The most used X-ray source is the copper (Cu) tube which is problematic with transition metals like cobalt (Co), iron (Fe) and manganese (Mn) [12]. Fortunately these elements are not expected to be present in alkali activated cement pastes.

Figure 3.3: Hemisphere of diffraction [50]

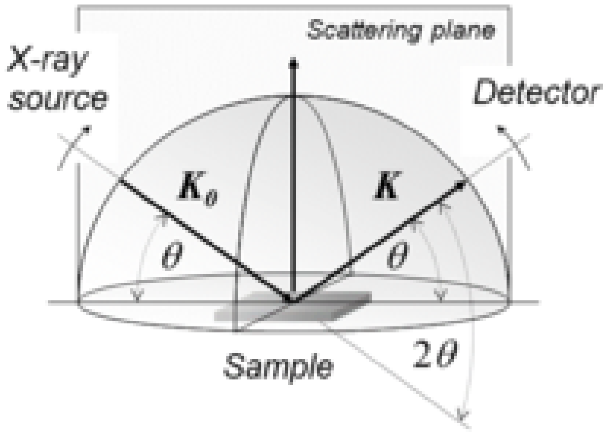

Experimental procedure

The analysis has been done on paste samples, composed by the binder, the activator and the water without the use of any inert material; the w/b is 0.55 for all the compositions. The samples have been cured in wet room (20°C and 100% RH) for 90 days, then the internal part has been grounded into powder until it passed through a $80\mu m$ sieve.
The used diffractometer is a Bruker D2 phaser set on the following parameters:

- voltage: 30 kV
- rotation frequency: 10 t/min
- anti-cathodic tube type: copper (Cu)
- angle range: 2θ between 5° and 80°
- step: 0,02°
- duration: 2 seconds
- opening: 0,6 mm
- separator: 1 mm

The resulting patterns have been compared with the ones of the anhydrous binders (BFS + activator) and the diffraction patterns indicated by Martin [40], Hunnicut [38], and Bernard [37].

3.4.2 Measure of the LOI via DTGA

Theoretical bases of DTGA

The powder diffraction analysis that has been performed does not provide any information on the quantities of reaction products but allows only to identify them. To have an estimation of the quantity and to follow its evolution in time some other analysis approaches should be used and one of the most commons is the differential thermogravimetric analysis.

This analysis technique uses heat to change the equilibrium of chemical reactions to provoke the decomposition of the hydrated and carbonated products present in the cement paste. The sample is grounded in powder until it passes through 80 μm diameter sieve. Some tens of milligrams are taken for the analysis and, once put inside a crucible, the sample is placed on the balance inside the furnace of the testing machine. The atmosphere inside the furnace is controlled by the injection of gas like nitrogen. The temperature is increased according to the setting decided by the user until a threshold, usually 1000°C, and then decreased to room temperature. During this process both the mass and heat power are measured at constant time steps. After the post-processing phase on the chosen temperature interval to retain, derivation and superposition of the curve of mass and its first derivative we obtain a graph similar to the one in figure 3.4.

The mass-derivative curve is characterized by peaks contained in well defined temperature ranges. The beginning and the end of each peak identify the beginning and the end of a certain decomposition reaction and the position in terms of temperature identify the nature of the decomposing product. Some attention should be paid because the range of temperature in which a reaction happens and the position of the peaks are not fixed but depend on the quantity of decomposing product, the temperature increase rate and the gas used to control the atmosphere. A known example of this translation of peak temperature is brucite whose peak can move between 350 and 450°C [32] as shown in figure 3.5.

As it happens for XRD the DTGA has a problem of overlapping of peaks in presence of multiphase solids because many chemical reactions take place in the same ranges of temperature: for example the evaporation of bounded water in C(A)SH and the decomposition of hydrotalcite take place between 105 and 300°C [24] and their effect are difficult to separate.

Description of the experimental protocol and result exploitation

In the present study this analysis has been done on mortar samples, sometimes fabricated *ad hoc* sometimes taken after the compressive strength test. The materials analyzed are both the precursors both hardened mortar at 3 curing ages: 7, 28 and 90 days.

The sample is broken into pieces and reduced in powder until it passes through a 80μm diameter sieve and inserted in an alumina crucible.

The testing machine is a Mettler Toledo TGA/DSC 1 and the used analysis protocol is the following one:

- heat from room temperature to 105°C at 10°C/m
- temperature constant at 105°C for 30 min
- heat up to 1000°C at 10°C/min
- 1000°C constant for 15 min
- cooling to room temperature at -20°C/min

The temperature plateau at 105°C has the function of leaving the unbounded water to evaporate, and the other plateau at 1000°C is meant to leave time to let the powder to stabilize before starting the decreasing temperature phase. Only the mass between the end of the 105°C and of the 1000°C is considered.

The reference temperature ranges chosen to exploit the results are:

- 105-300°C to catch the evaporation of water bounded in the C(A)SH layers and the decomposition of hydrotalcite
- 105-600°C to catch the decomposition of all hydrates
- 600-1000°C to catch calcination and crystallization of unreacted BFS
- 105-1000°C to measure the total mass loss

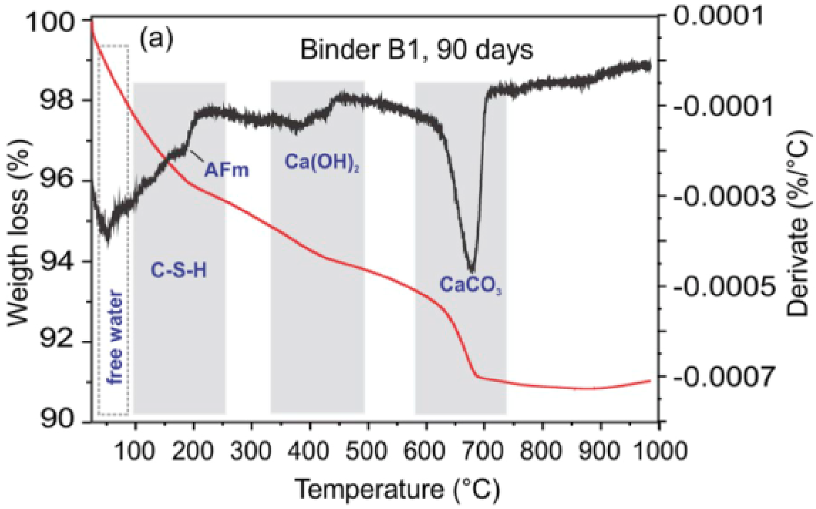

Figure 3.4: Example of TGA analysis and post-processing of the results [17]

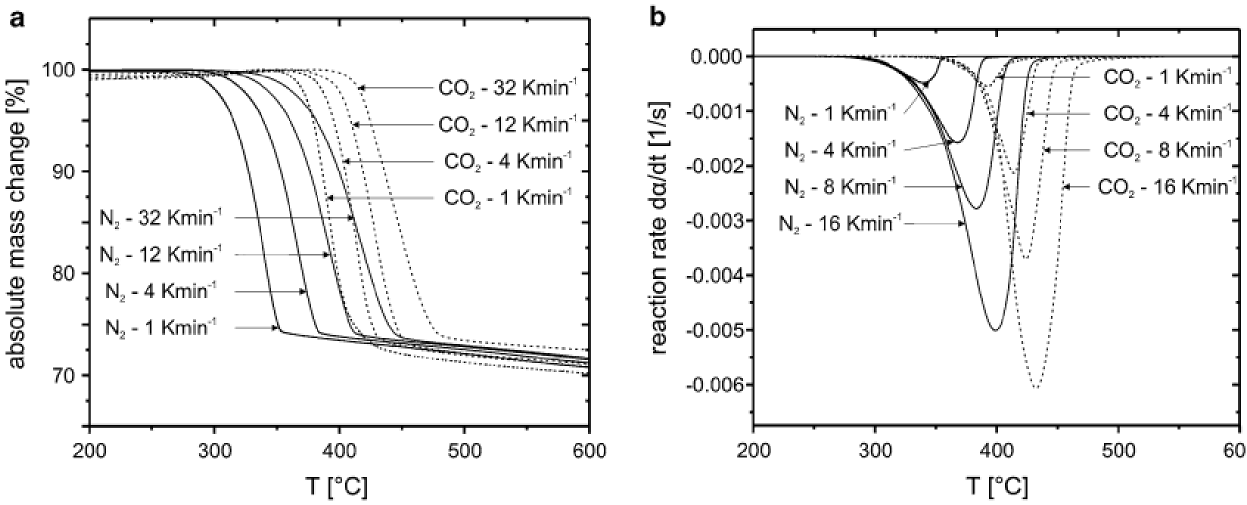

Figure 3.5: TGA curves of brucite depending on the temperature increase speed, the gas and the gas injection flux [32]

The main limit of the adopted preparation technique is that interlayer water of C(A)SH starts evaporating at around 50°C [24] and the loss of mass associated with this phenomenon is superimposed with the evaporation of free water. Furthermore quantifying the C(A)SH lost below 105°C detaching it from free water is not possible, so we should not expect the loss of mass between 105-300°C to grow with the curing age.

3.4.3 Study of the pore structure

The pore size and distribution have a very strong influence on important properties of cement-based materials as compressive strength and elasticity, permeability and diffusivity, delayed deformation, durability to freezing and thawing, and are related to the reactivity of the chemical products used as binder and activators [10][18] because the specific surface area is a measure of the quantity of product that is able to react with water.
Pores can be present in the cement matrix, in the aggregates, at the interface between cement paste and aggregates or voids due to bleeding of the water. Many categorization of the pores according to their size have been proposed but nowadays a unique one has not been reached because pores having the same role and origin may be associated to overlapping ranges of size. A "general" classification is the proposed by IUPAC that keeps into account the size only, but some others are specific for the study of cement-based materials. The IUPAC classification and some important classifications specific for concrete science are proposed in fig.3.6.
The pore structure is described using many parameters:

Porosity defined as the ration between the total pore volume and the bulk volume; usually we talk about "effective" porosity which considers only the accessible pores

Hydraulic radius ratio between the pore volume and the pore surface

Specific Surface Area (SSA) usually defined as the ratio between the total surface area of the pores and the mass of the bulk material

Pore Size Distribution defined as $D_V(r) = -\frac{dV}{dr}$. It can be represented as integral pore size distribution or differential pore size distribution

Many methods are available to study the porosity of cement-based materials, and they are suitable to study different pore size ranges: the application fields of the most commonly used ones are shown in fig.3.7.
It is worth noting that few methods are able to characterize pores below the range in which simultaneous presence of gel and capillary pores occurs that thus is hard to study. Mercury intrusion porosimetry is able to characterize pores from the largest sizes to the smallest micropores, while gas adsorption has a closed range of pore size it is suitable for. Water adsorption, which is another very used method because of its simplicity and safety, provides only the volume of the accessible pores but no information about their distribution.
In order to characterize well the porosity it is better to use different methods and combine the information that each one provides. In the present study we have performed the nitrogen adsorption and the water adsorption tests.

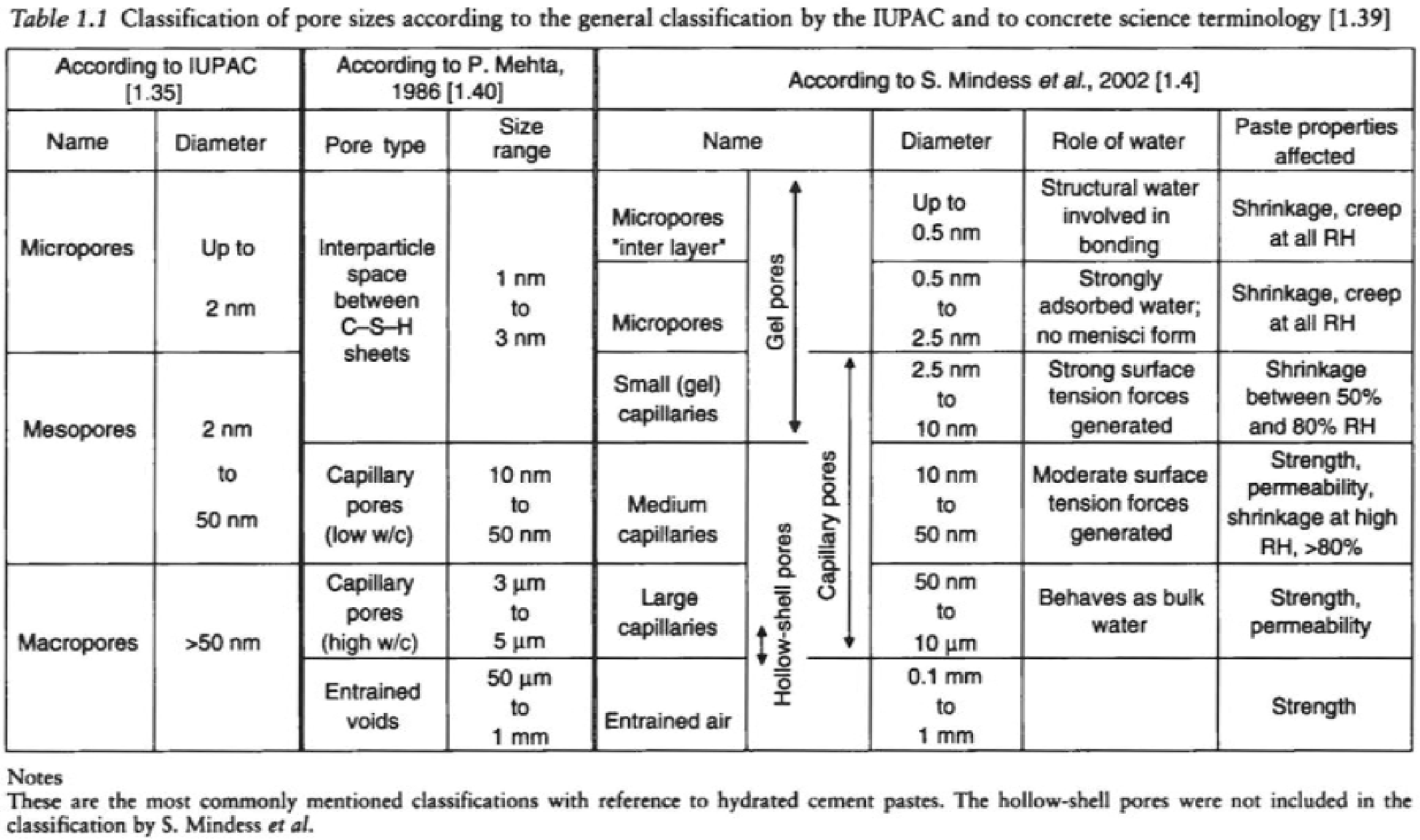

Table 1.1 Classification of pore sizes according to the general classification by the IUPAC and to concrete science terminology [1.39]

According to IUPAC [1.35]		According to P. Mehta, 1986 [1.40]		According to S. Mindess *et al.*, 2002 [1.4]				
Name	Diameter	Pore type	Size range	Name		Diameter	Role of water	Paste properties affected
Micropores	Up to 2 nm	Interparticle space between C–S–H sheets	1 nm to 3 nm	Micropores "inter layer"	Gel pores	Up to 0.5 nm	Structural water involved in bonding	Shrinkage, creep at all RH
				Micropores		0.5 nm to 2.5 nm	Strongly adsorbed water; no menisci form	Shrinkage, creep at all RH
Mesopores	2 nm to 50 nm			Small (gel) capillaries	Capillary pores	2.5 nm to 10 nm	Strong surface tension forces generated	Shrinkage between 50% and 80% RH
		Capillary pores (low w/c)	10 nm to 50 nm	Medium capillaries	Hollow-shell pores	10 nm to 50 nm	Moderate surface tension forces generated	Strength, permeability, shrinkage at high RH, >80%
Macropores	>50 nm	Capillary pores (high w/c)	3 µm to 5 µm	Large capillaries		50 nm to 10 µm	Behaves as bulk water	Strength, permeability
		Entrained voids	50 µm to 1 mm	Entrained air		0.1 mm to 1 mm		Strength

Notes

These are the most commonly mentioned classifications with reference to hydrated cement pastes. The hollow-shell pores were not included in the classification by S. Mindess *et al.*

Figure 3.6: Classification of pore sizes according to IUPAC and concrete science [3]

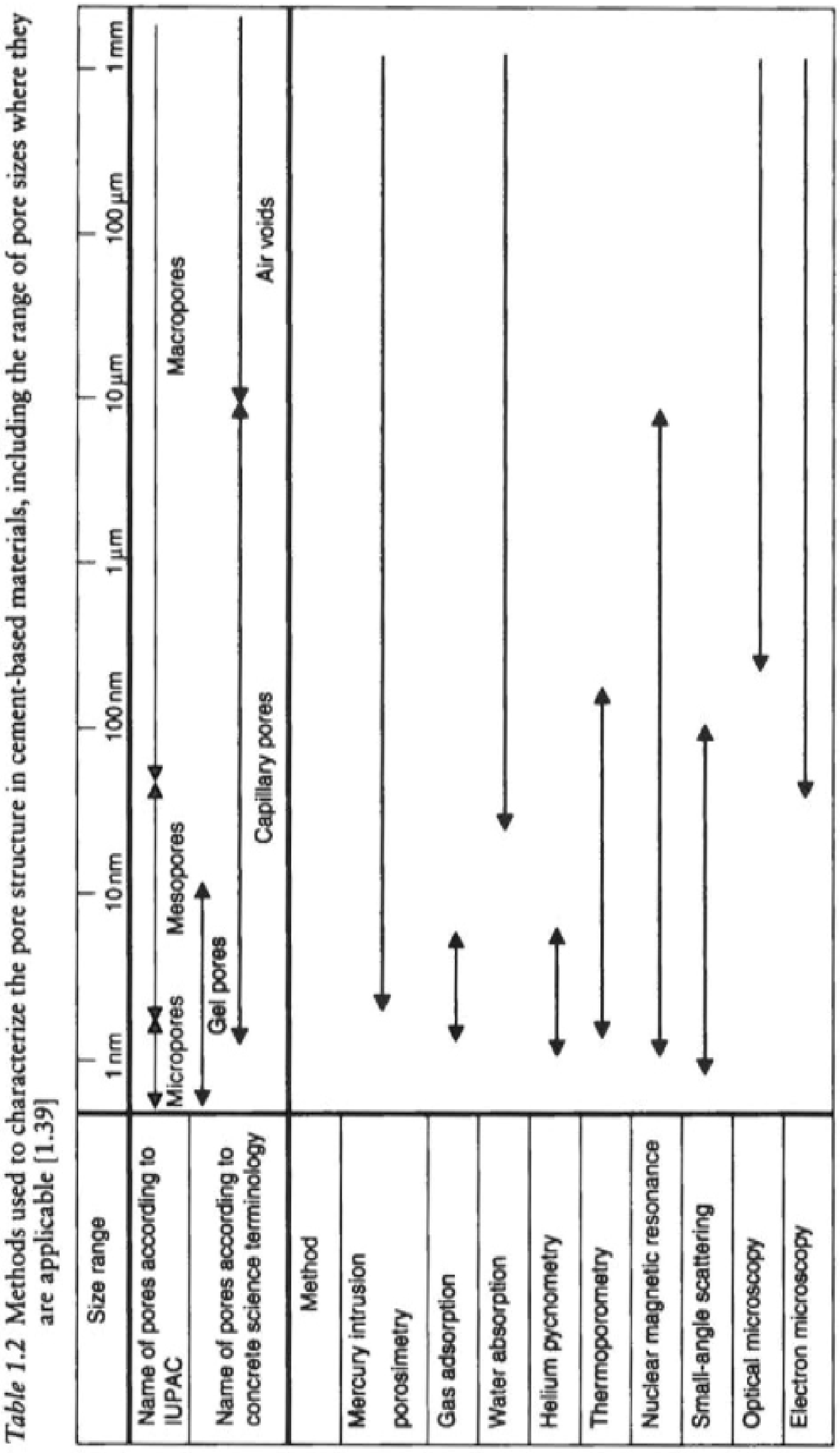

Table 1.2 Methods used to characterize the pore structure in cement-based materials, including the range of pore sizes where they are applicable [1.39]

Figure 3.7: Methods to study the porosity and fields of application [3]

Nitrogen adsorption

The nitrogen adsorption is part of the family of gas adsorption methods and it is one of the most used. These methods are suitable to characterize the porosity at the scale of gel and capillary pores. The physical principle exploited in this analysis is the weak interaction between nitrogen molecules due to the Van der Waals forces, which are used to create layers of condensed nitrogen on the pore surface until saturation.
Aligizaki [4] reports that gas adsorption methods are reliable to study micropores and mesopores having a diameter inferior to 10 nm (100Å). According to the classification proposed by Mindness et al. reported in fig.3.6, the pores formed by the C(A)SH gel have diameters inferior to 10 nm (100Å) while capillary pores are comprised between 2.5 nm (25Å) and 10 μm (100,000 Å). In the interpretation of the results some attention has to be paid because there is a superimposition between the diameter ranges of gel and capillary pores. In any case the pore volume associated to diameters below 10 nm should increase in time because of the formation of C(A)SH.
Bajja [36] used nitrogen adsorption to evaluate the effects of the addition of silica fume in CEMI pastes and mortars and focused on the pores having diameter $<$ 6 nm (60Å) to have an estimation on the quantity of produced C(A)SH. The drying method that Bajja used the Freeze-drying technique, consisting in vacuum drying at 6.10^{-4} mbar for 7 days after immersion in liquid nitrogen at 77K. This technique is reported to preserve the pores having diameter below 5 nm (50Å).

Sample preparation and analysis procedure Being based on the use of Van der Waals forces, this analysis method requires the surface of the sample to be perfectly clean from any kind of liquid and gas. The analysis is done on mortar samples cured 7, 28 and 90 days in the wet room. The sample is grounded into powder until it passes through a $80\mu m$ diameter sieve, inserted in a tube, which has been weighed, and conserved under vacuum conditions and a temperature of 105°C for at least 12h. At the end of this phase some helium is injected in the tube to let the vacuum pressure decrease without having any interaction between the gas and the pore surface, then the tube is weighted and attached to the testing machine.
The sample preparation is a crucial aspect of this kind of test because an excessively aggressive treatment in terms of drying temperature and vacuum pressure may damage the pore structure and cause the decomposition of some products. Hunnicut[38] in his master thesis synthesized C-S-H and C-(A)-S-H and, after drying at 50°C and 472 mmHg (18 inHg in the original document), he performed DTGA analysis which showed that relevant losses of mass before 105°C. The evaporation of interlayer water occurs between 50 and 200°C, reaching its peak at 120-160°C [24]. Being the adopted drying temperature 105°C we have to conclude that the results obtained are not very reliable in following the progress of the hydration process because we cannot quantity the C(A)SH decomposed during the drying.
The typical test apparatus uses nitrogen and helium as gasses to inject in the sample and boiling-point nitrogen to keep the sample at constant temperature during the test. The typical testing apparatus follows the scheme in fig.3.8 and the following analysis steps:

1. injection of helium into a vessel of known volume and measure of its temperature and pressure

2. the helium is released in the specimen tube and, measuring the pressure change, the dead volume in the sample tube is calculated

3. helium is removed by the vacuum pump and nitrogen is injected in the calibration tube and the pressure is measures, then it is left expanding in the sample tube; the pressure is measured every 5 minutes and if it changes of less than 13.3 Pa equilibrium is considered to have been reached

4. knowing the volume of injected nitrogen and the one in the dead space and in the connectors, the volume of adsorbed nitrogen can be easily computed

5. the steps are repeated by progressively increasing the vacuum pressure

6. desorption is done in the same way by decreasing the vacuum pressure

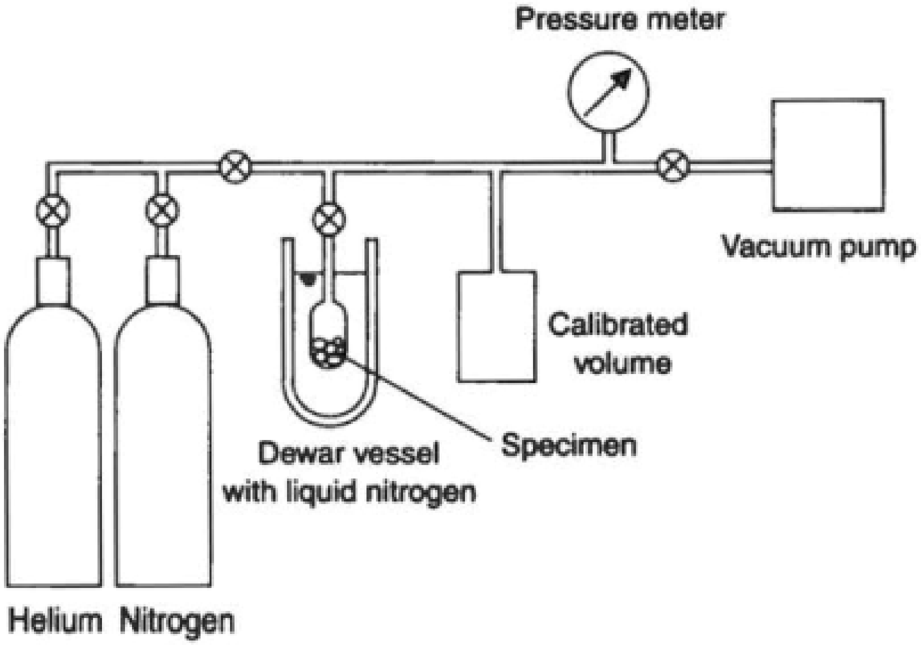

Figure 3.8: Function scheme of a nitrogen adsorption test apparatus[2]

The adsorption isotherms The result of the analysis is the *adsorption isotherm*, which is the curve of the adsorbed volume of nitrogen vs. the vacuum pressure. The IUPAC has proposed a classification of the adsorption isotherms in 6 types based on their shapes and the presence of hysteresis between the adsorption and the desorption paths. Referring to fig.3.9 the 6 types proposed by IUPAC are:

Type I the adsorbed nitrogen forms a monolayer of molecules and capillar condensation does not occur

Type II multilayer physical adsorption on a non-porous solid

Type III solids characterized by macropores

Type IV solids having both macropores and mesopores

Type V solids having micropores and mesopores

Type VI non-porous solids having uniform outside surfaces

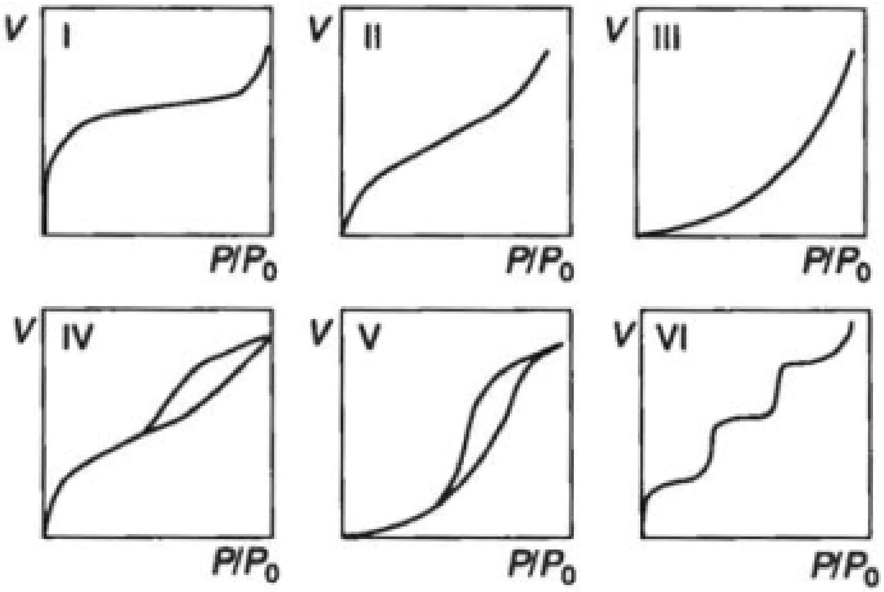

Figure 3.9: Types of adsorption isotherms according to the IUPAC classification[2]

The parts composing an adsorption, shown in fig.3.10, can be associated to different phases of the adsorption process:

- The segment AB represent the formation of a thin layer of adsorbate on the pore walls
- The segment BC is the multi-layer adsorption phase
- The point C can be found around 0.4 P/P_0 and represents the beginning of the hysteresis
- The segment CDE represents the capillary condensation of the gas, until the point E of saturation
- The point E is the complete filling of the pores with the gas
- The segment EGC is the desorption path which is coincident with the adsorption path after point C

Thickness of the adsorbed film Theoretically it is defined as:

$$t = \frac{V_s}{V_m} \cdot \tau \tag{3.3}$$

where V_s is the the volume of gas adsorbed (mm^3/g), V_m is the volume of adsorbed nitrogen when the entire surface is covered by a monomolecular layer of gas (mm^3/g) and τ is the thickness of the monomolecular layer.
t is a function of the pressure and many experimental curves have been proposed for different adsorbates and adsorbants.

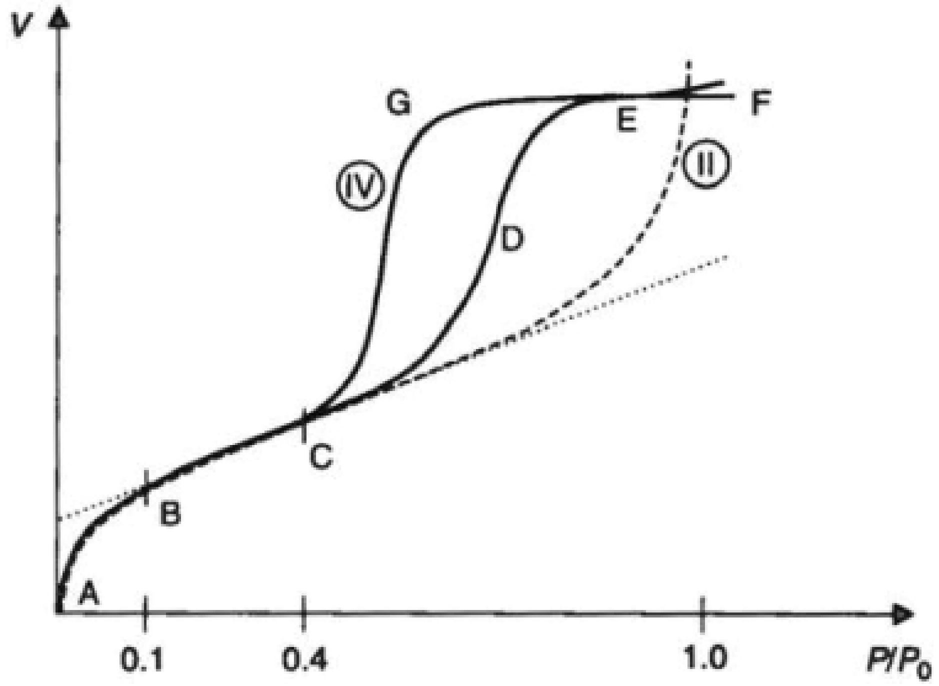

Figure 3.10: Example of a typical adsorption isotherm of Portland cement pastes

Pore size: the Kelvin equation This equation is applicable to mesopores and is based on the following assumptions:

1. the gas is ideal
2. the condensed liquid is incompressible
3. the molar volume of the liquid phase is negligible compared to the molar volume of the gas

If the adsorbate is nitrogen the equation can be written as:

$$r_k = \frac{-4.15}{\log P/P_0} \cdot 10^{-10} \quad [m] \tag{3.4}$$

The great limit of this equation is to consider only the capillary condensation which is not the sole mechanism acting in the gas adsorption process. To correct this equation the thickness of the adsorbed film is added, assuming that in the desorption phase any pore smaller that $\mathrm{r_k}$ is completely filled:

$$r_p = r_k + t \quad [m] \tag{3.5}$$

Pore size distribution: the Barrett-Joyner-Halenda (BJH) method This method is used to determine a reliable pore size distribution and is based on the following assumptions:

1. the pores have cylindrical shape

2. the pore radius is determined with the corrected Kelvin's equation using the t-curve proposed by Shull
3. the thickness of the adsorbed layer inside the pore is the same as it was on a flat surface
4. all the pores are filled at $P/O_0 = 1$

The pores are divided into groups according to their sizes and all the pores in each group are assumed to have the average radius r_p. The desorption branch of the isotherm between a relative pressure of 0.967 and the end of the hysteresis loop is considered as a series of steps and the amount of adsorbate removed between each steps is divided inner pore emptying and film thinning process, using the corrected Kelvin's equation and the Shull t-curve. The pore core calculated is associated to one of the pore groups defined at the beginning. The total pore volume can be calculated by summing the values at each pressure step. The cumulative pore volume is then derived with respect to the logarithm of the pore diameter obtaining the pore size distribution.
The average diameter of gel pores corresponds to the position of a spire-like peak in the dV/dlog(D) graph which, in the case of C-S-H generated from ordinary Portland cement hydration, occurs between 30 and 40 Å[36].

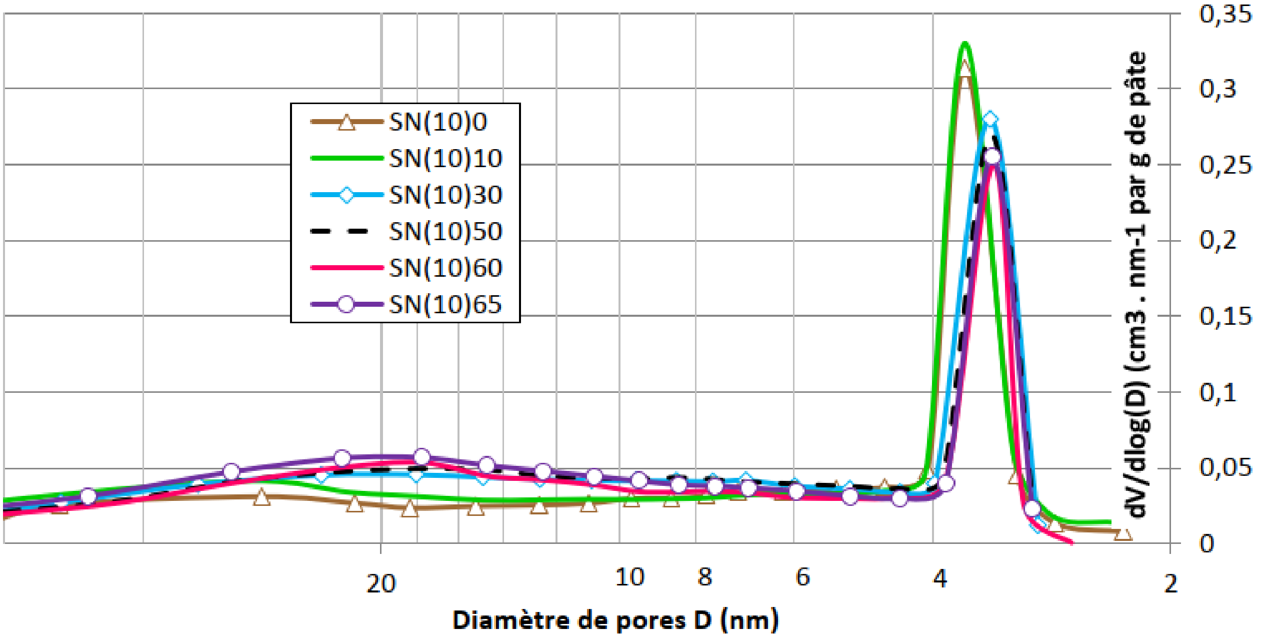

Figure 3.11: Pore size distribution of portland cement + silica fume mortar [36]

Specific surface area: the Brunauer-Emmett-Teller (BET) theory This method assumes that:

1. the solid surface is energetically homogeneous
2. no adsorbate-adsorbant interaction is present
3. the properties of the adsorbed layers do not change after the adsorption of the first layer

4. the heat of adsorption of the second and higher layers is equal to the heat of liquefaction
5. the number of layer at saturation is infinite
6. at dynamic equilibrium the number of molecules evaporating from a layer is equal to the number of molecules condensing in the layer below

After the last assumption the evaporation and condensation rates have been equated, obtaining:

$$\frac{P/P_0}{V(1-P/P_0)} = \frac{1}{V_m C} + \frac{C-1}{V_m C} \cdot P/P_0 \tag{3.6}$$

The equation represents a straigth line and the parameters V and P/P$_0$ can be taken from the adsorption isotherm. The parameters defining the straight line are called $s = \frac{C-1}{V_m C}$ and $i = \frac{1}{V_m C}$. From these relations we can obtain V$_\mathrm{m}$. The specific surface area is defined as:

$$S_{BET} = \frac{V_m N_A A_m}{V_M} \cdot 10^{-20} \quad [m^2/g] \tag{3.7}$$

where A$_\mathrm{m}$ is the average area occupied by on molecule of adsorbate in the completed monolayer (m^2/molecule), V$_\mathrm{M}$ is the molar volume (m^3/mol), N$_\mathrm{A}$ is the Avogadro number. When nitrogen is used the equation 3.7 becomes:

$$S = \frac{(6.023 \cdot 10^{23}) \cdot (16.2 \cdot 10^{-20} \cdot V_m)}{22.4 \cdot 10^{-3}} = 4.35 \cdot V_m \cdot 10^6 \tag{3.8}$$

3.4.4 Water porosity test

The nitrogen adsorption method provides information on micropores and the smallest mesopores, but not on larger pores and voids which have the highest influence on strength and diffusivity. This scale of pores can be studied with the water adsorption test which, as shown in fig.3.7, is suitable for a large range of pore size and has the advantage to need a very simple test apparatus and chemical products that are not dangerous to hold, contrary to nitrogen which requires a lot of precautions.

The preparation of the sample and the test have been done according to the standard NF P 18-459[59]. The sample is a cylinder of mortar of diameter 4 cm and 3 cm high, that has been considered big enough to be representative of the material, cured 90 days in wet room. The samples have been inserted in a vacuum dessicator and a vacuum pump has kept the pressure below 25 mbar for 4 hours. Then water has been injected into the desiccator until the samples where covered by water. The samples have been kept under water in vacuum conditions for 44 hours. Once the gas elimination and saturation phases had been completed the samples have been weighted with an hydrostatic balance, obtaining the quantity m$_\mathrm{w}$, then their surfaces have been dried with a towel and the samples have been weighed with a precision balance, obtaining thus m$_\mathrm{a}$. After that the samples have been put in a oven set to a temperature of 105°C and left drying until the stabilization of the mass, obtaining m$_\mathrm{d}$. The accessible water porosity and apparent density have been calculated according to the formulas:

$$\rho_d = \frac{m_d}{m_a - m_w} \cdot \rho_w \tag{3.9a}$$

$$\epsilon = \frac{m_a - m_d}{m_a - m_w} \cdot 100 \tag{3.9b}$$

3.5 Study of the reaction kynetics and physical properties

3.5.1 Isothermal calorimetry

This technique is used to study the reaction heat of chemical products and cement pastes. The reagents are mixed in a plastic container which is inserted into the test machine. The calorimeter keeps the temperature constant and measure the heat power necessary to do so. Once the heat power has been stabilized the test is stopped and the reaction heat can be calculated as the integral of the heat power in time.

This test has been done only on the two quicklimes used (calcinated and non-calcinated) and the MgO mixing 10 g of powder with 40 g of water. The test allows us to evaluate the reactivity of the product and the rate of hydration once the reaction has been extinguished.

The used test machine is a Calmetrix I-Cal 2000 HPC.

3.5.2 Semi-adiabatic calorimetry

This alternative technique allows to measure the hydration heat of a cement on a mortar sample and not on a paste sample.

The testing apparatus is a Controlab Langavant L0071.1 and complies with the norm NF EN 196-9:2010. It is composed by two calorimeters, one for the mortar sample and the other one as reference. The mortar is deposed in a steel cylindrical container and inserted in the test calorimeter. Thermometers are introduced in both the calorimeters and the temperatures of the two are monitored at constant time steps until stabilization. The room temperature is kept at 20°C.

The hydration heat is calculated using the equation:

$$Q = \frac{C}{\theta_t} + \frac{1}{m_c} \sum_{i=1}^{N} \bar{\alpha_i} \cdot \bar{\theta_i} \cdot \Delta t_i \tag{3.10}$$

where:

- C is the total heat capacity of the system (J/K)
- m_c is the mass of binder (g)
- θ_t is the difference between the temperature of the essay and the reference (K)
- $\bar{\theta_i}$ is the average θ_t calculated between to subsequent time steps
- $\bar{\alpha_i}$ is the average heat dispersion coefficient

$\bar{\alpha_i}$ is calculated as $\bar{\alpha_i} = a + b \cdot \bar{\theta}_i$, where a = 62.9 and b = 0.065 are two calibration constants given by the manufacturer.
The total heat capacity of the systems is the sum between the heat capacities of all the components:

$$C = c_{BFS} \cdot m_{BFS} + c_a \cdot m_a + c_s \cdot m_s + c_w \cdot m_w + c_b \cdot m_b + \mu \tag{3.11}$$

where c are the mass specific heat (J/mol K) and m are the mass of the components:

- BFS stands for the GGBFS
- a stands for the activator
- s stands for the sand
- w stands for the water
- b stands for the metal box
- μ is the heat capacity of the calorimeter provided by the producer

In three compositions mixes of different products are used as activators (the uncalcinated quicklime is considered as a CaO + $Ca(OH)_2$ + $CaCO_3$ mix). In this case c_a is the sum of the specific heats each one multiplied by its percentage in mass.
The adopted values are resumed in table 3.3.

Table 3.3: Heat capacities

Product	Heat capacity	Unit of measure	Source
GGBFS	1.05	J/g K	[33]
CaO	0.753	J/g K	[45]
$Ca(OH)_2$	0.996	J/g K	[44]
$CaCO_3$	0.834	J/g K	[43]
MgO	0.922	J/g K	[49]
CEMI	0.8	J/g K	NF EN 196-9
Water	3.8	J/g K	NF EN 196-9
Sand	0.8	J/g K	NF EN 196-9
Steel box	0.5	J/g K	NF EN 196-9
Calorimeter	673	J/K	Manufacturer

3.5.3 Ultrasonic study of the hardening process and research of the setting times

The setting phase is the interval of time during which the cement paste completely looses its plasticity. Identifying the initial and the final setting times is important to study the reactivity of the binder and its hydration kinetics.
The method used in the present study is based on the monitoring of the speed of ultrasonic waves in a mortar sample. The fresh mortar is deposed in a cylindrical shaped chamber 8 cm

diameter and 4 cm high provided with an ultrasonic wave emitter and a receiver at the two extremities. An ultrasonic wave is produced at regular time intervals and its flight time is measured to compute the velocity according to the norm NF EN 12504-4:2021[55].
The exploitation of the results follows the procedure suggested by Robeyst, Gruyaert, and De Belie[30] and consists in fitting the ultrasonic wave velocity curve with a tri-logistic function using the least squares method:

$$v(t) = \sum_{i=1}^{\infty} \frac{k_i}{1 + \exp{(t - t_i)/dt_i}} + c \tag{3.12}$$

3 logistics curves are usually enough to reach a good fitting. The fitting function is derived two times and the two setting times are associated to the points of inflection of the curve.

3.5.4 Measure of the delayed deformations

The delayed deformations of shrinkage or expansion have been measured on prismatic mortar samples having dimensions 4 x 4 x 16 cm and two pegs in the middle of the two bases to allow the insertion of a metal spherical ball. For each composition the w/b 0.55 has been kept and the same quantity of sand has been used, in order to have the same quantity of paste. The reference composition to decide the quantity of sand is CaO d 10%. 6 samples have been fabricated for each compositions:

- 3 samples have been sealed in aluminum paper after demolding and cured in controlled atmosphere at temperature 20°C and RH 50
- 3 samples have been cured in the wet room

The sealed samples are shown in fig.3.12.
For each sample 3 measures of length and mass have been taken during the first day, 1 measure per day for the first week and then 1 measure per week.
The deformation is computed as:

$$\epsilon = \frac{l(t) - l_0}{l_0} \cdot 10^6 \quad [\mu m/m] \tag{3.13}$$

And the mass variation is expressed as percentage of the initial mass:

$$\Delta m = \frac{m(t) - m_0}{m_0} \quad [\%] \tag{3.14}$$

3.5.5 Measure of the pH

The pH of the cement paste has been measured by water dissolution. 2 g of powder have been agitated for 24h with 20 g of distilled water, then left rest 1 h to allow the fine particles to depose. After calibration the ph meter is inserted in the sample without touching the solid part deposed at the bottom and the ph is measured.

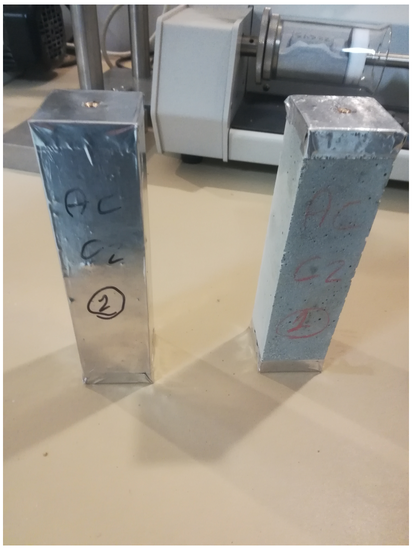

Figure 3.12: Samples used in the measure of delayed deformations

3.6 Mechanical tests

3.6.1 Description of the samples, fabrication procedure and curing conditions

The samples used for these tests have a prismatic shape and dimensions 4 cm x 4 cm x 16 cm. The standard describes also the characteristics of the molds. The mold is required to be made of steel and have a Vickers hardness of al least 200 HV. The tolerances on the dimensions of the compartments are the following:

length $(160 \pm 1)\ mm$

width $(40.0 \pm 0.2)\ mm$

depth $(40.1 \pm 0.1)\ mm$

In our case we have used PVC molds that are conform to the standard on the dimension side but not on the required hardness.
The mortar has been inserted into the molds in two layers and vibrated 5 s after the insertion of each layer to ensure an optimal compaction.
The requires requires to keep the mold in a room with temperature constant to $(20.0 \pm 1.0)\ C$ for 24h, then the samples should be demolded and cued in water for the remaining curing time. We have not decided to follow this procedure for two reasons:

1. some of the compositions are too weak to be demolded after 24h, so it was necessary to demold after 48h
2. the compositions uses alkali-activated BFS, so we have decided not to take the risk to disperse the ions in water

The curing method adopted is thus characterized by demolding after 48h and then storing the samples in the wet room.
The adopted curing ages are 3, 7, 28 and 90 days.

3.6.2 Estimation of the Young's elastic modulus through ultrasonic waves

The Young's elastic modulus and the Poisson's ratio are two direct expressions of the stiffness of a material and for this reason they are very important in all the disciplines that rely on solid mechanics and theory of elastic continuum.
The Young's modulus can appear in two forms according to the type of action of the material: the so-called "static Young's modulus" and the "dynamic Young's modulus". The first one is used in the applications of structural mechanics and design because it represents the stiffness of the material to quasi-stationary actions; the second one is related to the speed of propagation of compressive waves inside the material.
Measuring the static Young's modulus requires a destructive test as the one described by the standard *NF EN 12390-13* [54]. On the contrary the determination of the dynamic modulus can be done with a non-destructive test based on the propagation of ultrasonic waves; for this reason finding a relation between dynamic and static Young's modulus is very interesting to estimate the second one through non-destructive essays.
[14] proposed a model relating the two parameters with application to the geomaterials:

$$E_s = E_d(1-\phi) - 3\ln\phi \tag{3.15}$$

where:

- E_s is the static Young's modulus
- E_d is the dynamic Young's modulus
- ϕ is a parameter depending on the porosity of the medium

In the present study we will not analyze more deeply the relation between the two quantities but we will stop at the dynamic modulus for the compositions of mortars.

Operating procedure

The test has been performed according to the standard is *NF EN 12504-4* [55] using a Socomate International USPC 7100 I PCI testing apparatus. The pulser and the receiver are disposed for direct transmission on opposite faces of the mortar sample as shown in fig.3.13; some glycerol is put between the samples and the electrodes in order to allow a good transmission of the ultrasonic waves.

The ultrasonic waves generated by the pulser are compressive p-waves and lateral s-waves; just the first ones will be considered. The speed is calculated diving the width of the sample, measured with a caliper, by the flying time measured by the instrument.
The dynamic elastic modulus is calculated as follows [41]:

$$\frac{(1+\nu)(1-2\nu)}{1-\nu}\,\rho^2 \tag{3.16}$$

The density of the material ρ is calculated as the ratio between the mass of the sample and the volume, calculated by measuring the dimensions of the samples with a caliper. The Poisson's ratio ν is taken equal to 0.2.

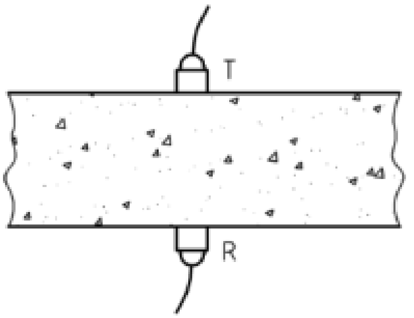

Figure 3.13: Position of the pulser and the receiver for flying time measure[55]

3.6.3 Compressive and flexural strength tests

These tests are aimed to determine the compressive and flexural strength of a cement by using standardized mortar samples. The reference is the norm *NF EN 196-1* [56].

Description of the flexural strength test

According to the norm the charge is applied in 3 points as shown in fig. 3.14

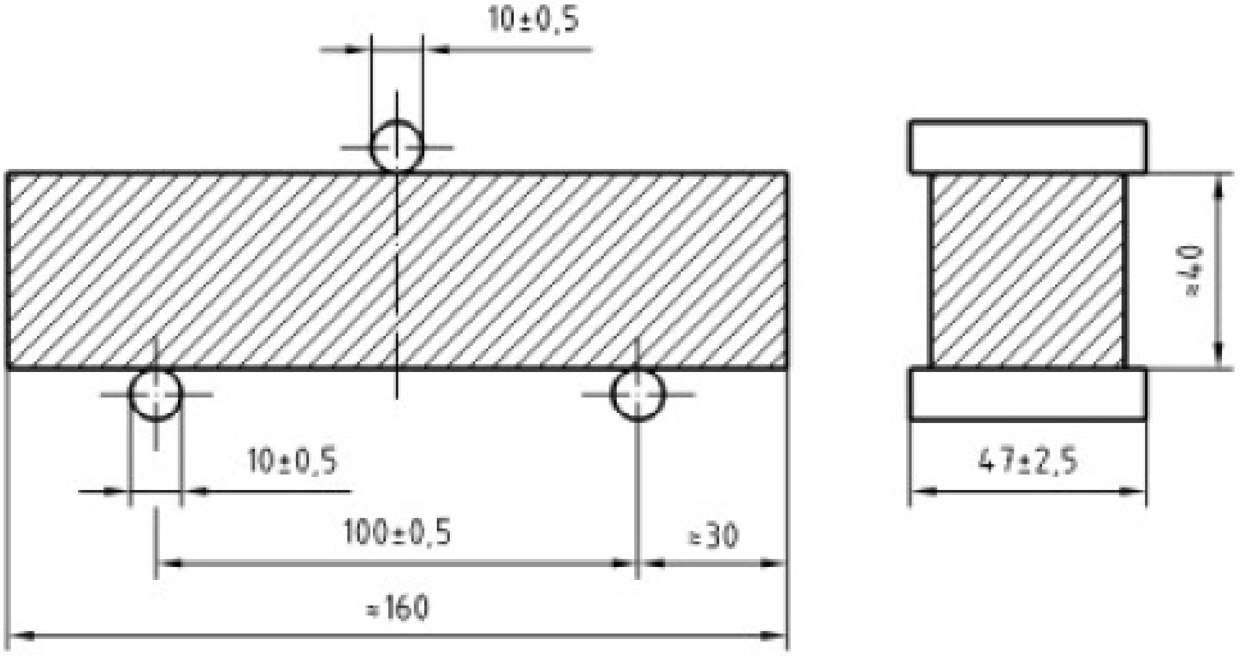

Figure 3.14: Three points flexural strength test according to *NF EN 196-1* [56]. Dimensions in mm

The testing machine must be able to apply a force up to 10 kN with a precision of ±10% of the measured load; the force must be applied with a speed equal to $(10.0 \pm 10)\ kN/s$.
The flexural strength is calculated using the following equation:

$$\sigma_f = \frac{1.5\, F_f\, l}{b^3} \tag{3.17}$$

where:

- σ_f is the strength in MPa
- b is the width of the sample in mm
- F_f is the applied force at rupture in N
- l is the distance between the supports in mm

Description of the compressive strength test

The compressive strength test is done by applying a force increasing at a speed equal to $(2400 \pm 200)\ N/s$. The plates used to apply the force on the samples must be made of tungsten carbide or tempered steel and have a Vickers hardness superior to 600 HV. Their thickness must be at least 10 mm and the other two dimensions $(40.0 \pm 0.1)\ mm$.
All the components of the machinery must be aligned complying to the tolerances indicated by the norm.
The compressive strength is calculated as:

$$\sigma_C = \frac{F_C}{1600} \tag{3.18}$$

where:

- σ_C is the compressive strength in MPa
- F_C is the applied force in N
- 1600 m^2 is the area of the plates applying the load

Description of the experimental apparatus

The machinery used in the present study is a double press Controlab (ref. E0183), able to perform both flexural and compressive strength tests up to respectively 15 and 250 kN. The jigs are Controlab E0170 for the compressive test and Controlab E0171 for the flexural test.
The characteristics of the machine, of the jigs and their function during the essays comply to the norm *NF EN 196-1* [56].

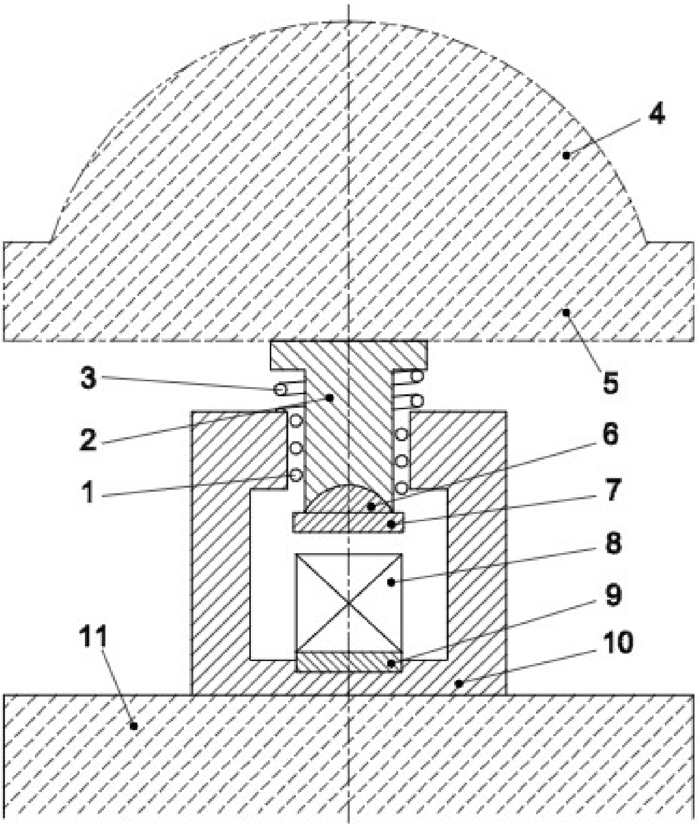

Key

1	ball bearings
2	sliding assemble
3	return spring
4	spherical seating of machine
5	upper platen of machine
6	spherical seating of the jig
7	upper platen of the jig
8	specimen
9	lower platen of the jig
10	jig
11	lower platen of the machine

Figure 3.15: Typical jig for compressive strength test according to *NF EN 196-1* [56]

Chapter 4

Characterization of the precursors

4.1 Characterization of the GGBFS

The ground granulated blast furnace slag that has been used is produced by Ecocem France in Dunkerque and its characteristics, as communicated by the manufacturer, are shown in fig.4.1. The BFS complies to the standard EN 15 167-1 and EN 206/CN.

In order to check the reliability of the provided information the XRD analysis, the TGA and the nitrogen adsorption test have been performed.

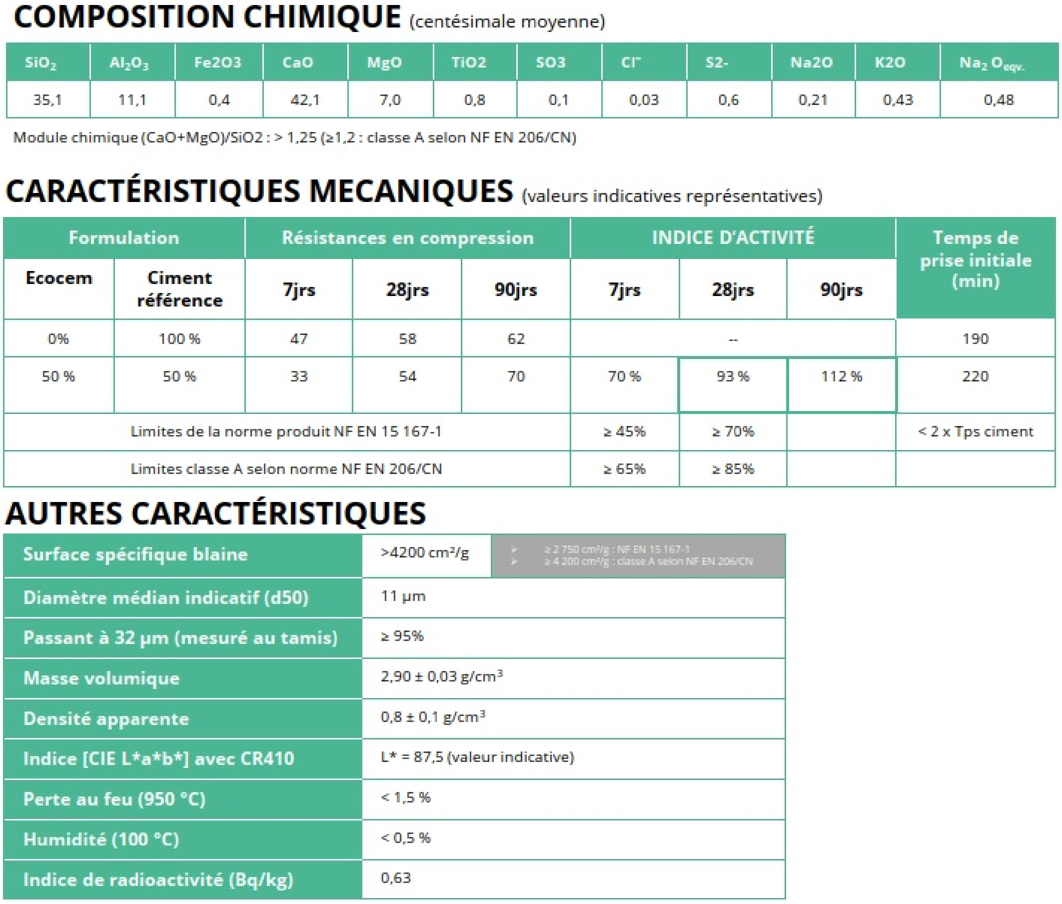

COMPOSITION CHIMIQUE (centésimale moyenne)

SiO_2	Al_2O_3	Fe2O3	CaO	MgO	TiO2	SO3	Cl^-	S2-	Na2O	K2O	$Na_2O_{eqv.}$
35,1	11,1	0,4	42,1	7,0	0,8	0,1	0,03	0,6	0,21	0,43	0,48

Module chimique (CaO+MgO)/SiO2 : > 1,25 (≥1,2 : classe A selon NF EN 206/CN)

CARACTÉRISTIQUES MECANIQUES (valeurs indicatives représentatives)

Formulation		Résistances en compression			INDICE D'ACTIVITÉ			Temps de prise initiale (min)
Ecocem	Ciment référence	7jrs	28jrs	90jrs	7jrs	28jrs	90jrs	
0%	100 %	47	58	62	--			190
50 %	50 %	33	54	70	70 %	93 %	112 %	220
Limites de la norme produit NF EN 15 167-1					≥ 45%	≥ 70%		< 2 x Tps ciment
Limites classe A selon norme NF EN 206/CN					≥ 65%	≥ 85%		

AUTRES CARACTÉRISTIQUES

Surface spécifique blaine	>4200 cm²/g	≥ 2 750 cm²/g : NF EN 15 167-1 ≥ 4 200 cm²/g : classe A selon NF EN 206/CN
Diamètre médian indicatif (d50)	11 µm	
Passant à 32 µm (mesuré au tamis)	≥ 95%	
Masse volumique	2,90 ± 0,03 g/cm³	
Densité apparente	0,8 ± 0,1 g/cm³	
Indice [CIE L*a*b*] avec CR410	L* = 87,5 (valeur indicative)	
Perte au feu (950 °C)	< 1,5 %	
Humidité (100 °C)	< 0,5 %	
Indice de radioactivité (Bq/kg)	0,63	

Figure 4.1: Characteristics of the BFS provided by the manufacturer

4.1.1 XRD of GGBFS

The XRD analysis has been performed on the anhydrous BFS as described in section 3.4.1. The diffractogram in fig.4.2 shows a good vitreous structure; some peaks are present around 30° but we can anyway consider reliable the value of vitrification superior to 90% given by the manufacturer.

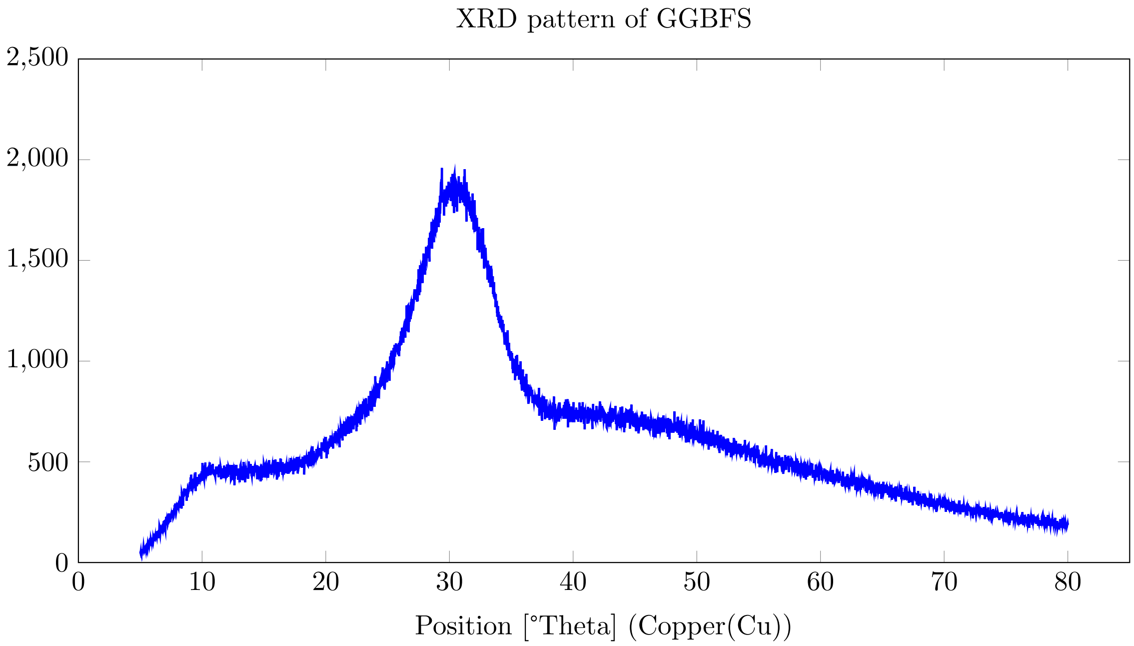

Figure 4.2: Diffractogram of anhydrous BFS

4.1.2 Loss on ignition of GGBFS

The DTGA curves in fig.4.3 does not show the presence of carbonation but some crystalization is visible in the ranges of temperature 600-700°C and over 1000°C [24]. The products does not present any relevant impurity and the loss of mass is 0.5%, below the value declared by the manufacturer.

4.1.3 Pore structure of GGBFS

In order to characterize the pore structure a nitrogen adsorption test has been done according to the procedure described at point 3.4.3.

The adsorption isotherm, shown in fig.4.4, can be classified as type I according to IUPAC, typical of adsorbent media characterized by micropores [2]. The pore size distribution determined according to the BJH method confirms the prevalence of micropores. The BET surface area amounts to 1.0329 m^2/g.

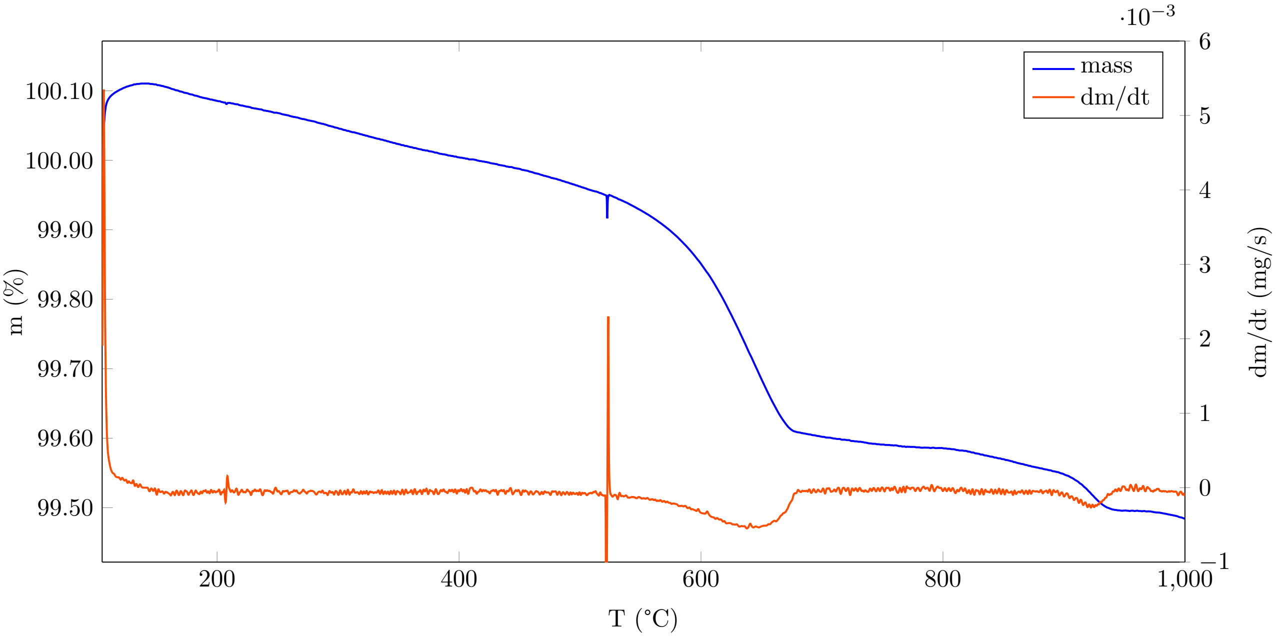

Figure 4.3: TGA curves of BFS

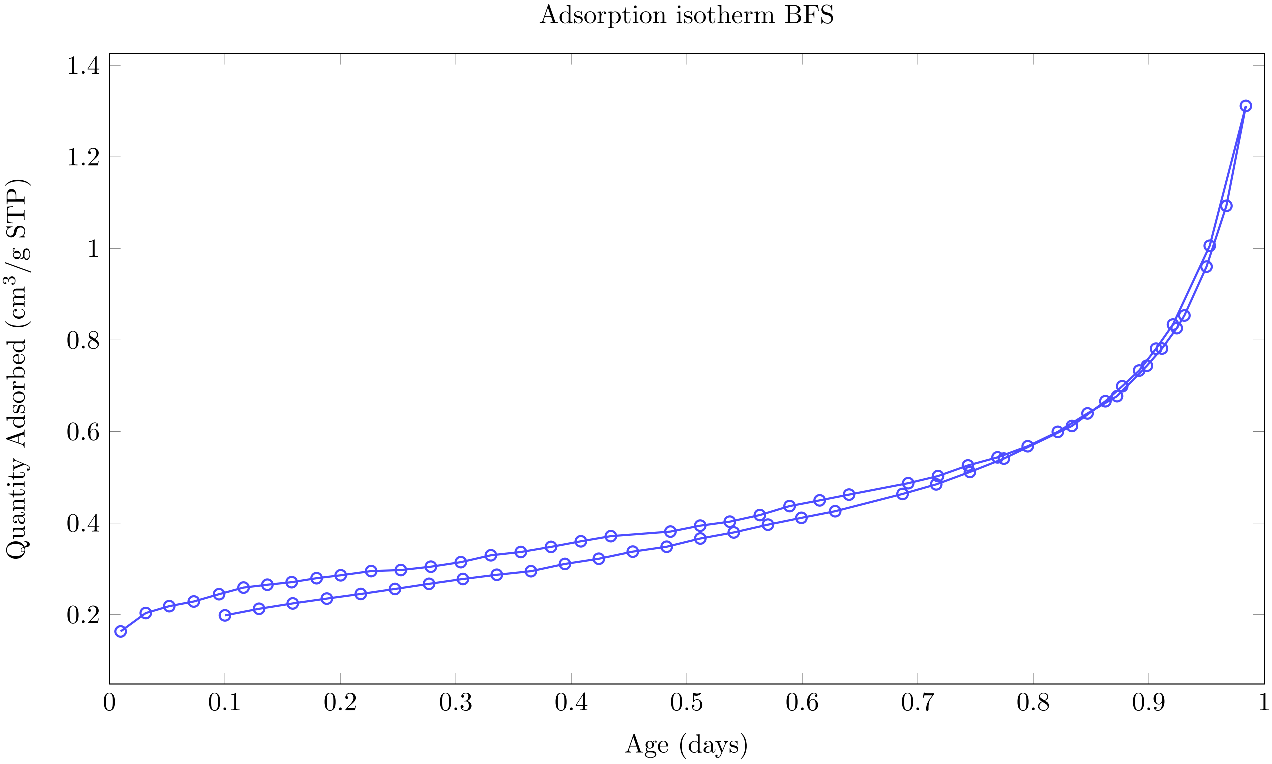

Figure 4.4: Nitrogen adsorption isotherm of BFS

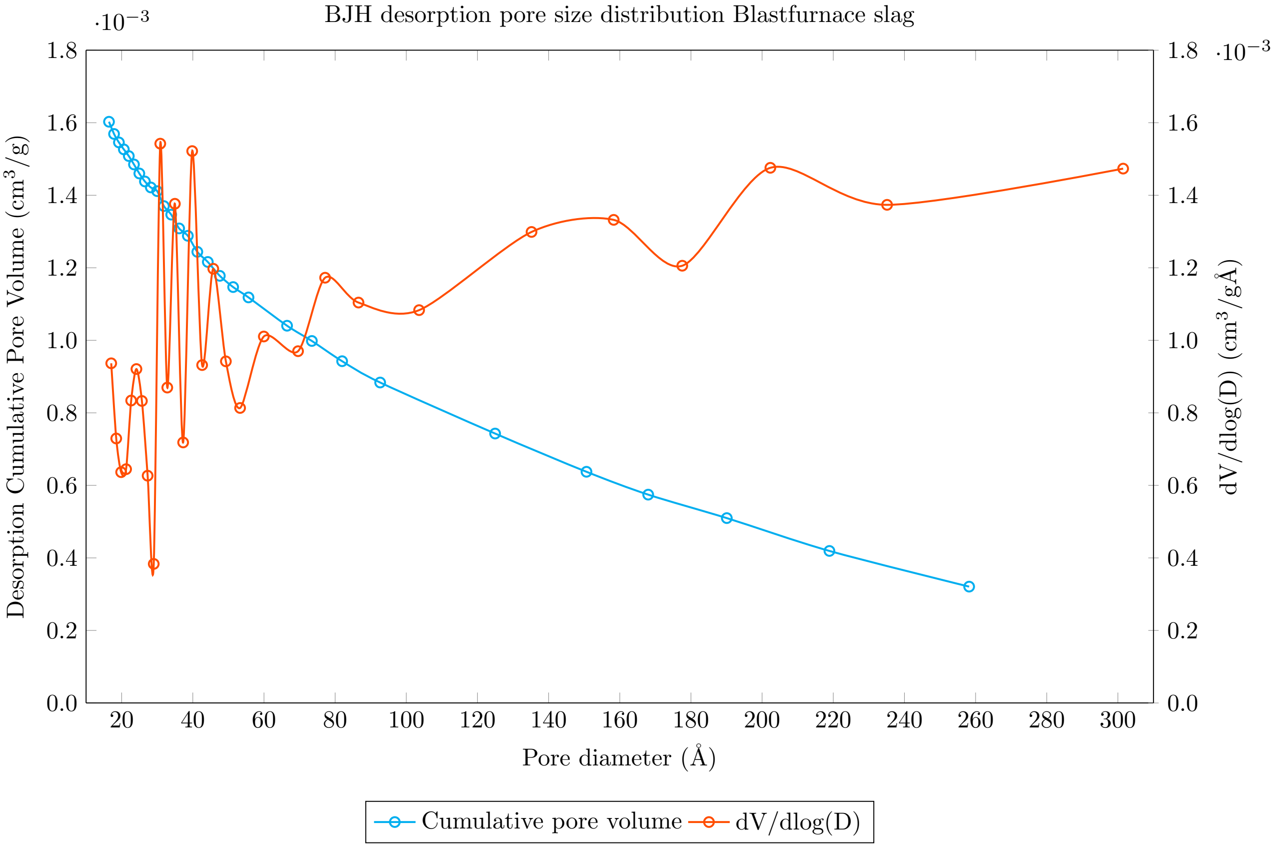

Figure 4.5: BJH pore size distribution of BFS

4.2 Characterization of the CaO

The used quicklime is produced by VWR Chemicals and corresponds to the catalog number 22645.360 and the CAS Number 1305-78-8.

4.2.1 Measure of the density

Following the procedure described in the section 3.1, we have measured a density equal to 2.925 g/cm^3 with a standard deviation of 0.053. The detailed calculation is shown in teb.4.1.

The theoretical density of CaO is 3.34 g/cm^3 [46]: the difference between the theoretical value and the experimental one shows that some impurities are present in the product.

4.2.2 Loss of mass due to impurities

The thermo-gravimetric analysis, performed as described at 3.4.2, confirms the presence of portlandite and calcite, consequence of a partial hydration and a partial carbonation of the quicklime. Knowing the decomposition reaction of $Ca(OH)_2$ and $CaCO_3$, explained in equation 4.1 and 4.2

Table 4.1: Measured quicklime density

Test	m1 [g]	m2 [g]	m3 [g]	ρ [g/cm3]
1	72.066	3.953	74.97	2.9581554
2	72.052	2.928	74.196	2.9317347
3	71.957	2.559	73.843	2.9848663
4	72.028	5.382	75.927	2.8488672
5	72	4.497	75.28	2.9006943

mean rho	2.925	g/cm3
std	0.052715	g/cm3

$$Ca(OH)_2 \rightarrow CaO + H_2O \tag{4.1}$$

$$CaCO_3 \rightarrow CaO + CO_2 \tag{4.2}$$

The first peak of the mass derivative in fig.4.6 is associated to the decomposition of portlandite while the second to calcite [24].

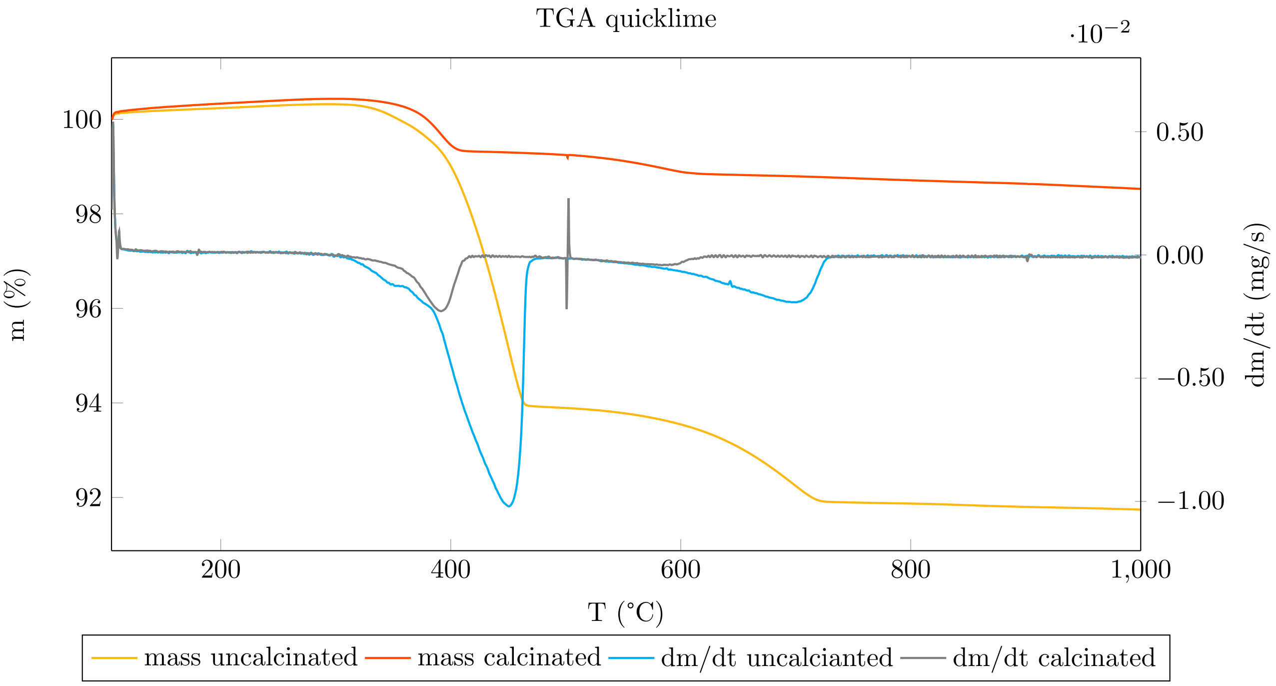

Figure 4.6: TGA curves of quicklime before and after calcination

Knowing the losses of mass corresponding to these peaks we can compute the amount of portlandite and calcite:

$$m_{portlandite} = \frac{\Delta m}{u_{H_2O}} \cdot u_{Ca(OH)_2} = \frac{6\ g/100g}{18\ g/mol} \cdot 74.1\ g/mol = 24.7\ g/100g \tag{4.3}$$

$$m_{calcite} = \frac{\Delta m}{u_{CO_2}} \cdot u_{CO_2} = \frac{1.63\ g/100g}{18\ g/mol} \cdot 100.09\ g/mol = 3.71\ g/100g \tag{4.4}$$

The important amount of portlandite is not surprising because CaO is very reactive with water and the storage conditions of this commercial product may not be in a completely dry environment. Because of these impurities this product is very different from pure CaO, so we have decided to study the effects both of pure CaO, obtained calcinating the commercial product in a oven at 900°C for 6h, and the commercial product itself when used as alkali activators. The DTGA curve of calcinated quicklime are visible in fig.4.6. By repeating the same calculations shown in equations 4.3 and 4.4 we have estimated that the amounts of portlandite and calcite are, respectively, 1.71 g/100g and 0.91 g/100g. For simplicity we have assumed this new product as it was pure CaO.

4.2.3 X-ray cristallography

XRD have been done both on the anhydrous BFS and the anhydrous binder (90% BFS + %CaO) and then, by subtracting the two diffractograms, we have obtain the one of CaO shown in fig.4.7. This test confirms the important presence of portlandite while calcite is not very visible because of its small amounts and the superimposition of its main peak with a peak of portlandite.

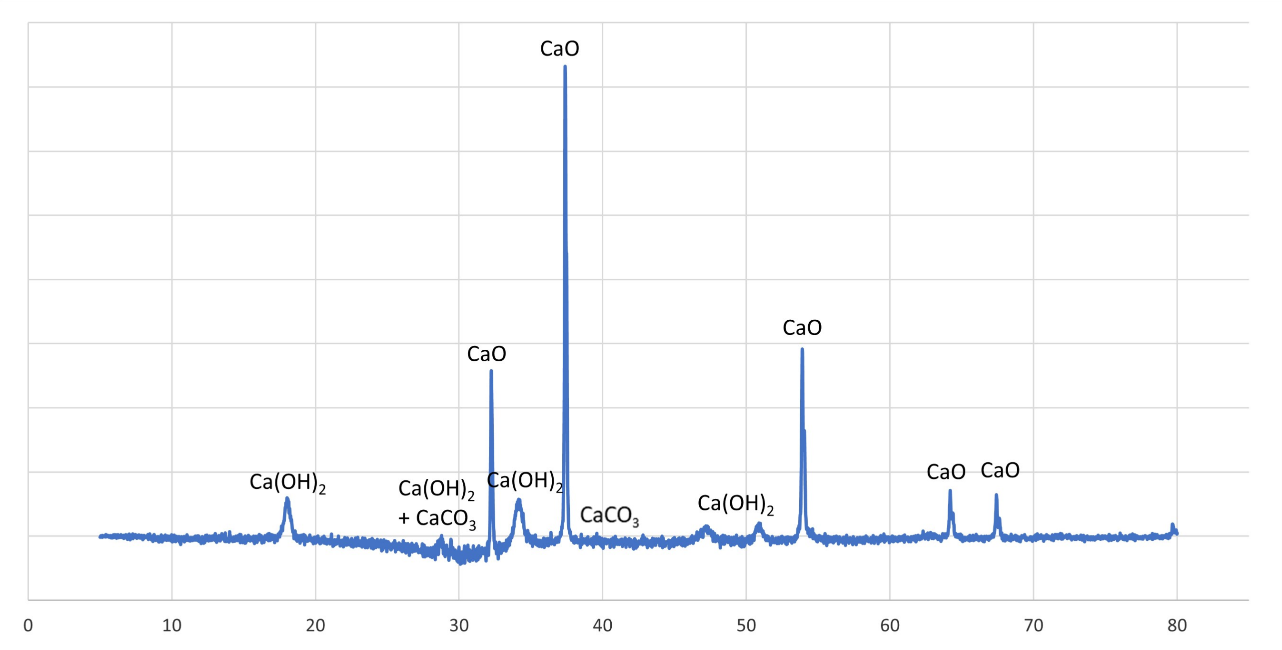

Figure 4.7: Diffractogram of commercial quicklime

The same procedure has been done for CaO after calcination and $Ca(OH)_2$ nor $CaCO_3$ are visible in its diffractogram (fig.5.3), confirming the goodness of both the calcination process both the conserving conditions and that the assumption of pure CaO is acceptable.

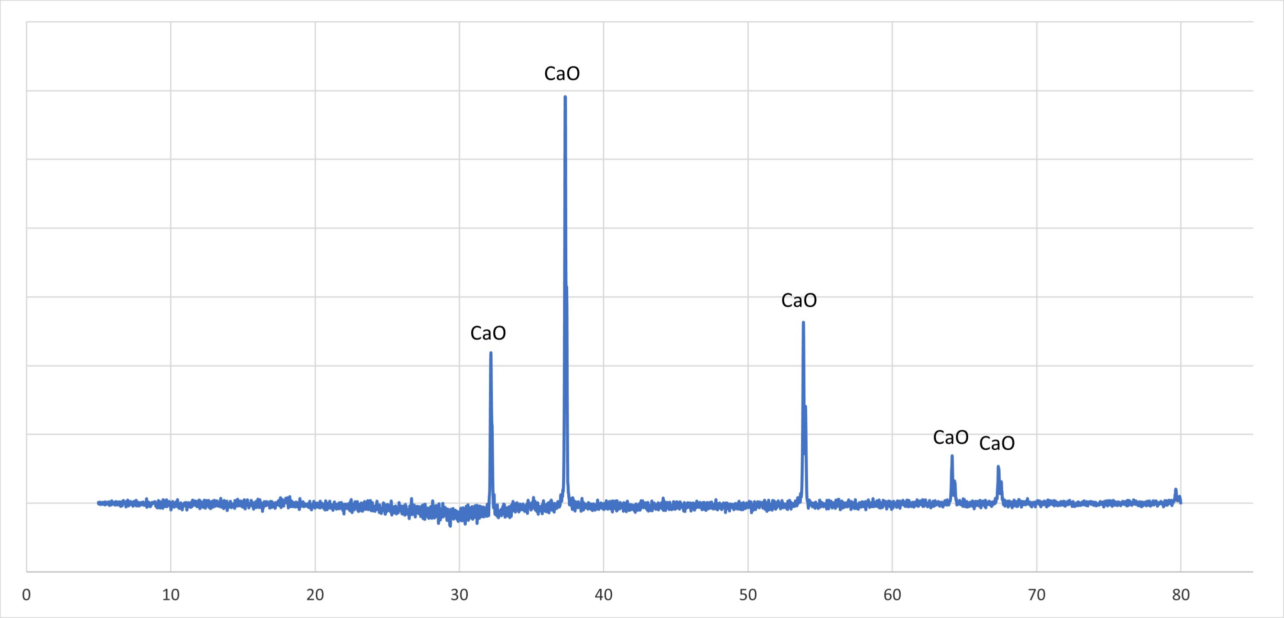

Figure 4.8: Diffractogram of quicklime after calcination

4.2.4 Pore structure

The nitrogen adsorption-desorption of both the quicklimes used gave two adsorption isotherms between type I and and II, according to the IUPAC classification [2], revealing that the materials are adsorbents characterized by micropores.

The cumulated pore volume and the pore size distribution calculated with the Barret-Joyner-Alenda method show that the prevalent size of pores is below 50 Å(fig.**??**).
The BET specific surface are is estimated to be 2.67 m^2/g for the uncalcinated lime and 2.47 for the calcinated one.
It is worth noting that the calcination procedure has not provoked significant changes in the pore structure of the quicklime.

4.2.5 Study of the reactivity through isothermal calorimetry

In order to estimate the reactivity of the quicklime the isothermal calorimetry test has been performed. Both the quicklimes are very reactive and their hydration heat has been able to saturate the calorimeter, as shown by the constant path in fig.4.10. The calcinated, as one should expect, shows higher hydration heat and the saturation phase of the instrument lasts longer. In both cases we can affirm that the hydration of the quicklime requires 2 hours. A TGA on the hydrated products showed that the content of portlandite is 92% in the case of calcinated quicklime and 89% for uncalcinated quicklime.

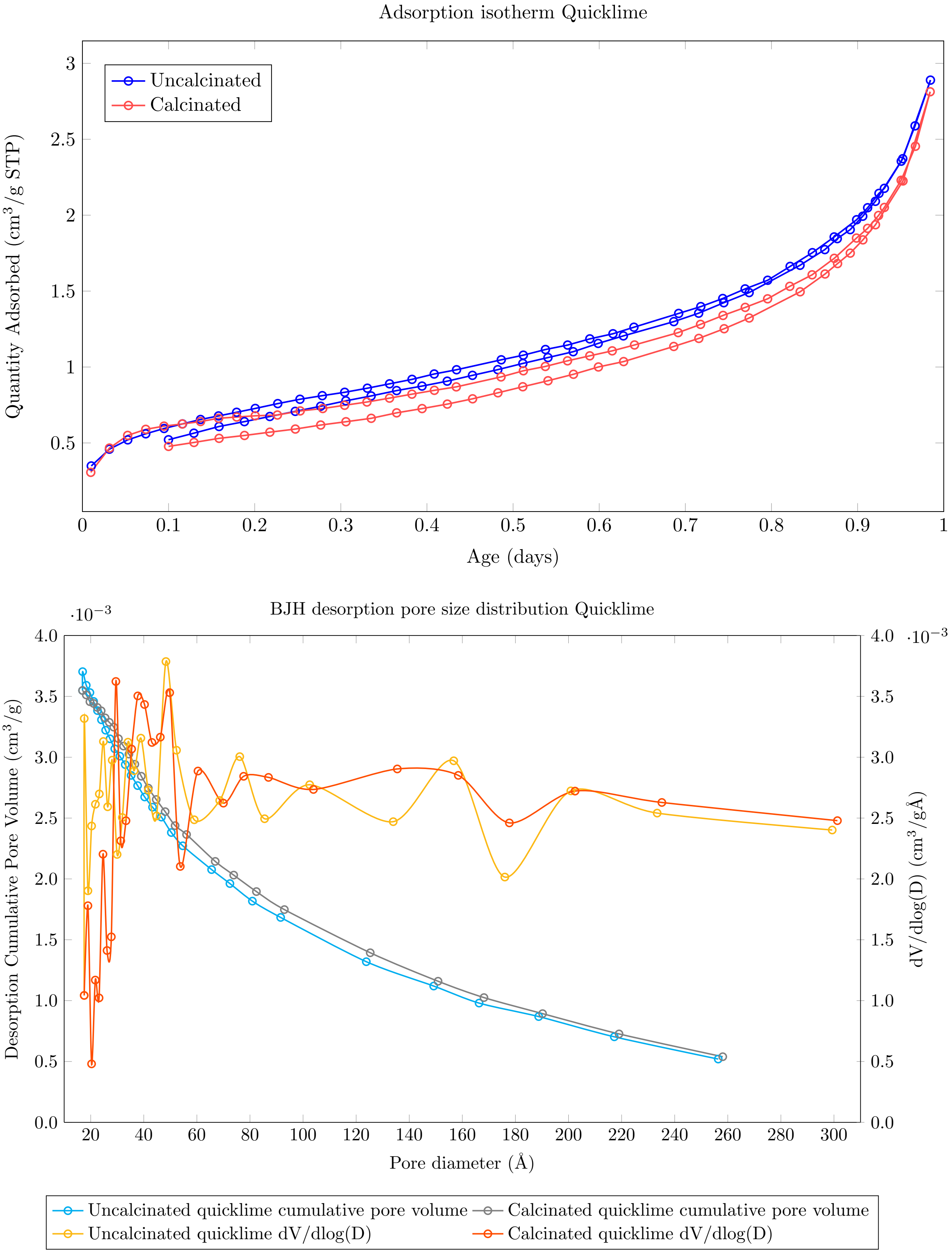

Figure 4.9: Adsorption isotherms and pore size distribution of the two quicklimes

Figure 4.10: Isotherm calorimetry of quicklime

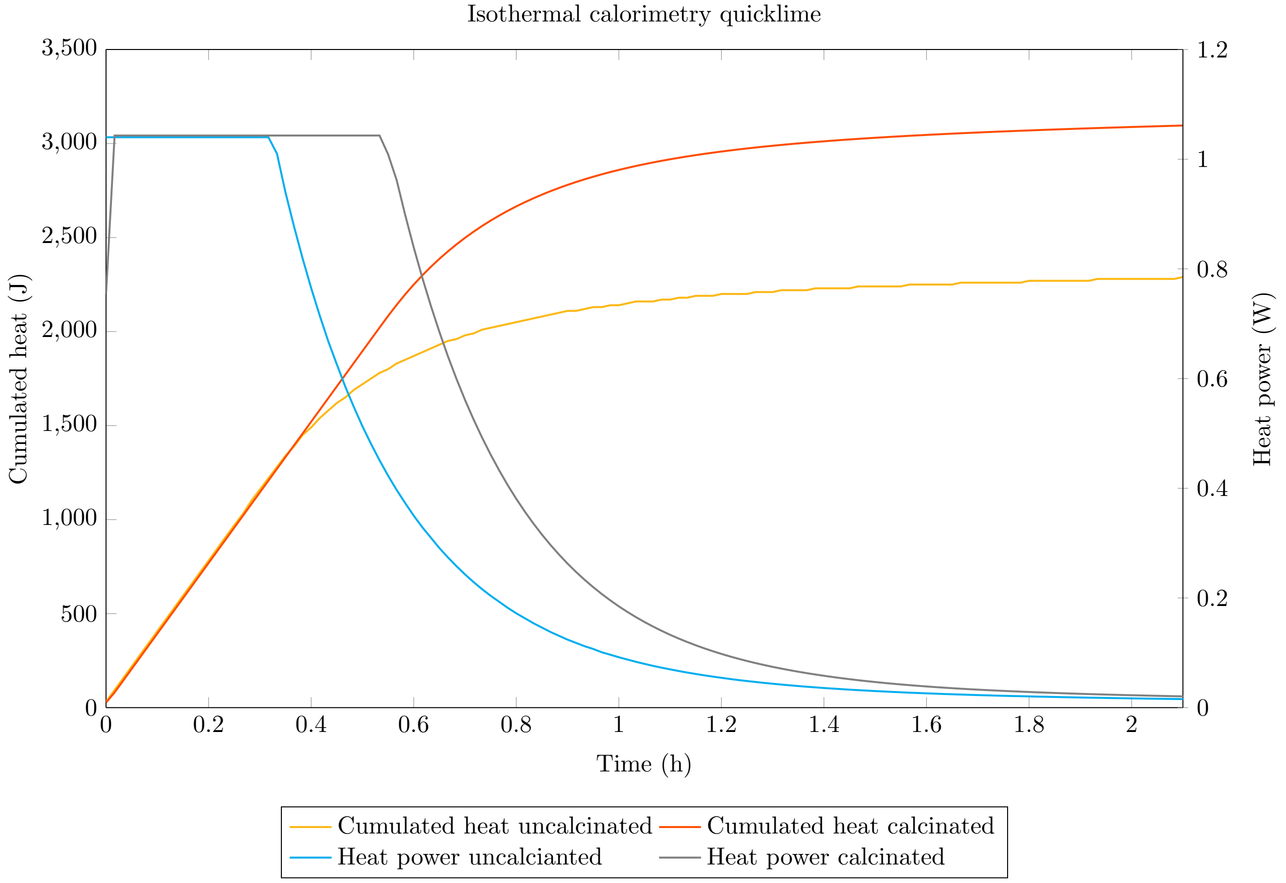

4.3 Characterization of the MgO

The used MgO product is Magnesium Oxide Light produced by VWE Chemicals and corresponds to the catalog number 25054.298 and the CAS number 1309-48-4.

4.3.1 Measure of the density

Following the procedure described in the section 3.1, we have measure a density equal to 3.35 g/cm^3 with a standard deviation of 0.085.

The theoretical density of MgO is 3.58 g/cm^3 [10]: the difference between these two values shows that some impurities are present in the product.

4.3.2 Loss of mass due to impurities

The loss on ignition is the loss of mass in percentage due to heating up to 1000-1150°C in a crucible in a laboratory furnace. The loss of mass is due to the calcination of the residual carbonate and the decomposition of the hydrates and it is both an indicator of the manufacture procedure and of the presence of impurities: the higher the LOI, the lower the temperature or the calcination time and the higher the reactivity of MgO.
A DTGA has been performed on the MgO product as described in section 3.4.2. The mass

Table 4.2: Measured MgO density

Test	m1 [g]	m2 [g]	m3 [g]	ρ [g/cm3]
1	72.034	1.295	73.021	3.300568
2	72.002	1.182	72.898	3.244301
3	71.965	1.733	73.307	3.479297
4	71.961	1.324	72.979	3.396536
5	71.964	1.604	73.186	3.296178
6	71.966	0.956	72.699	3.365291

mean rho	3.347028	g/cm3
std	0.084353	g/cm3

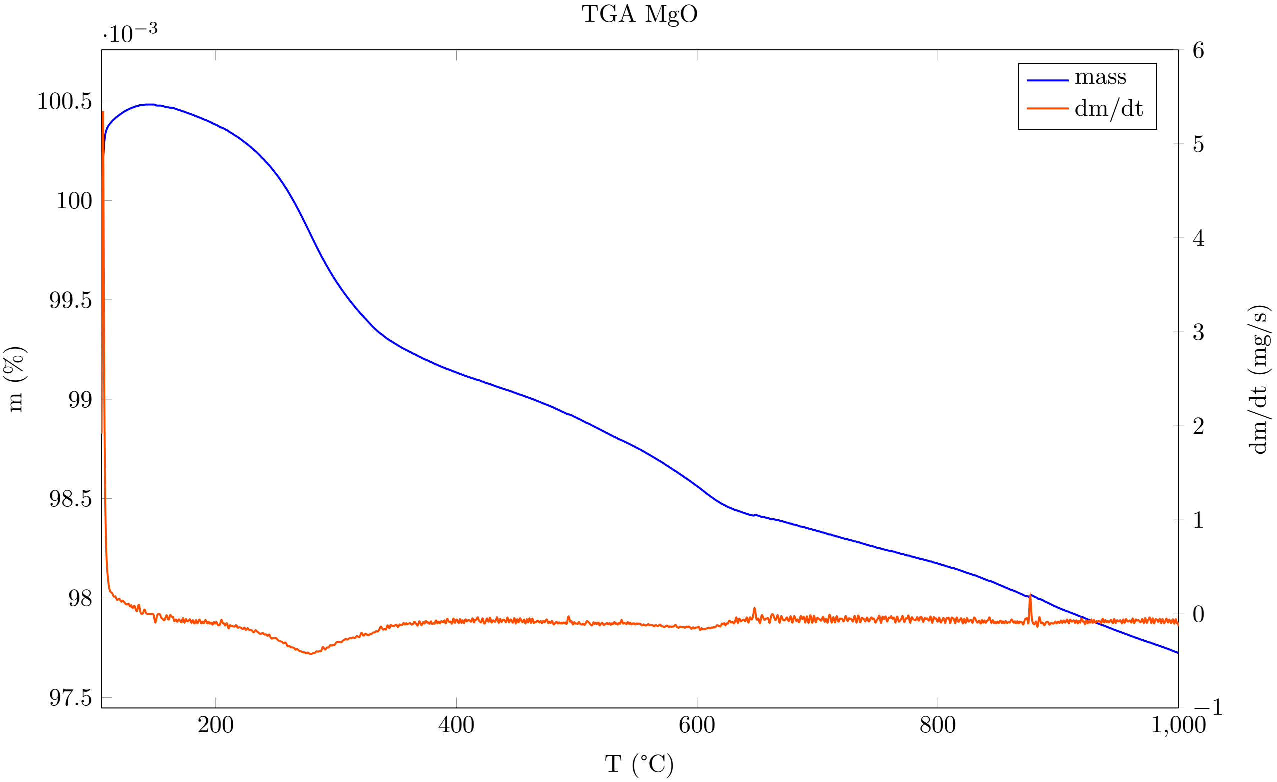

Figure 4.11: TGA curves of MgO

curve of the DTGA analysis, shown in fig.4.11, indicates a loss on ignition around 2.2% and the presence of brucite (loss of mass close to 300°C) and magnesite (loss around 600°C).
The loss of mass due to the decomposition of brucite ($Mg(OH)_2$) is due to the evaporation of water produced by the chemical reaction:

$$Mg(OH)_2 \ \rightarrow \ MgO \ + \ H_2O \tag{4.5}$$

To compute the amount of brucite one can retain the loss of mass between 200°C and 400°C, transform to number of moles of water and then transforming to mass of brucite by using the molar masses [51] [48]:

$$m_{brucite} = \frac{\Delta m}{u_{H_2O}} \cdot u_{Mg(OH)_2} = \frac{0.88\ g/100g}{18\ g/mol} \cdot 58.32\ g/mol = 2.8512\ g/100g \qquad (4.6)$$

4.3.3 X-ray crystallography

XRD have been done both on the anhydrous BFS both on the anhydrous binder (90% BFS + 10%MgO) and then, by subtracting the two diffractograms, we have obtained the one of the MgO reported in fig.4.12.

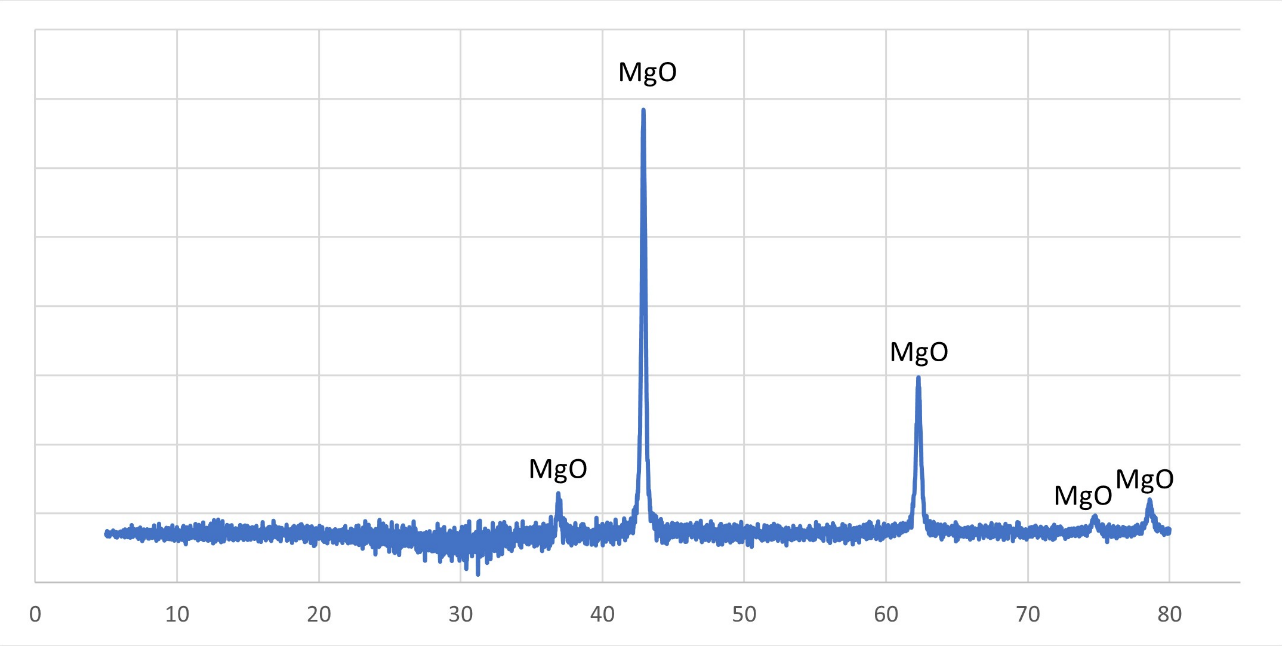

Figure 4.12: Diffractogram of MgO

The peaks of MgO are clearly visible (ordered with decreasing amplitude) at 42.9°, 62.3°, 78.6°, 74.7° and 36.9° [40]. Brucite and magnesite are not visible on the diffractogram, although their presence has been demonstrated via TGA, probably because of their very low amounts.

4.3.4 Pore structure and categorization of MgO

As many studies have shown the specific surface area (SSA) of an MgO-based product is directly related to its pore structure and the specific surface area in particular. The SSA is the surface area for a gram of product (cm^2/g) and reflects directly the manufacturing thermal treatment. The study of the pore structure have been done through a nitrogen adsorption test and the application of the Barret-Joyner-Alenda and the Brunauer-Emmett-Teller methods, as described in section 3.4.3.
The adsorption isotherm, shown in fig.4.13, is borderline between type I and type V because of the little hysteresis loop at the highest relative pressures: this means that some mesopores are

present together with micropores. The presence of both micropores and mesopores is confirmed by the cumulative pore volume curve and the pore size distribution.

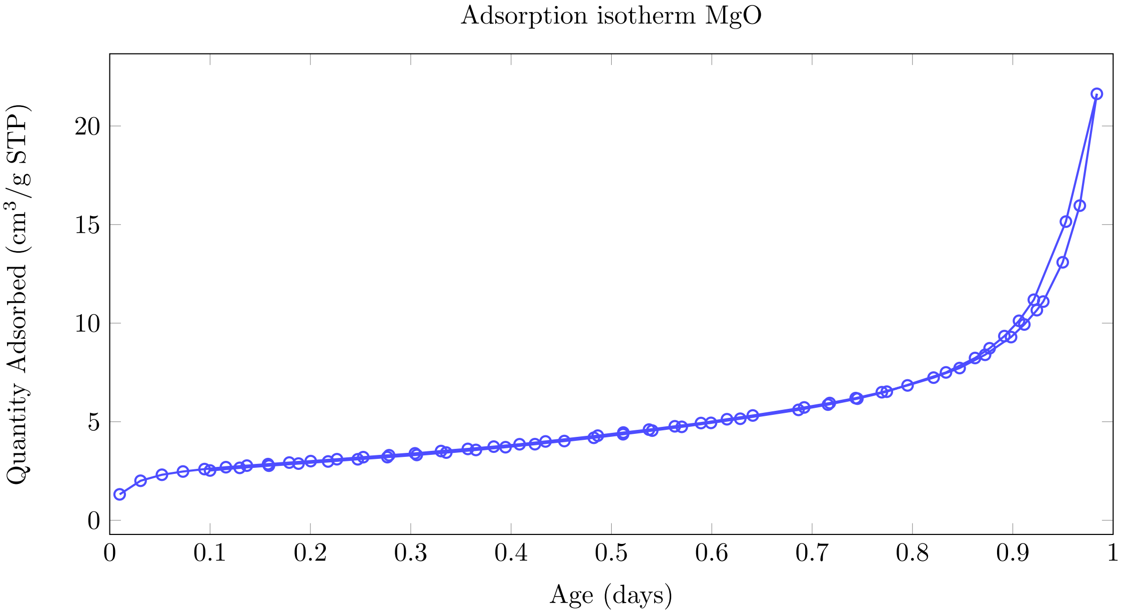

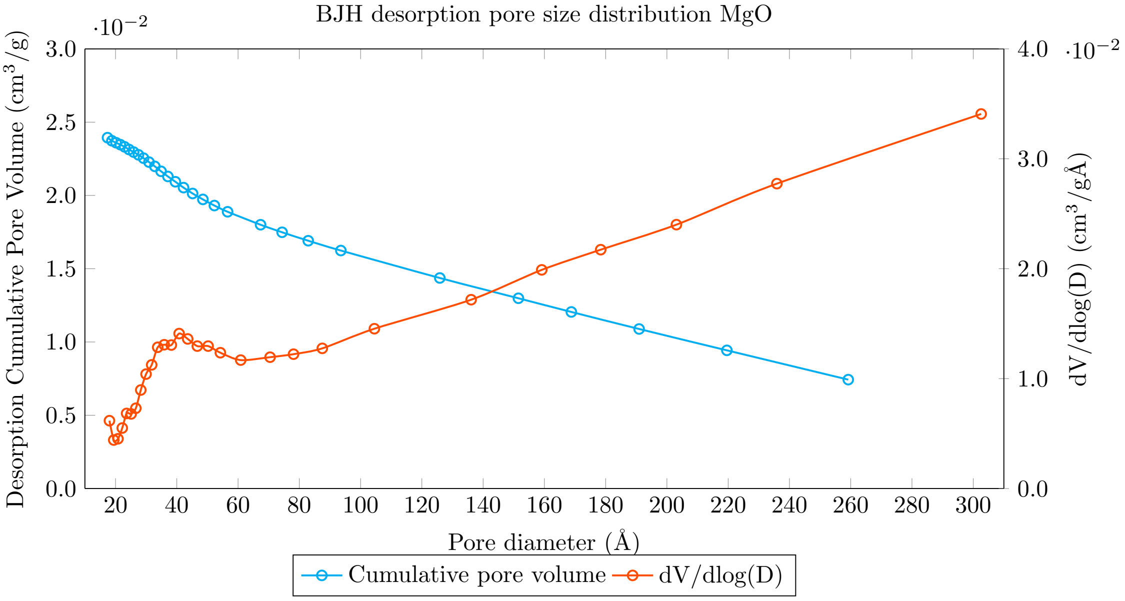

Figure 4.13: Adsorption isotherm and pore size distribution of MgO

The BET specific surface area is 10.7488 m^2/g.

In order to facilitate the application to alkali-activated cements (AAC) it is desirable to further categorize MgO products according to their reactivity, regardless of their sources and calcination process. Shand and Jin [10] have proposed to distinguish between 3 categories based on the value of SSA:

1. Category I: high reactivity $SSA > 60m^2/g$
2. Category II: medium reactivity $10m^2/g \leq SSA \leq 60m^2/g$

3. Category III: low reactivity $SSA < 10m^2/g$

According to this classification the used MgO product is a medium reactivity one.

4.3.5 Other measures of reactivity

Another test that can be done to estimate the reactivity of MgO is the *Chemical reactivity test*, which consists in adding MgO to an acid solution and measuring the time needed to neutralize it: the reactivity is higher as lower is the neutralization time.
The Chinese standard suggests a much simpler test which consists in hydrating a mass of MgO for 24h at room temperature, then in drying it at 100-110°C: the mass gain in percentage indicates the active MgO content.

4.3.6 Comparison between the methods to determine the reactivity

The SSA is a reliable and direct measure of the reactivity, so it can be taken as a reference to validate the other methods.
The LOI method is problematic because this parameter is not clearly related to the SSA so the estimation of the reactivity that it provides is not very reliable.
The chemical reactivity test is even more problematic because it does not make any significant difference between the reactivity of MgO with a SSA $<$ 10 cm^2/g.
As consequence it is suggested to use the nitrogen adsorption test to quantify the SSA and use this parameter as an indicator of the reactivity.

4.3.7 Study of reactivity via isothermal calorimetry

A rougher estimation of the reactivity can be done via an isothermal calorimetry, as described in section 3.5.1, followed by a DTGA on the hydrated powder. In figure 4.14 we can show that the peak of thermal power is reached very soon, after 1.62h, and the reaction ends around 40h after the contact with water. The following DTGA shown that the hydration rate is 83.25%.

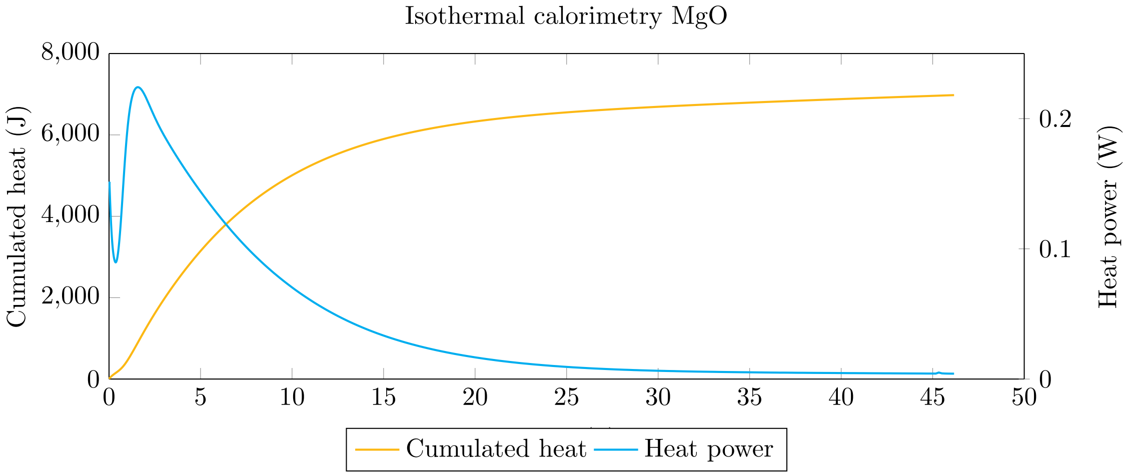

Figure 4.14: Isotherm calorimetry of MgO

4.4 CEMI

The used Portland cement is a CEMI 52.5N of the Galaxim line produced by Lafarge. The manufacturer proposes this line of products for self-compacting concrete so we expect its use to provide a good plasticity to the mortar composition. The value of the density provided by the manufacturer is 3.15 g/cm^3.

4.5 Conclusions

The characterization of precursors is a very important preliminary part of the experimental campaign because it allows to assess if relevant impurities are present and, studying the DTGA curves and the XRD patterns, to obtain more information that will be very important for the interpretation of the results.

The information provided by the manufacturer of GGBFS is coherent with our experimental observations: the XRD pattern is typical of a glass amorphous structure and the loss on ignition is 0.5 so we consider the information reliable. The chemical composition of the used GGBFS is quite similar to the one used by Burciaga-Díaz [17] in terms of specific surface area (SSA) and composition. One of the slags used by Burgiaca-Diaz has a SSA of 450 m^2/2 while ours has 420 m^2/g and the contents of SiO_2, Al_2O_3, CaO and MgO are very similar, so we expect to have similar results in terms of strength.

Contrary to the BFS the characteristics of the quicklime do not correspond to what is declared by the manufacturer: according to the technical information the product should contain more than 92% of CaO but actually an important quantity of portlantide and some calcite are present. The presence of these impurities is no unexpected because CaO is very reactive and can react with the water present in the air. Probably the product has not been stocked in the proper way. It will be interesting to use both calcinated quicklime and the untreated commercial product to see how the mix of CaO and $Ca(OH)_2$affects the activation and the hydration process of BFS.

About the MgO we can conclude that the information provided by the manufacturer are reliable because the quantity of brucite detected through a DTGA is less than 3% and the declared content of MgO 97%. Brucite peaks are not visible in the XRD patterns and the presence of carbonates is not visible in any of the performed tests. As consequence we can consider the product as pure and we will not perform any pretreatment as calcication. The DTGA performed on the hydrated powder after isothermal calorimetry shows that the same water to powder ratio applied on quicklime provides a hydration rate around 90% while it stops at 83% with MgO. MgO has a specific surface area that is about 10 times higher than quicklime and for this reason it is able to better trap the water in its pores and react. As consequence it means that MgO needs much more water to reach the chemical equilibrium.

Chapter 5

Experimental results

5.1 Mix design

The studies considered until now have used an activator to binder ratio of 10% [24][19][23], being the binder the sum of GGBFS and activator. When the activator is CaO the use of this ratio seems to maximize the mechanical strength [17]. The addition of CaO to a ternary blend Portland cement-slag-silica fume has negative effects [31].
Taking into account the reported experimental studies we have decided to prepare 5 very simple compositions of mortars having a activator/binder ratio constant 10%: only the nature of the activator or the mix of activators changes:

1. CaO dried 10%
2. CaO 10%
3. MgO 10%
4. CaO 5% + MgO 5%
5. MgO 5% + CEMI 5%

After the results of the slump and the mechanical tests we have decided to study two optimized versions of the compositions 2 and 5 by reducing the water to binder ratio in order to maximize the strength.
The first composition has been selected as the reference one. Its sand to binder ratio has been fixed at 2.5 and the water to binder ratio at 0.55. The selected water to binder ratio is the minimum capable of ensuring enough fluidity to compact the mortar in the molds without the use of any admixture. The characteristics of the compositions and the ratios of activator, water and sand are resumed in tab.5.1.

The mass of each component of the mix is calculated considering a volume of 1 m^3:

$$V_{BFS} + V_A + V_{Sand} + V_W = \frac{r_{BFS}}{\rho_{BFS}}\, m_B + \frac{r_A}{\rho_A}\, m_B + \frac{r_S}{\rho_S}\, m_B + \frac{r_W}{\rho_W}\, m_B = 1\ m^3 \tag{5.1}$$

Where r indicates the ratio on binder, ρ the density. For *binder* we mean the sum of GGBFS, activator and water that will form the hydrated paste.

Composition	CaO/b	MgO/b	CEMI/b	BFS/b	s/b	w/b
CaO dried 10%	0.10	0	0	0.9	2.5	0.55
CaO 10%	0.10	0	0	0.9	-	0.55
MgO 10%	0	0.10	0	0.9	-	0.55
CaO 5% + MgO 5%	0.05	0.05	0	0.9	-	0.55
MgO 5% + CEMI 5%	0	0.05	0.05	0.9	-	0.55
CaO 10% opt	0.10	0	0	0.9	-	0.45
MgO 5% + CEMI 5% opt	0	0.05	0.05	0.9	-	0.47

Table 5.1: Description of the studied compositions

From equation 5.1 we obtain the total quantity of binder:

$$m_B = \frac{1\ m^3}{\frac{r_{BFS}}{\rho_{BFS}} + \frac{r_A}{\rho_A} + \frac{r_S}{\rho_S} + \frac{r_W}{\rho_W}} \tag{5.2}$$

Once calculated the total mass of binder, the quantities of BFS, sand and activator are calculated multiplying them by the respective ratios. To calculate the mass of water we have to consider the quantity adsorbed by the sand, that has been dried in a oven at 105°C for at least 2 days, which corresponds to 0.8% of the mass of the sand:

$$m_W = \frac{r_W}{\rho_W}\ m_B + 0.008\ m_S \tag{5.3}$$

The sand content per 1 m^3 of the reference composition is 0.52 m^3/m^3 which will be adopted for the other compositions too, to have the same quantity of paste to compare the shrinkage measures.
The imposition of the volume of sand changes the equation, but all the other quantities are calculated in the same way as before.

$$m_B = \frac{(1 - 0.52)\ m^3}{\frac{r_{BFS}}{\rho_{BFS}} + \frac{r_A}{\rho_A} + \frac{r_W}{\rho_W}} \tag{5.4}$$

5.2 Fresh state behavior

For each composition the slumps have been measured through the Abram's cone test and the initial temperature with a thermometer. In the following paragraph we will describe in details the proportions of raw materials for each composition, the result of the slump measure and the initial temperature.
According to the results in table 5.2 and the results of the mechanical tests we have decided to reduce the water to binder ratio of compositions 2 and 5, to try to improve the mechanical strength.
As we can see in figures 5.1 and 5.2 and in table 5.2, the nature of the activator plays a very big influence on the fluidity and on the initial temperature. It is worth noting that the initial temperature of the composition CaO 10% decreases with the water to binder ratio because the reduction of the quantity of water makes the dissolution of quicklime more difficult.
It may seem that some segregation is present. To assess it we have tested the behavior for

different w/b ratios, adding controlled quantities of water to gradually increase it and repeating the slump test at each step. Based on that we can say that what looks like segregation is actually due to the inability of BFS to retain water and react with it as clinker does.

Composition	w/b	Slump [cm]	T [°C]
CaO dried 10%	0.55	2.4	31.2
CaO 10%	0.55	10.5	26.5
MgO 10%	0.55	2	19.2
CaO 5% + MgO 5%	0.55	7	22.5
MgO 5% + CEMI 5%	0.55	8	19
CaO 10 % opt	0.45	3.5	24
MgO 5 % + CEMI 5% opt	0.47	2	20

Table 5.2: Slump and initial temperatures of the compositions

(a) Slump composition CaO dried 10%

(b) Slump composition CaO 10%

(c) Slump composition MgO 10%

(d) Slump composition CaO 5% + MgO 5%

Figure 5.1: Slumps of compositions

(a) Slump composition MgO 5% + CEMI 5%

(b) Slump composition CaO 10% w/l reduced

(c) Slump composition MgO 5% + CEMI 5% w/b reduced

Figure 5.2: Slumps of compositions

5.3 Characterization of the microstructure

5.3.1 X-ray powder diffraction

The X-ray powder diffraction (XRD) allows us to characterize the hydration products by comparing the pattern of the hydrated binder with the ones of the single products.

XRD pattern of CaO compositions

The XRD pattern of CaO compositions are shown in fig.5.3 and fig.5.4. An important presence of $Ca(OH)_2$is generated by the hydration of the quicklime used as activator. The sharp CaO peaks present in the anhydrous binders almost disappear meaning that the hydration of quicklime has reached a very high degree, confirming that the used quicklimes are very reactive and the hydration reaction reaches very high degrees as remarked in section 4.2.5. Some carbonation is present as one can see from the peaks of calcite. In the uncalcinated quicklime composition part of the final amounts of portlandite and calcite derive from the anhydrous binder.

On the side of the products of the slag hydration we can see relevant C(A)SH peaks at 29.5 and 50°, and a little at 16° as indicated by [38]. C_4AH_X is visible presenting two twin peaks at 10.6 ad 11.4°, other twos at 22.1 and 22.9, and isolated peaks at 36.7 and 55.7°. Little peaks of akermanite are visible at 28, 31 and 51.9°. Hydrotalcite peaks are expected to appear at 5.5, 11.3 and 22.7° but the first peak is absent (not visible probably because the starting angle of the analysis is 5°) while the others are superimposed with calcite and C_4AH_X. Being hydrotalcite and C(A)SH the main products of slag hydration the presence of both is expected, so maybe the quantity of hydrotalcite in the hydrated paste is low.

The use of calcinated or uncalcinated quicklime makes no difference in the nature of the hydration products but only in the intensity of the peaks.

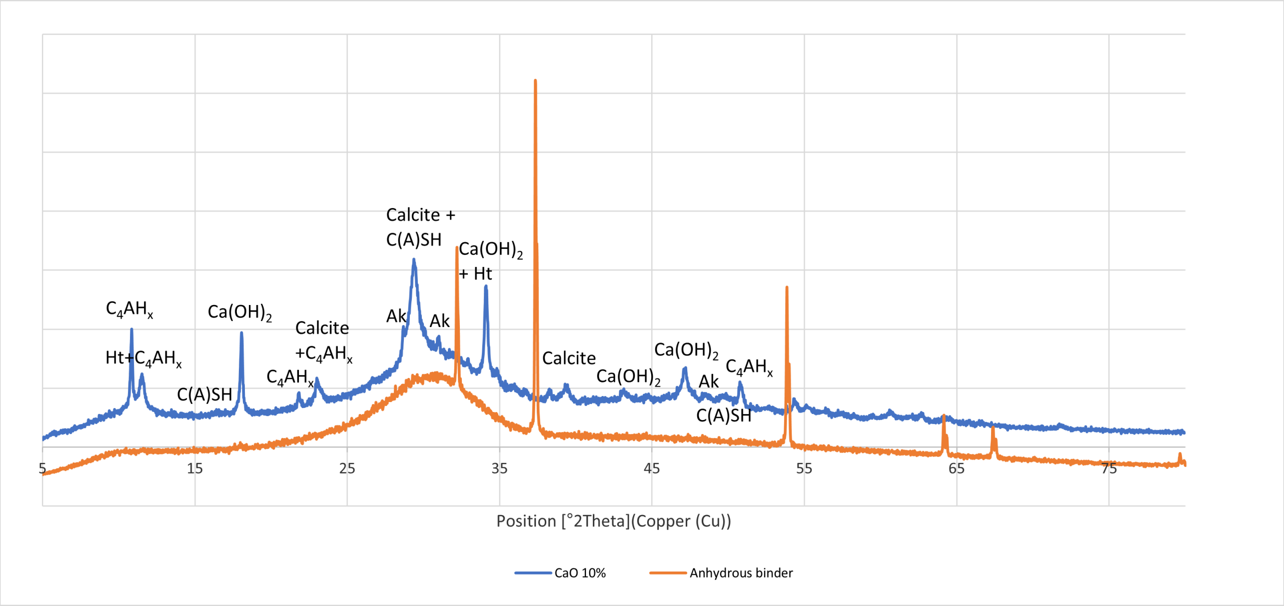

Figure 5.3: Diffractogram of CaOd 10%

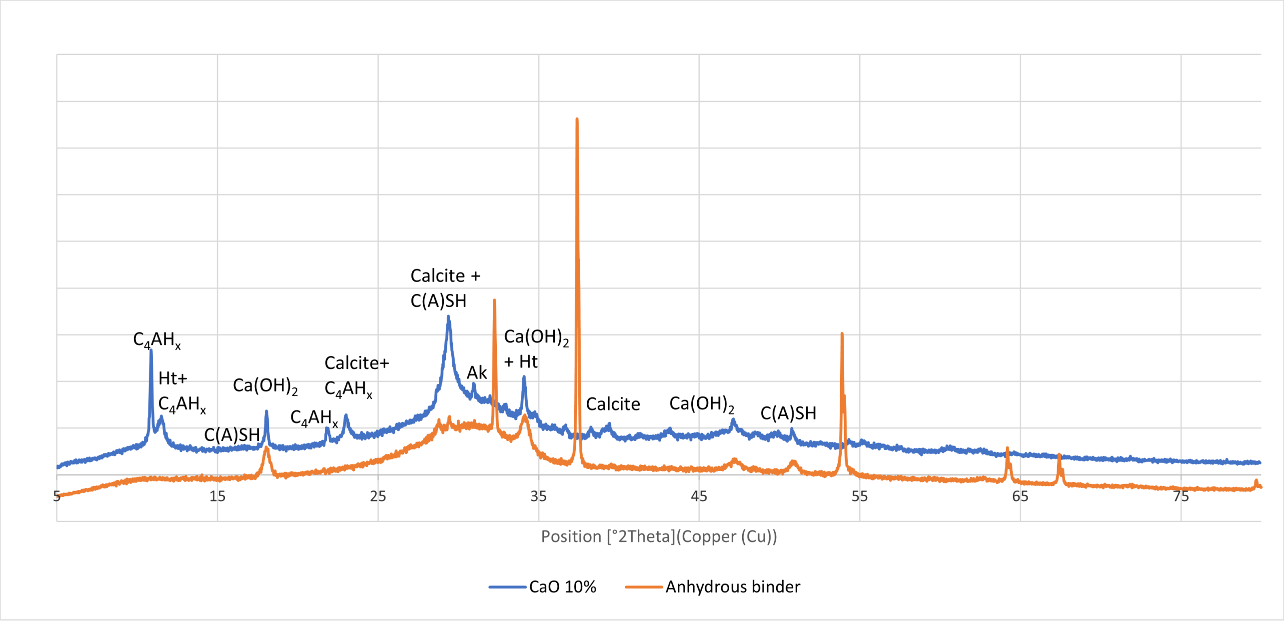

Figure 5.4: Diffractogram of CaO 10%

XRD patterns of MgO compositions

The XRD patterns in fig.5.5 and 5.6 show the presence of unreacted MgO. Important peaks of brucite are visible at 18.6, 37.2, 50.3 and 58.8°. Hydrotalcite peaks are visible at 11.3 and 22.7. Additive and inherent MgO can be consumed for the production of hydrotalcite or may depose as brucite according to the mechanism described in section 2.2. The important presence of brucite means that the consumption rate of MgO is not high enough to compensate the formation of brucite whose presence may be detrimental for the paste soundness.

C(A)SH and maybe MSH gel are visible at 29.5, 31.44 and 35.09° but they are not easy to distinguish.

Some carbonation is present as the peaks of calcite suggest.

The mix between MgO and CEMI leads to the formation of $Ca(OH)_2$as hydration product of clinker and to the presence of probably C_3S deriving from the unreacted binder. The only other difference between the XRD patterns of MgO 10% and MgO 5% + CEMI 5% is the lower presence of unreacted MgO in the latter case.

Using uncalcinated quicklime instead of CEMI leads to the simultaneous presence of the hydration products of both MgO 10% and CaO%, but both unreacted CaO and MgO peaks are visible.

5.3.2 Thermogravimetric analysis

The DTGA analysis has been used to evaluate the development of the hydration process and the carbonation. The analysis takes into account the temperature starting from 105°C to drop the loss of mass due to the evaporation of free water.

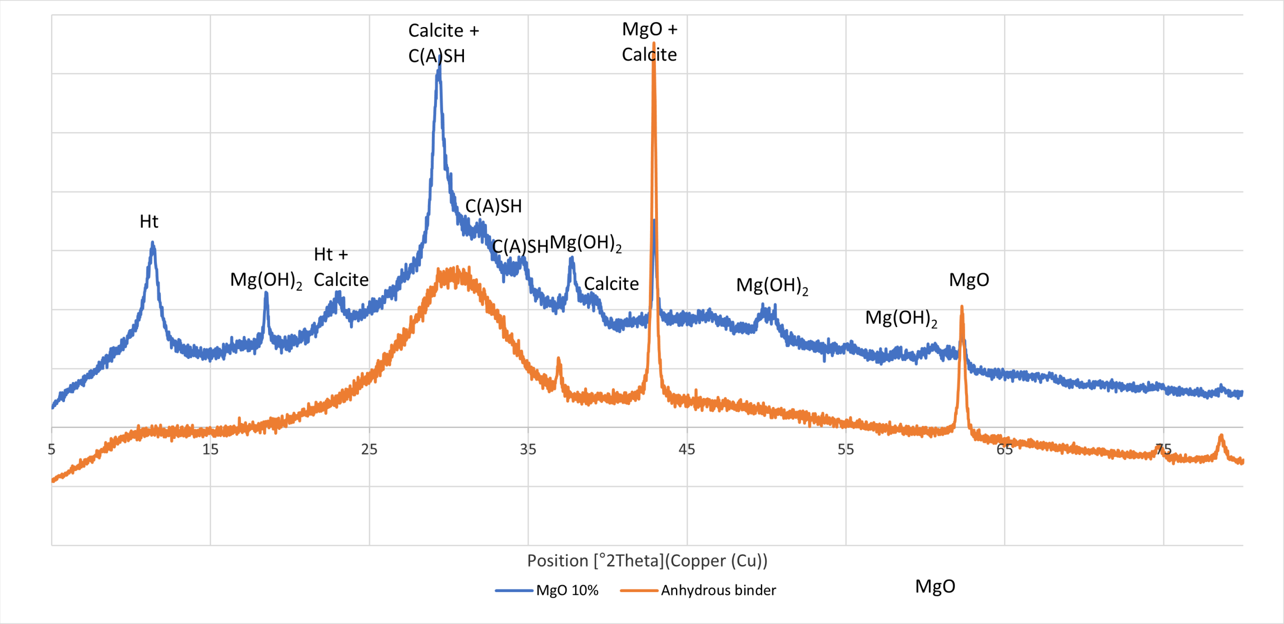

(a) Diffractogram of MgO 10%

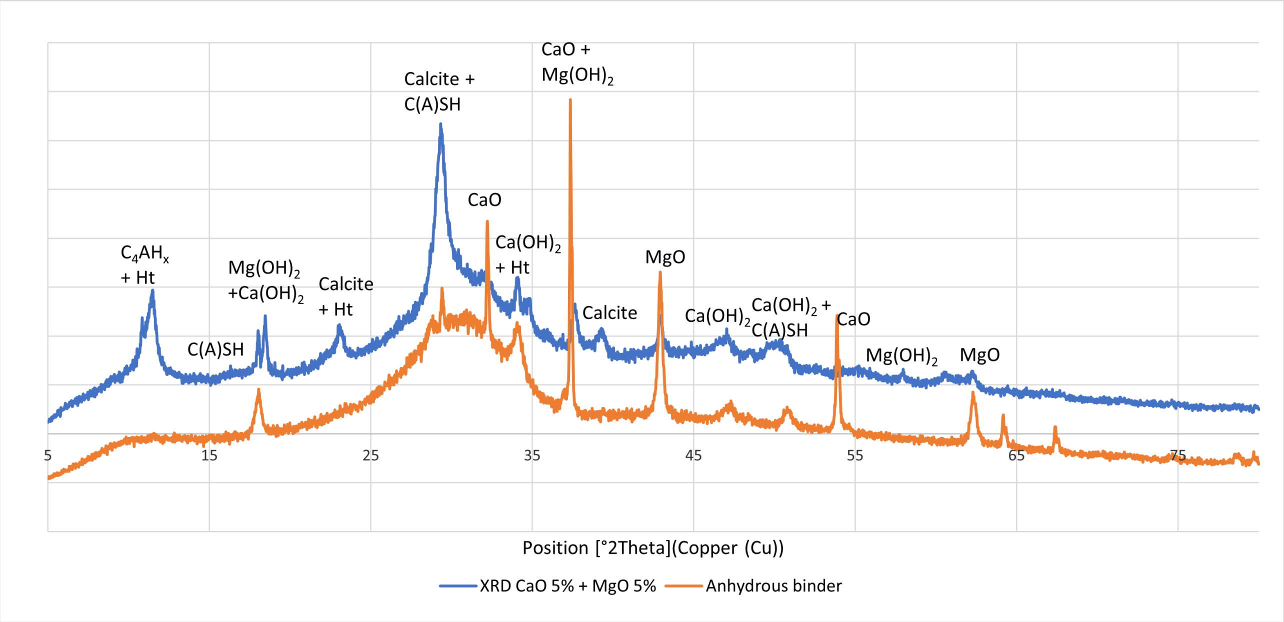

(b) Diffractogram of MgO 5% + CaO 5%

Figure 5.5: Diffractograms of MgO and MgO+CaO compositions

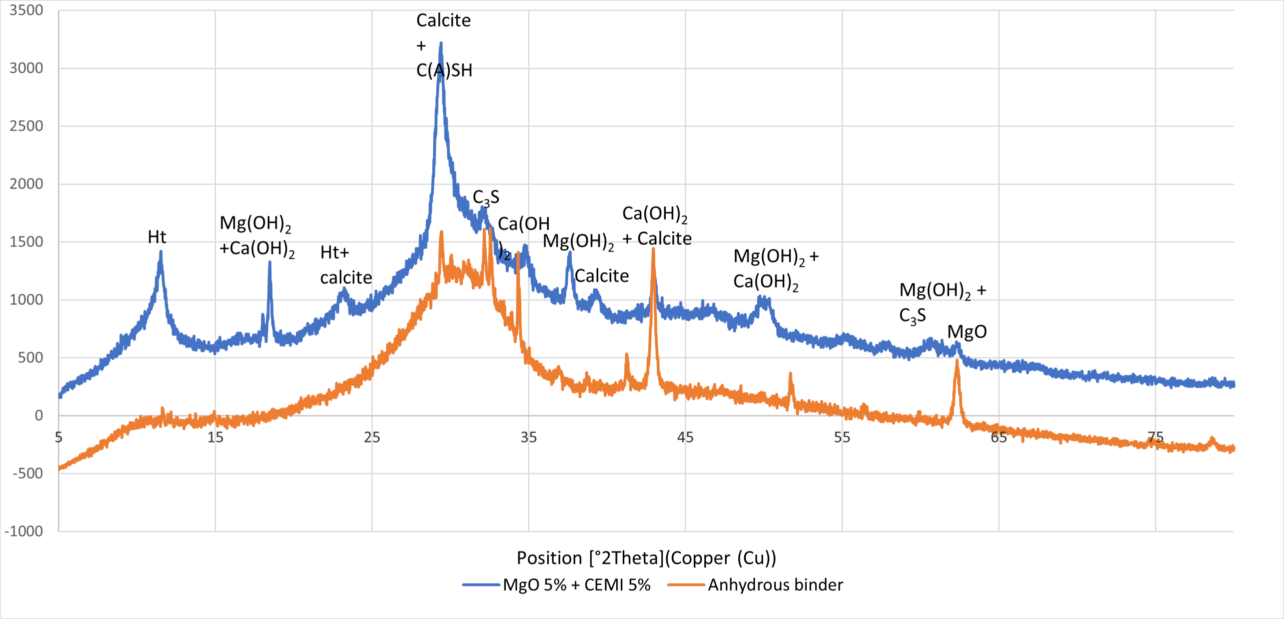

Figure 5.6: Diffractogram of MgO 5% + CEMI 5%

CaO compositions

The compositions that uses CaO as activator show that most part of the hydration products decompose in the temperature ranges 105-300 and 105-600°C in the first 28 days of curing; the growth continues slower until 90 days.

The total mass loss of CaOd 10% monotonically increases while the one of CaO 10% presents a minimum at 28 days, probably due to curing conditions or excessive delay in demolding.

The range 105-300 sums the decomposition of C(A)SH and hydrotalcite (ettringite has not been detected from XRD patterns) and the growth of the absolute value of the mass derivative in this range confirms that this products keep forming after 28 days albeit at slower rate.

The temperature range 105-600°C represents the decomposition of all hydrates and it is strongly affected by the presence of $Ca(OH)_2$. Sharp peaks of portlandite in dm/dt curves are visible between 400 and 500°C and their intensities tend to be maximum during the first 28 days and then to decrease until 90 days, probably because of the pozzolanic activity of BFS. Globally the total amount of hydrates is similar in both the CaO-based compositions.

The presence of carbonates is visible in the temperature range 600-1000°C and, as well as the presence of hydrates, the carbonation takes place mostly during the first 28 days and then slows down until later age. The use of impure CaO seems to produce a paste that is a bit less sensitive to carbonation but at the same time introduces an initial quantity oc $CaCO_3$ that fortunately is inert. This can be justified by the fact that the mass loss in the range 600-1000°C growths more slowly in CaO 10% that CaOd 10% during the first 28 days.

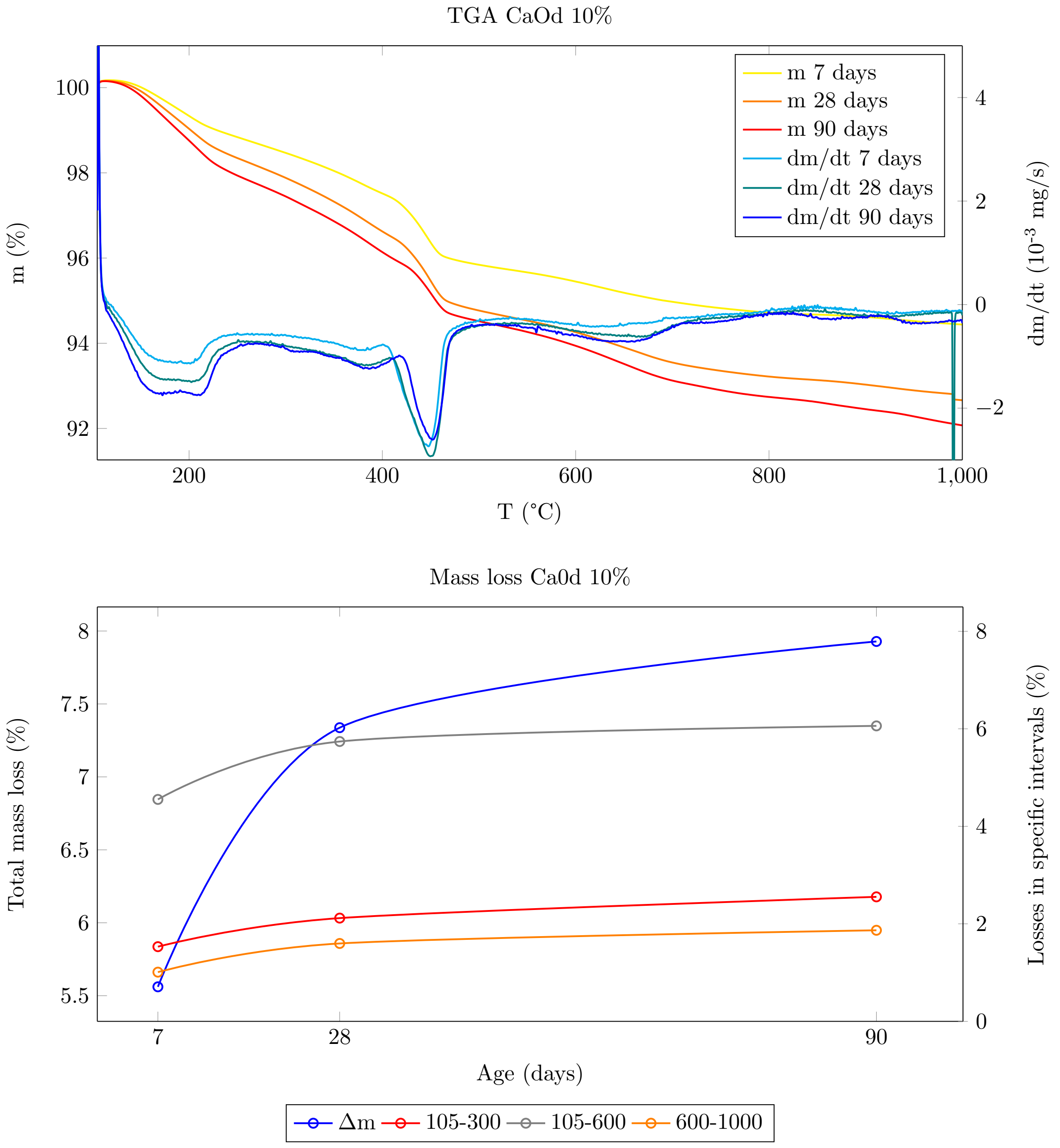

Figure 5.7: TGA of CaOd 10%

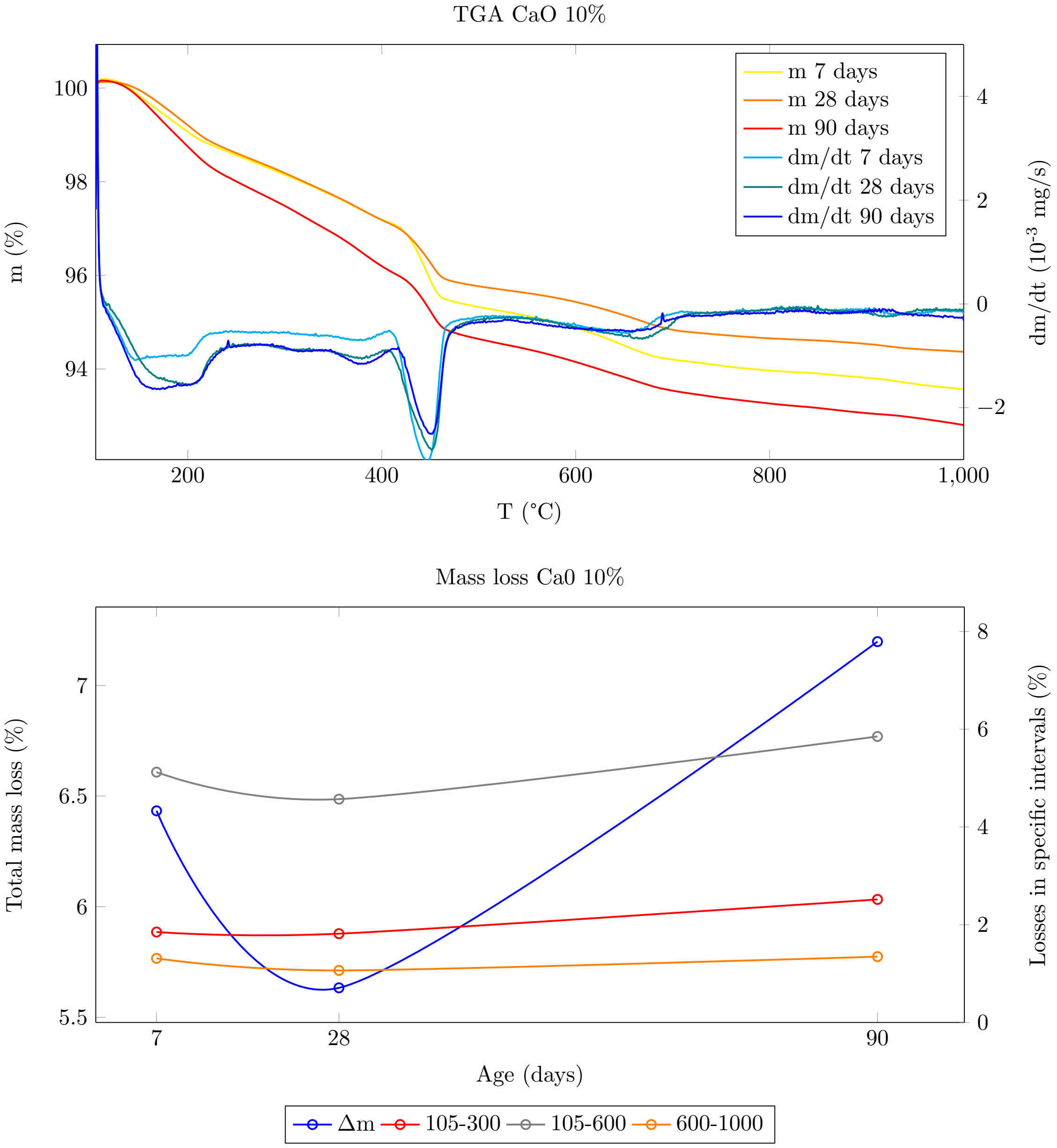

Figure 5.8: TGA of CaO 10%

MgO 10%

The total mass loss of this composition monotonically increases until 90 days, meaning that reaction products keep forming. Most of the products form in the first 28 days.
The mass losses in the ranges 105-300 and 105-600 growth in the first 28 days because of the formation of hydrates then decrease. From the DTGA curves in fig.5.9 one can see that brucite is present in important quantities and most of it forms after the first 28 days.

The mass loss due carbonation remains almost constant during the first 28 days, as one should expect knowing the pore-filling properties of brucite, but almost doubles between 28 and 90 days. We can conclude that the increment in the total mass loss is due to both carbonation and formation of brucite which are relevant. Due to the fact that the quantity of brucite increases we can observe that carbonation hits C(A)SH and hydrotalcite the most because of

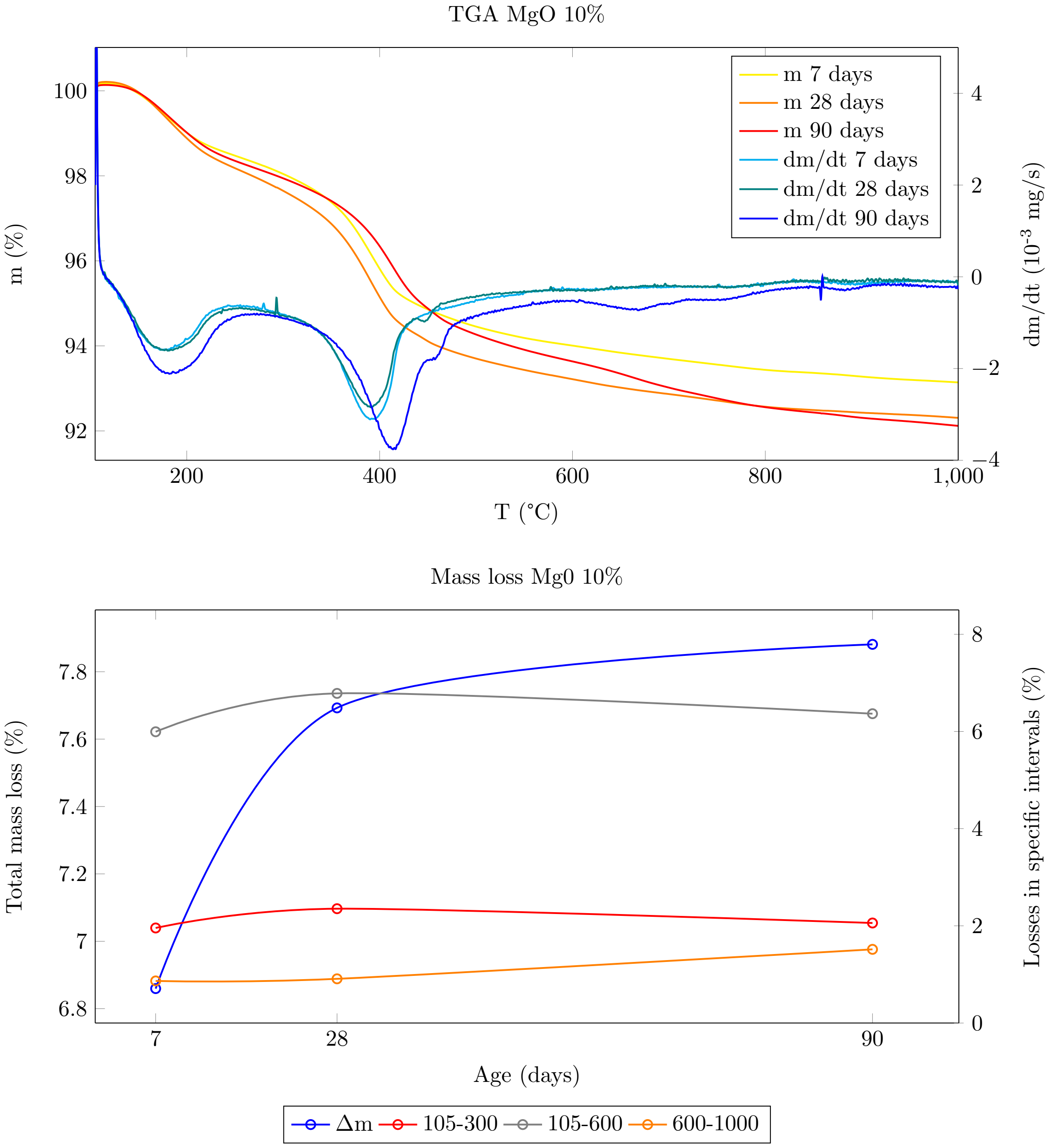

Figure 5.9: TGA of MgO 10%

the reduction of the 105-300°C loss.
As previously said (section 2.2) when the precipitation of brucite is excessive because of the low consumption rate of the formation of hydrotalcite the paste may become instable and cracks may form. The important carbonation together with the reduction of the quantity of C(A)SH and hydrotalcite suggests that this phenomenon may have happened.

CaO 5% + MgO 5%

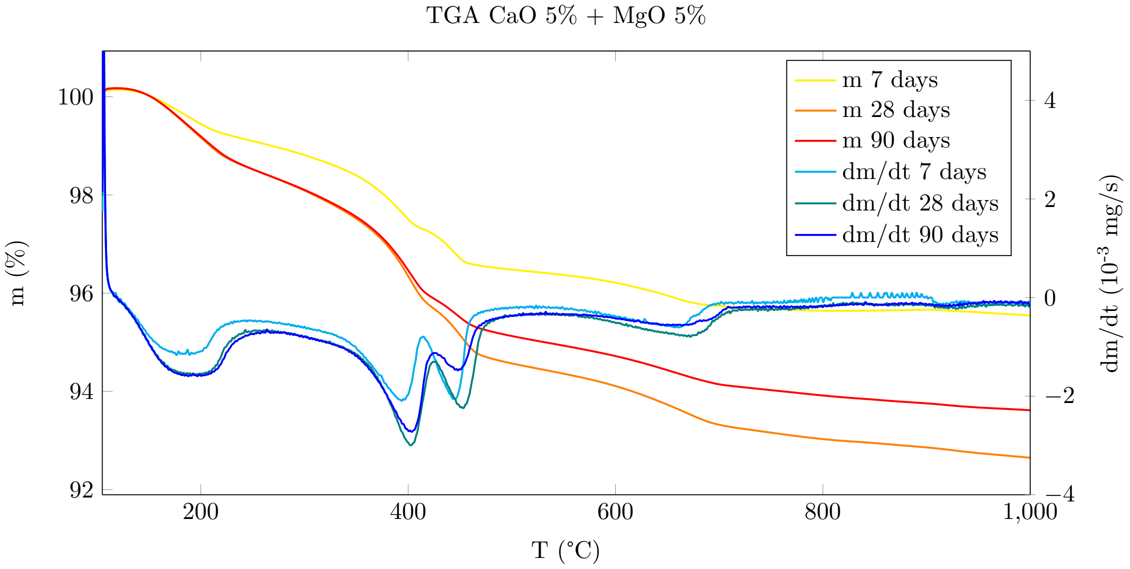

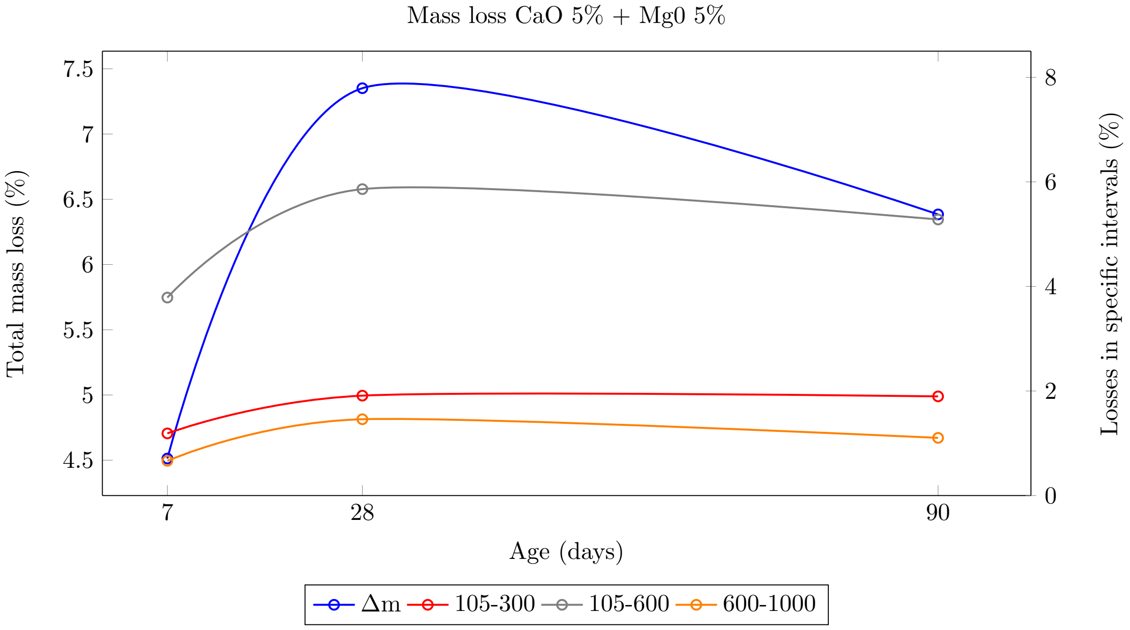

Figure 5.10: TGA of CaO 5% + MgO 5%

The total mass loss in fig.5.10 presents a decreasing behavior after 28 days of curing that can be caused by a change in the curing conditions or an excessive delay in the demolding. This issue makes difficult to observe the progress of the formation of hydrates and carbonates in the time range between 28 and 90 days.

The mass curves at age 28 days and 90 days are almost coincident for temperatures up to 400°C so the quantities of C(A)SH and hydrotalcite are the same. Considering the issue of the decreasing total mass loss and the fact that the 105-300 mass loss is constant between 28 and 90 days we can infer that the quantities of those products should increase in time.
Peaks of brucite and portlandite are visible between 400 and 500°C. Most part of these products form in the first 28 days and their quantity seems decreasing because of the total mass loss issue. In practice the quantity of portlandite is expected to decrease a bit because of the pozzolanic reaction with BFS while the quantity of brucite is expected to be constant.
Carbonation is present ass well and mostly develops during the first month. After 28 days the precipitation of brucite is expected to fill the pores improving the resistance to carbonation.

CEMI 5% + MgO 5%

The total mass loss presents a decreasing behavior after 28 days of curing that can be caused by a change in the curing conditions or an excessive delay in the demolding. This issue makes difficult to observe the progress of the formation of hydrates and carbonates in the time range between 28 and 90 days.
The mass losses associated to the decomposition of hydrates show an increasing behavior until 28 days and then they decreases with the total mass loss. The 600-1000 mass loss on the contrary decreases in the first 28 days and then remains constant. We can conclude that carbonation does not spread too much during the first month but after that it tends to progress.

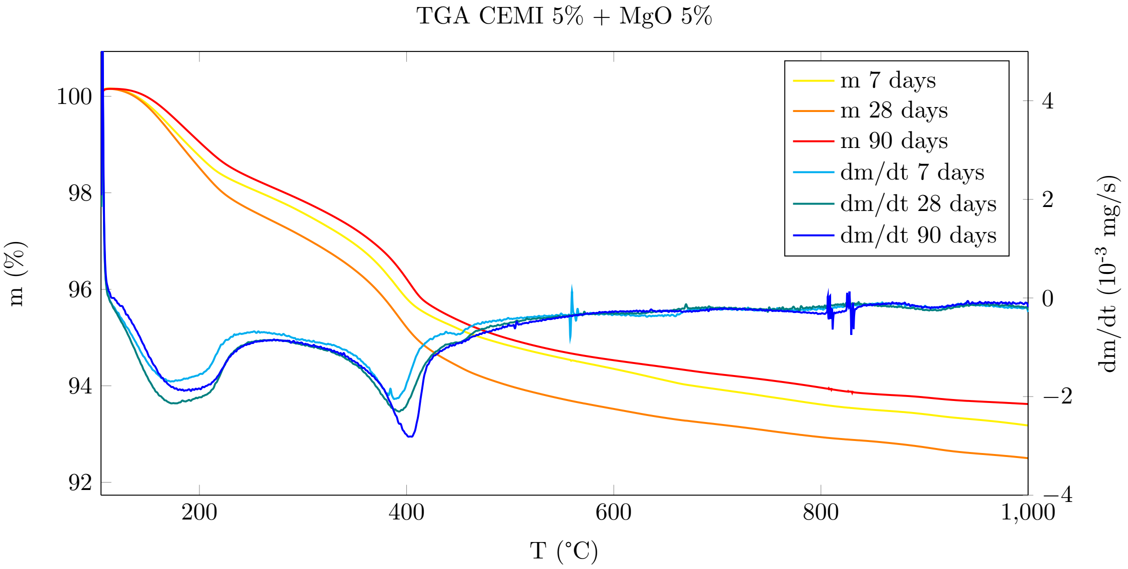

Figure 5.11: DTGA curve of CEMI 5% + MgO 5%

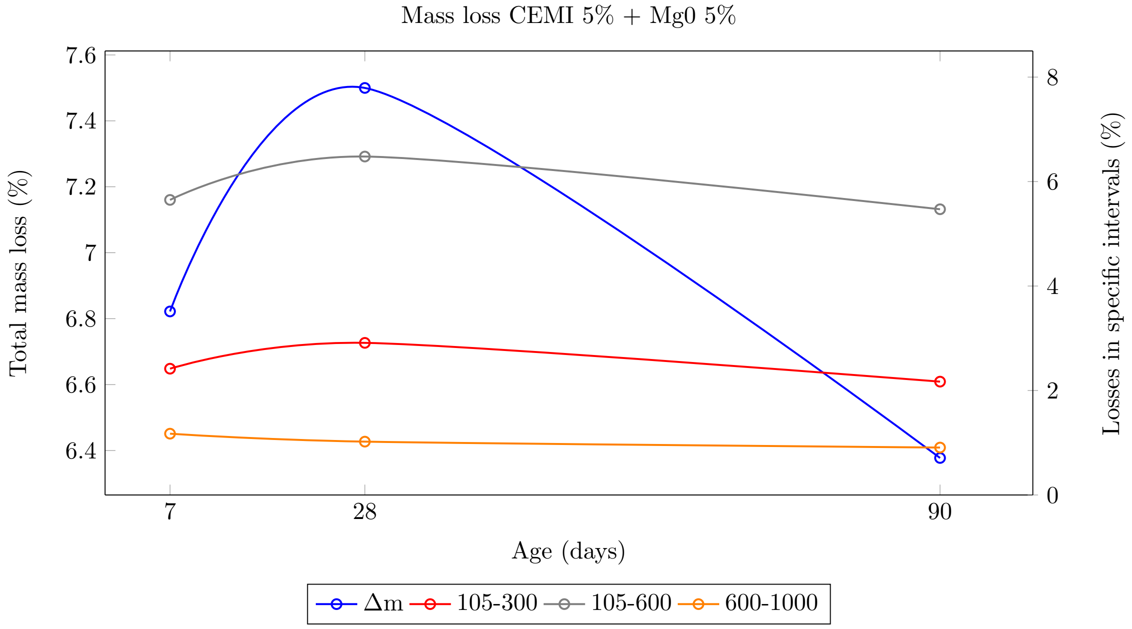

Figure 5.12: Mass loss of CEMI 5% + MgO 5%

5.3.3 Nitrogen adsorption analysis

As explained in section 3.4.3 the adopted drying method is quite aggressive and the results of this test are not very reliable as base to follow the development of the hydration process. Nitrogen adsorption allows to have some information on the porosity of C(A)SH and to estimate the average size of the pores. The results are resumed in table 5.3.

Composition	7 days	28 days	90 days
CaOd10%	39	35.12	34.55
CaO10%	36.71	35.37	38.81
MgO10%	34.96	37.23	37.22
CaO5%+MgO5%	33.52	36.82	35.62
CEMI5%+MgO5%	32.06	38.76	36.31

Table 5.3: Average C(A)SH pore diameter

CaO compositions

CaOd 10% has a cumulative pore volume curve minimum at 7 days, maximum at 28 and after 90 days it is comprised between the two others. The logarithmic derivative of the pore volume shows that the structure is quite regular after 7 days of curing, a prevalence of the pores larger than 100Å at 28 days. The dV/dlog(D) curve at 90 days shows a pore filling tendency, due to the fact that the peak of the curve has moved from 240Å to 120, excluding the spire at 35-40Å. The gel-pores range extends to 100Å superimposing with the range of capillary pores that starts at 25Å. In the pore size range 0-100Å the the dV/dlog(D) curve at 90 days is clearly higher than the others and this can be expected because of the hydration reaction, but the curve at 28 days is the lowest. The higher porosity at 28 days is thus a consequence of the prevalence of pores larger than 100Å which are not related to C(A)SH gel. The average pore diameter of C(A)SH, indicated by the position of the spire, reduced as the curing age increases from 39Å to 34.55Å.

The pore distribution of CaO 10% seems to be more regular because, except for dV/dlog(D) at 7 days, the curves at 28 and 90 days tend to flatten for diameter higher than 80Å. Furthermore as the curing age increases the pore size distribution curve tends to flatten. The spires indicating the average pore sizes of C(A)SH occur at 36.71, 35.37 and 38.81Å at respectively 7, 28 and 90 days of curing. Differently from CaOd 10% the tendency of average pore size to reduce is not evident in CaO 10%.

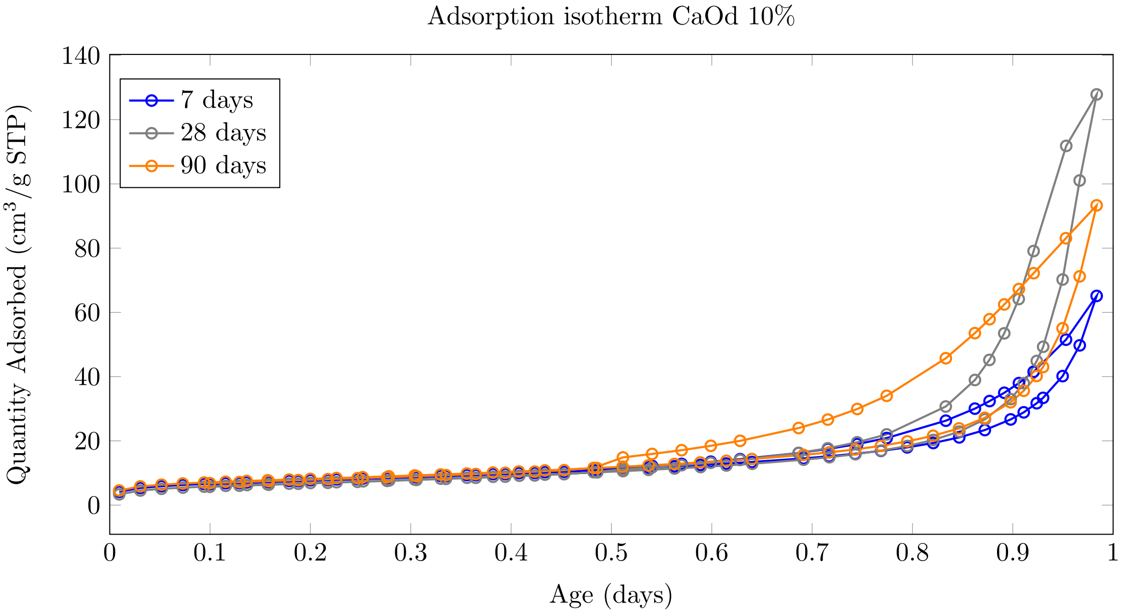

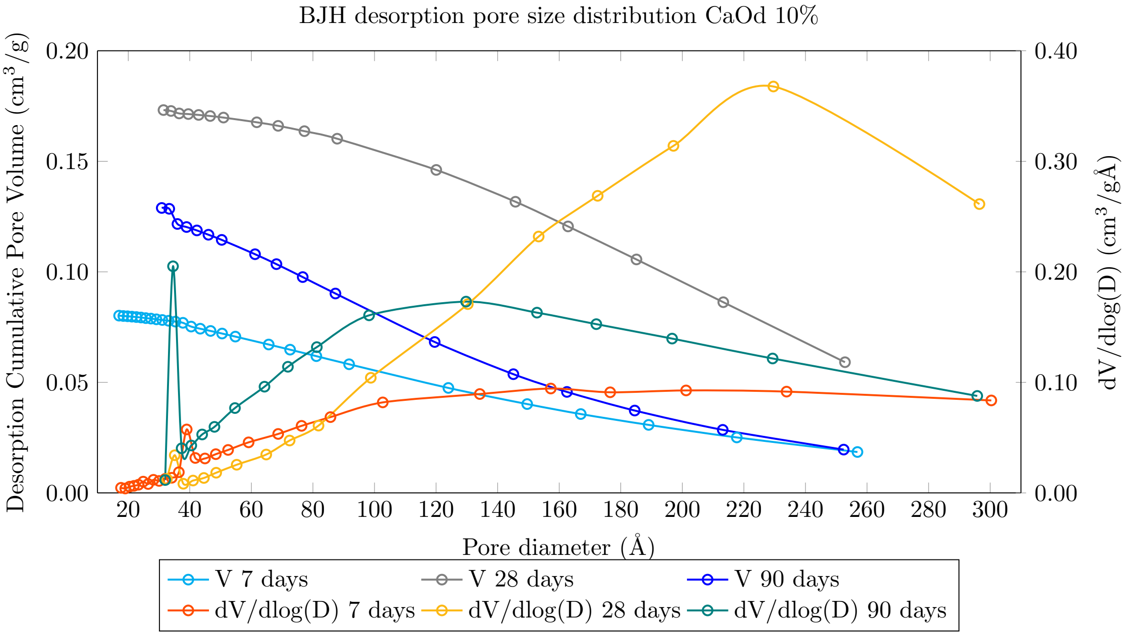

Figure 5.13: Nitrogen adsorption of composition CaOd 10%

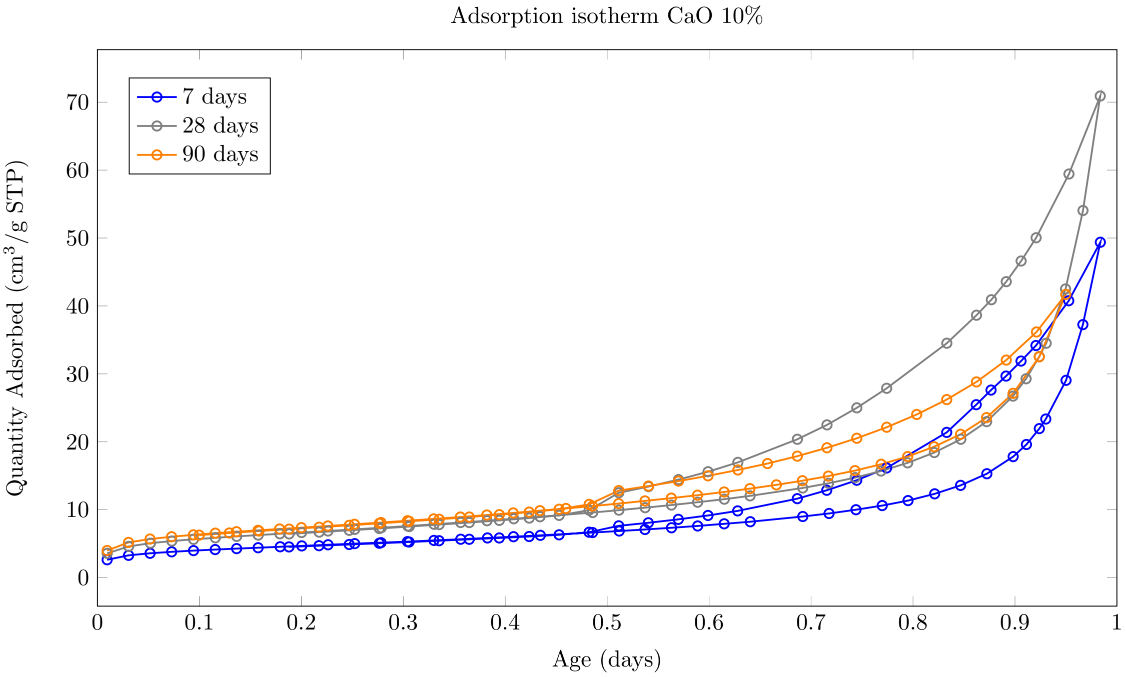

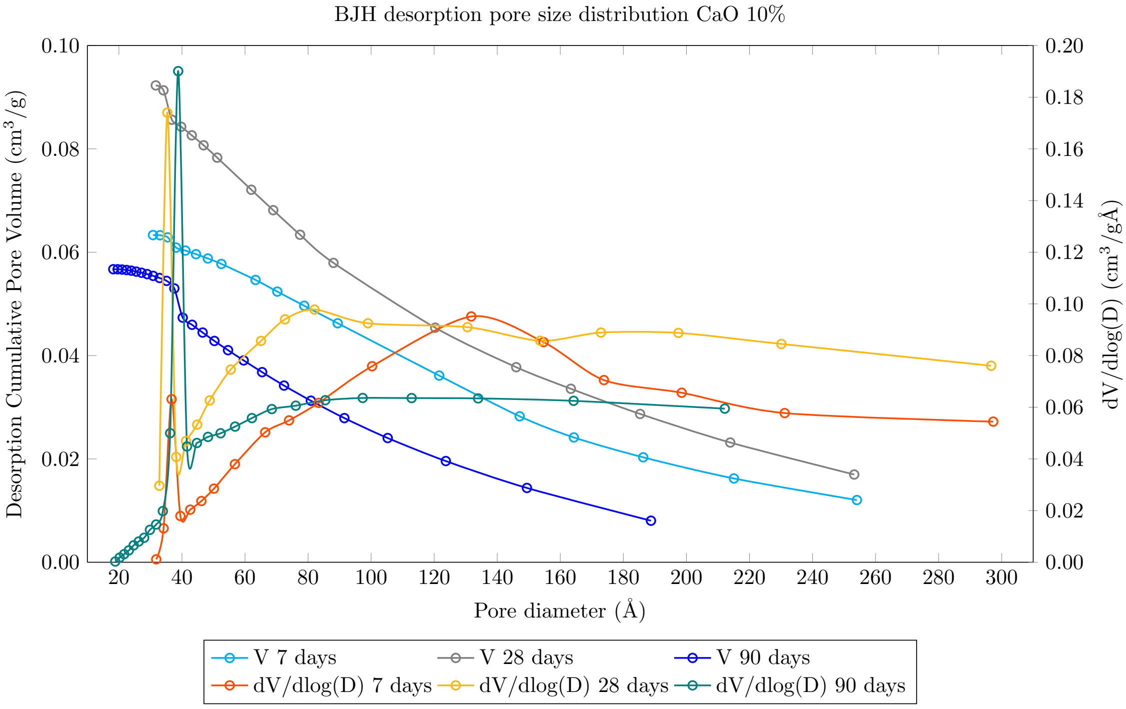

Figure 5.14: Nitrogen adsorption of composition CaO 10%

MgO compositions

The pore size distribution of MgO 10% composition, shown in fig.5.16, is more similar to the curves obtained by Bajja [36] for ordinary Portland cement and silica fume mixes. The spire is also the peak of the pore size distribution which tends to flatten after 40Å at any curing age. At 7 days there is a secondary peak at 80Å but this can be expected because the pore filling effects of C(A)SH formation and brucite precipitation is not evident yet. The initial average pore diameter is 34.96Å at 7 days which stabilized around 37.22Å after 28 days of curing. It is worth noting that the cumulative pore volume is lowest among all the compositions. This parameter should be considered carefully because it depends on the initial w/b ratio and the curing conditions but it suggests that MgO 10% has a much less porous paste than the other compositions.

The mix of CaO and MgO does not change the behavior of the pore size distribution curves shown in fig.5.17 but does not have increasing or increasing tendencies of the average C(A)SH pore size which is 33.52Å at 7 days, 36.82 at 28 days and 35.62 at 90 days of curing.

Using cement instead of lime leads to a disappearance of the flattening behavior of the dV/dlog(D) curves, with the exception of the 28 days one as we can see in fig.5.18. Higher gel pores and capillary pores beyond the gel pore range are more present. The average gel pore size is 32.06, 38.76 and 36.31 respectively for the three curing ages.

BET specific surface area

The calculation of BET surface area leads to results that do no suggest any interpretative path, except that MgO 10% has the lowest surface area at any studied age while CaO 5% + MgO 5% has the highest values which remain approximately constant.

The weakness of the gas adsorption method resides in the access of gas to the littlest gel pores that may be reduced by inappropriate drying techniques. Furthermore it seems that the type of calcium silicate hydrates (CSH) has a strong contribution on the capacity of the gas to penetrate in the pores because low-density CSH is the only one totally or partially accessible to nitrogen [36]. For these reasons the calculated BET surface area does not represent the totality of the gel pores but only the portion accessible to nitrogen. To improve the results and their interpretation it would be very useful to characterize the formed CSH by means as the SEM or an adsorption test of steam water, which is able to penetrate better inside the pores.

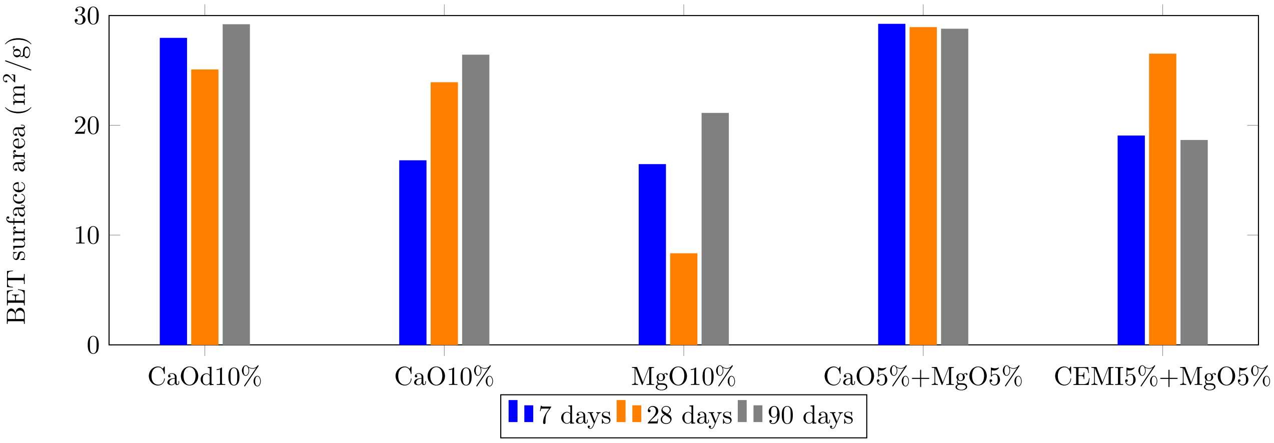

Figure 5.15: BET surface area of the studied compositions

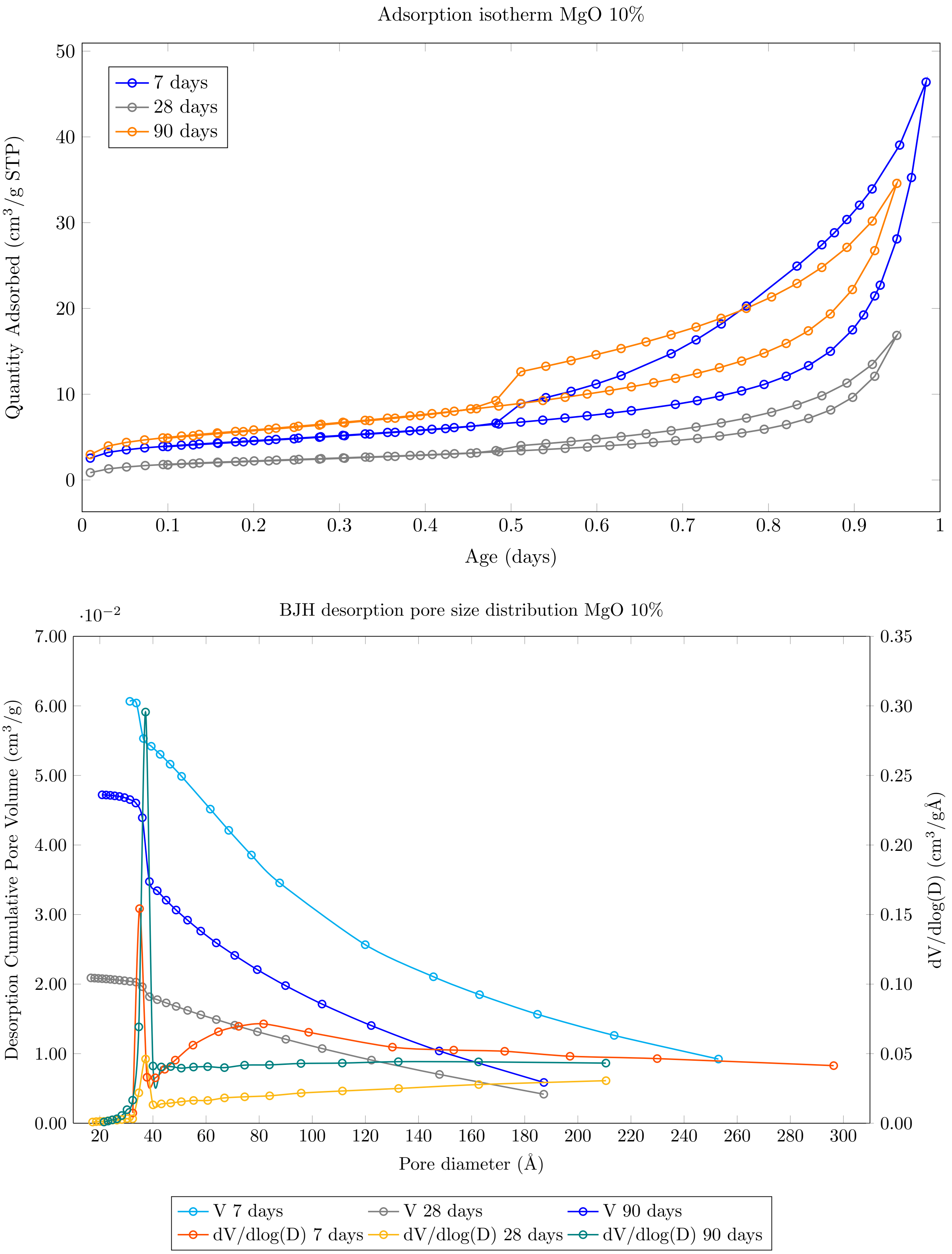

Figure 5.16: Nitrogen adsorption of composition MgO 10%

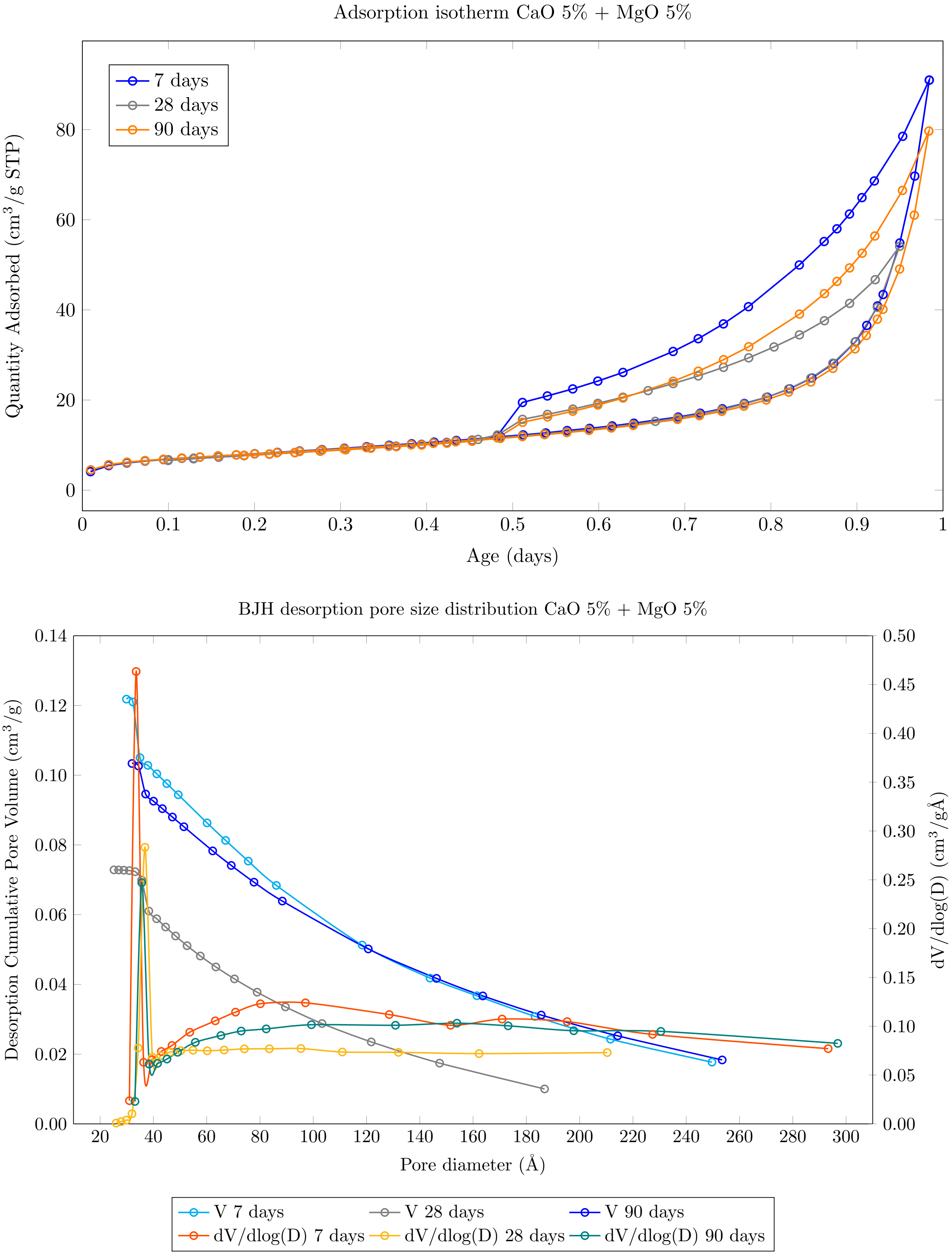

Figure 5.17: Nitrogen adsorption of composition CaO 5% + MgO 5%

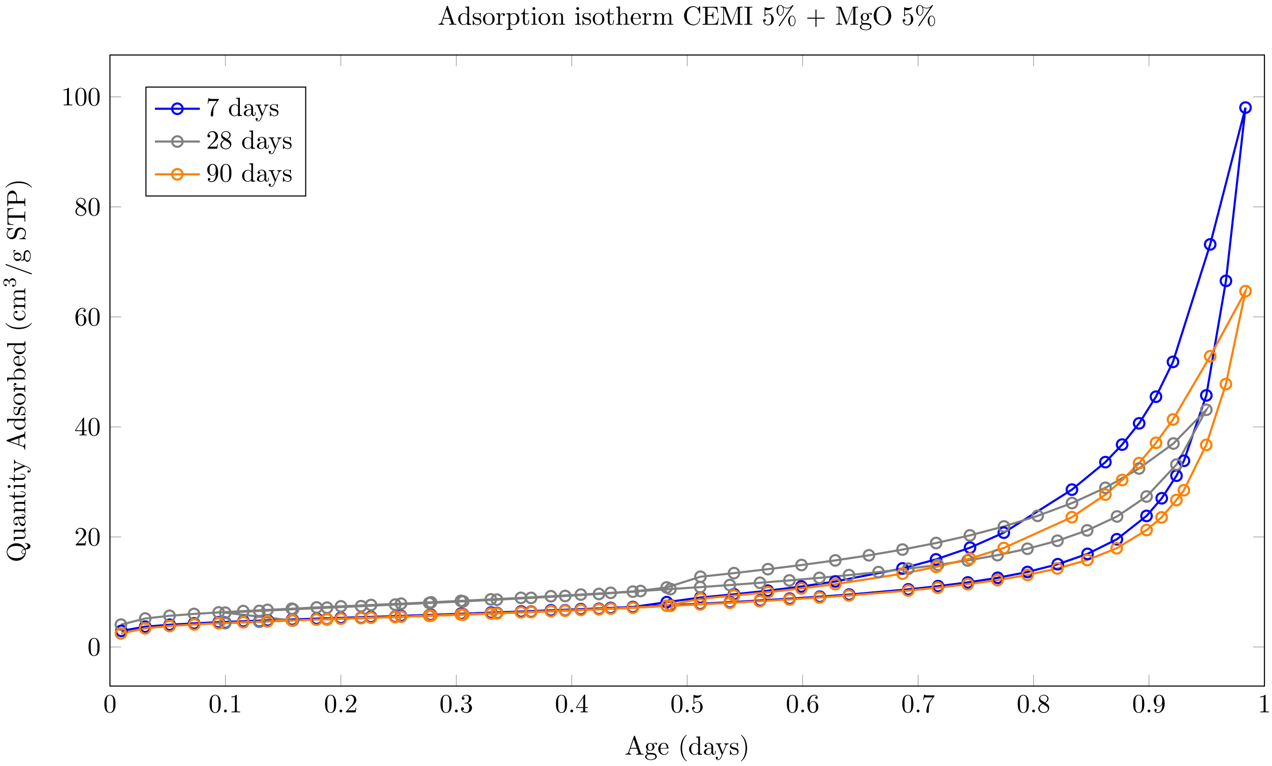

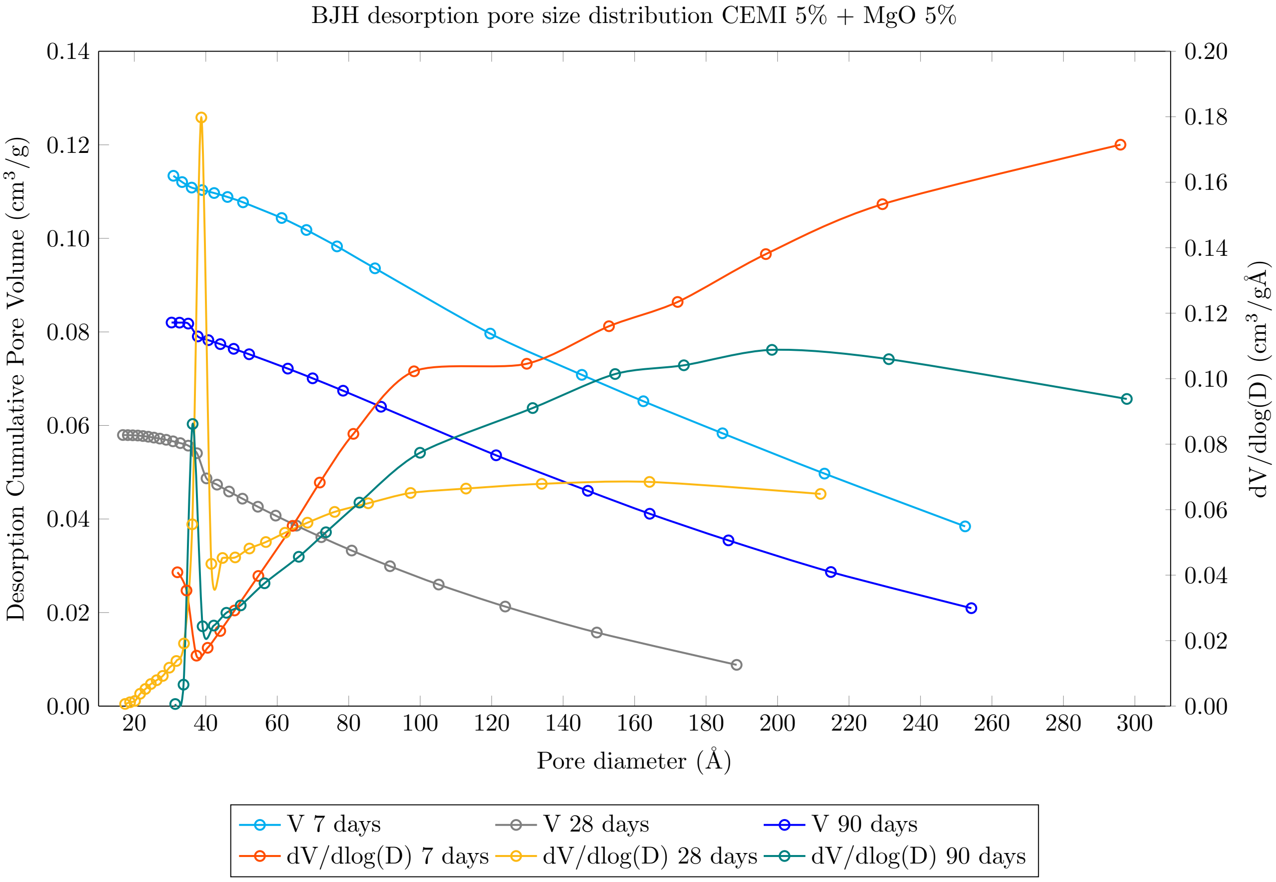

Figure 5.18: Nitrogen adsorption of composition CEMI 5% + MgO 5%

5.3.4 Water porosity test

Water porosity test is suitable to study accessible pores larger than about 400Å, which have effects on strength and permeability of the cement paste. As one should expect the formation of brucite consequent to the hydration of additive MgO reduces the porosity, which is minimum in MgO 10%, except when MgO is used as activator together with CaO because this combination gives the highest accessible porosity. The mix of different activators has the consequence of increasing the relative density which is maximum in CaO 5% + MgO 5% and CEMI 5% + MgO 5% while it is minimum in CaO 10%.

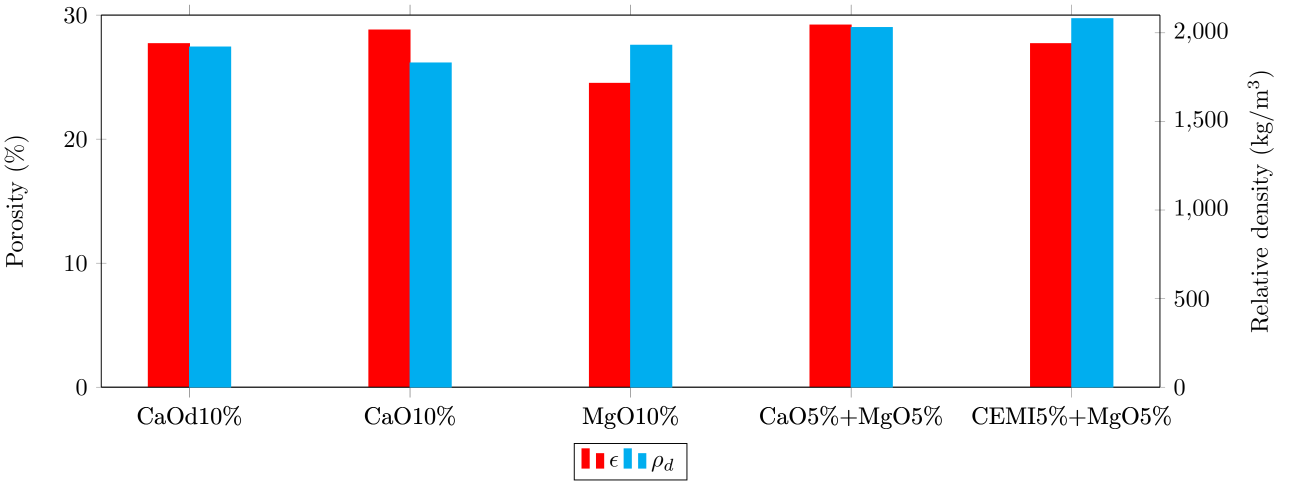

Figure 5.19: Accessible porosity and relative density

5.3.5 Conclusions

The study of the microstructure has shown that the use of MgO produces important quantities of brucite while the use of quicklime produces important quantities of portlandite. The presence of portlandite is a well expected fact but the presence of brucite is not for granted because it depends on the difference between the reactivity of the MgO and the BFS. The presence of brucite means that the BFS used in this study is little reactive compared to the MgO.
Brucite is employed to compensate the shrinkage and to reduce porosity exploiting its expansive effects[39], but at the same time its presence may be detrimental to the paste soundness. The pore filling effect of brucite is evident because MgO 10% is the composition having the lowest porosity, both at water adsorption and at nitrogen adsorption tests, but the mix with quicklime or CEMI seems to eliminate this effect, maybe because of the low dosage, maybe because of the higher porosity of the medium given by CaO or CEMI. In particular CaO-MgO behave quite similarly to CaO 10% on the porosity point of view after 90 days of curing.
The presence of hydrotalcite in the XRD patterns of CaO compositions is not very evident because most of its peaks are superimposed with calcite, portlandite and C_4AH_X while the peak at 5.5° is not visible maybe because it is too close to the starting angle of the diffractometer, but in the compositions containing no CaO has a sharp peak at 11°C so we can affirm that it is present.
Calcite is inevitably present in CaO and CaO-MgO composition because the activator is partially carbonated, but the presence in the other compositions reveals that some carbonation

has spread. In particular from the DTGA MgO 10% seems particularly affected by carbonation and the use of quicklime as sole activator does not seem to stop the spreading.

5.4 Reaction kinetics

5.4.1 Ultrasonic setting test

The ultrasonic setting test allows us to study the setting process of the cement paste using mortar samples.

The fitted hardening curves of the studied compositions are shown in fig.??. As we can see the long-term behavior is essentially controlled by the presence of CaO in the mix of activators because the curves of ultrasonic wave speed of all the compositions using CaO converge after 30 hours. The curves of MgO 10% and CEMI 5% + MgO 5% converge after 36 hours and the final value of their ultrasonic wave speed is higher than the CaO compositions, meaning that they have reached higher stiffness according to the relation between Young's modulus and ultrasonic wave speed (equation 3.16).

The initial ultrasonic wave speed of MgO 10% and CEMI 5% + MgO 5% is higher than the other compositions and almost the double of CaO 5% + MgO5% but, while MgO 10% starts hardening immediately, CEMI 5% + MgO 5% has a dormant phase which is the longest among all the studied compositions, followed by a fast stiffness gain. All the CaO compositions are characterized by the dormant phase. The use of partially hydrated and partially carbonated quicklime and the addition of MgO seem to anticipate the beginning of the setting phase. The second derivative curve of CaO 10% does not intersect the time axis but, analyzing the shape of peak immediately after the vertical asymptote, we can reasonably conclude that the setting occurs between 12.68 and 13.62 h.

The initial and final setting times corresponds to the null values of the second derivative of ultrasonic speed, after the vertical asymptote if present.

Composition	Dormant phase [h]	Initial setting time [h]	Final setting time [h]
CaOd 10%	11.37	14.4	16.4
CaO 10%	10.23	12.68	13.62
MgO 10%	-	4.13	5
CaO 5% + MgO 5%	8	11.71	18.11
CEMI 5% + MgO 5%	19.167	21.61	28.8

Table 5.4: Setting times

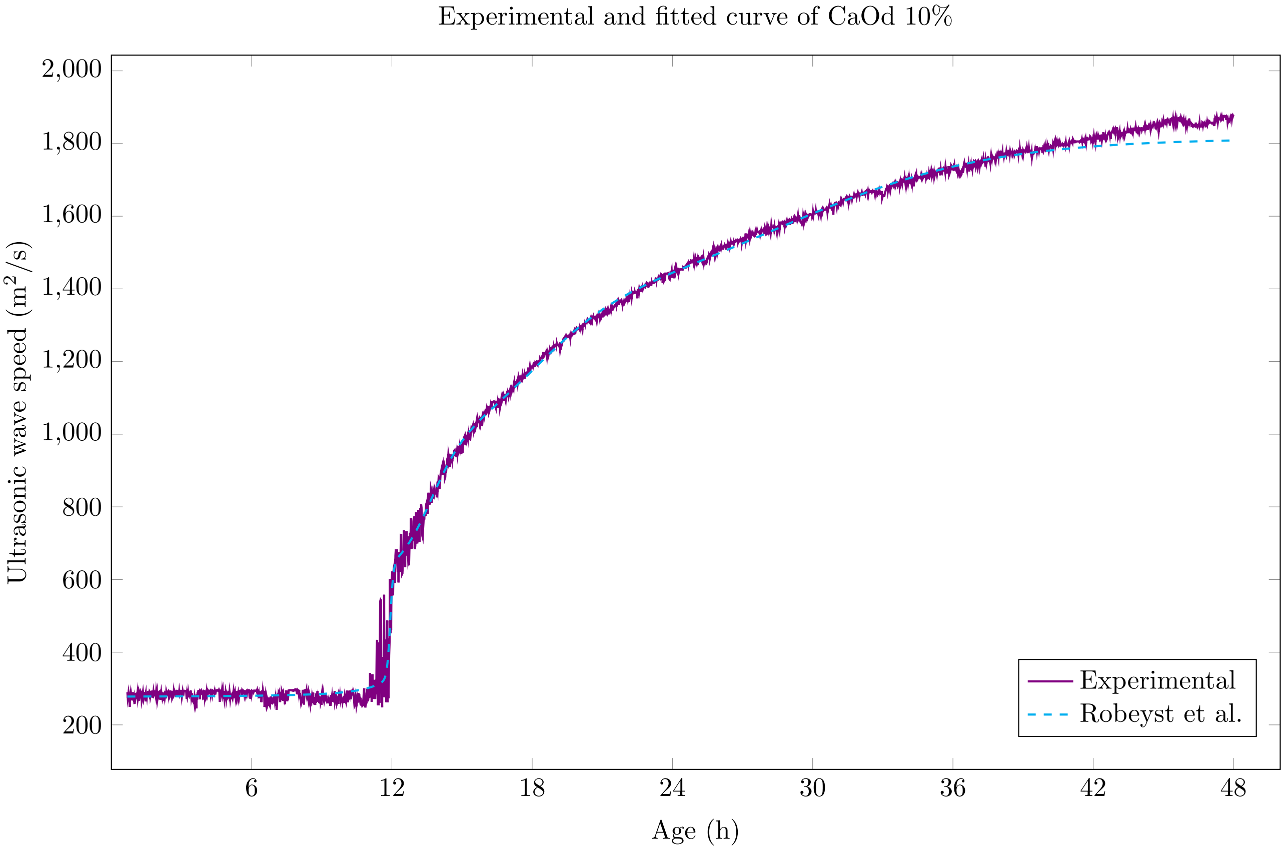

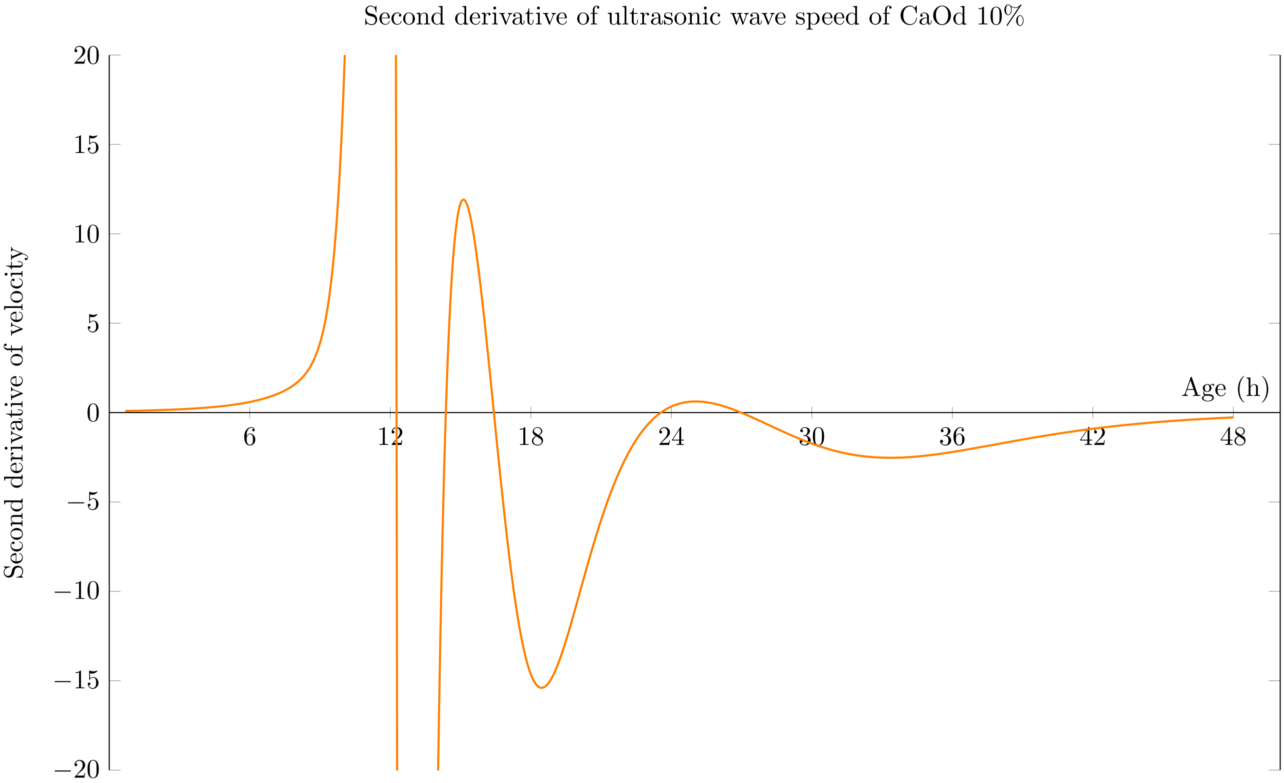

Figure 5.20: Setting curves of CaOd 10%

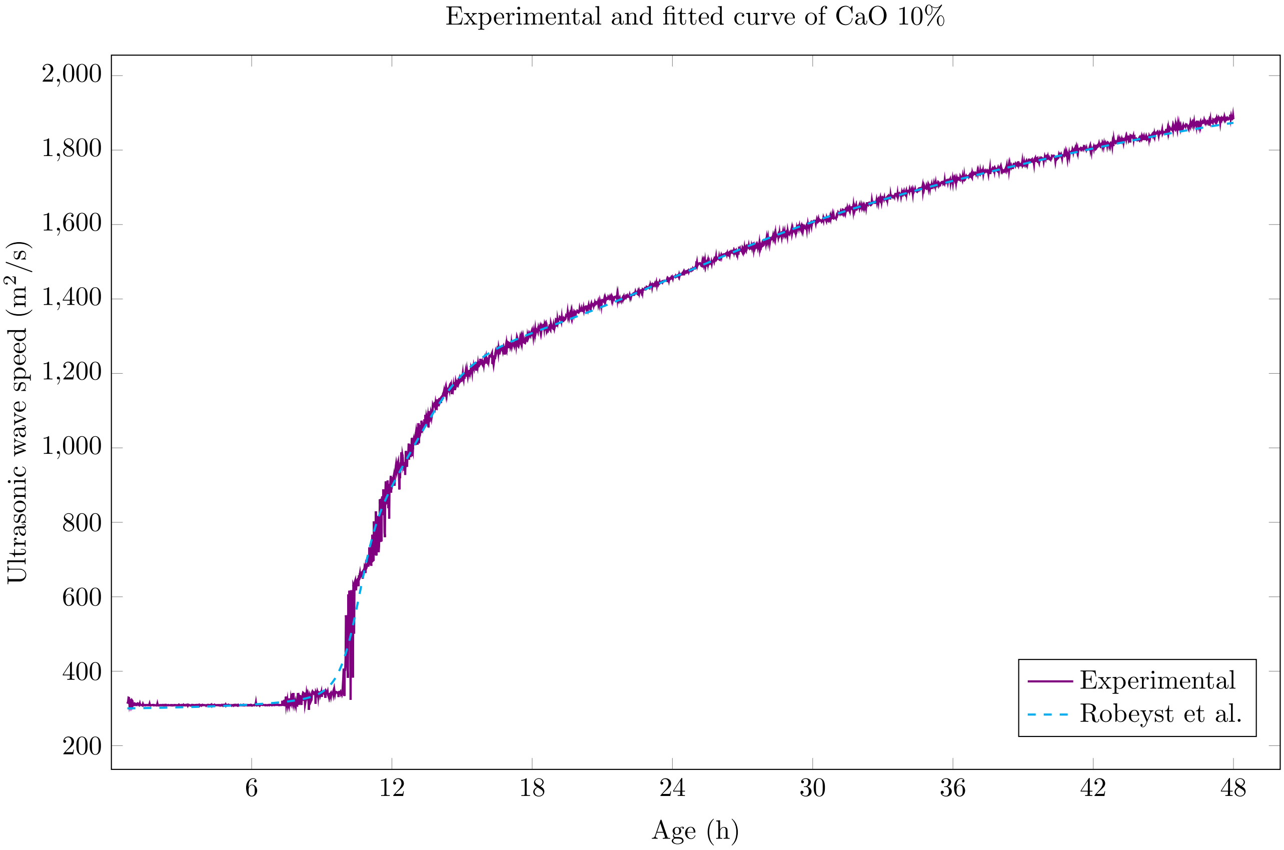

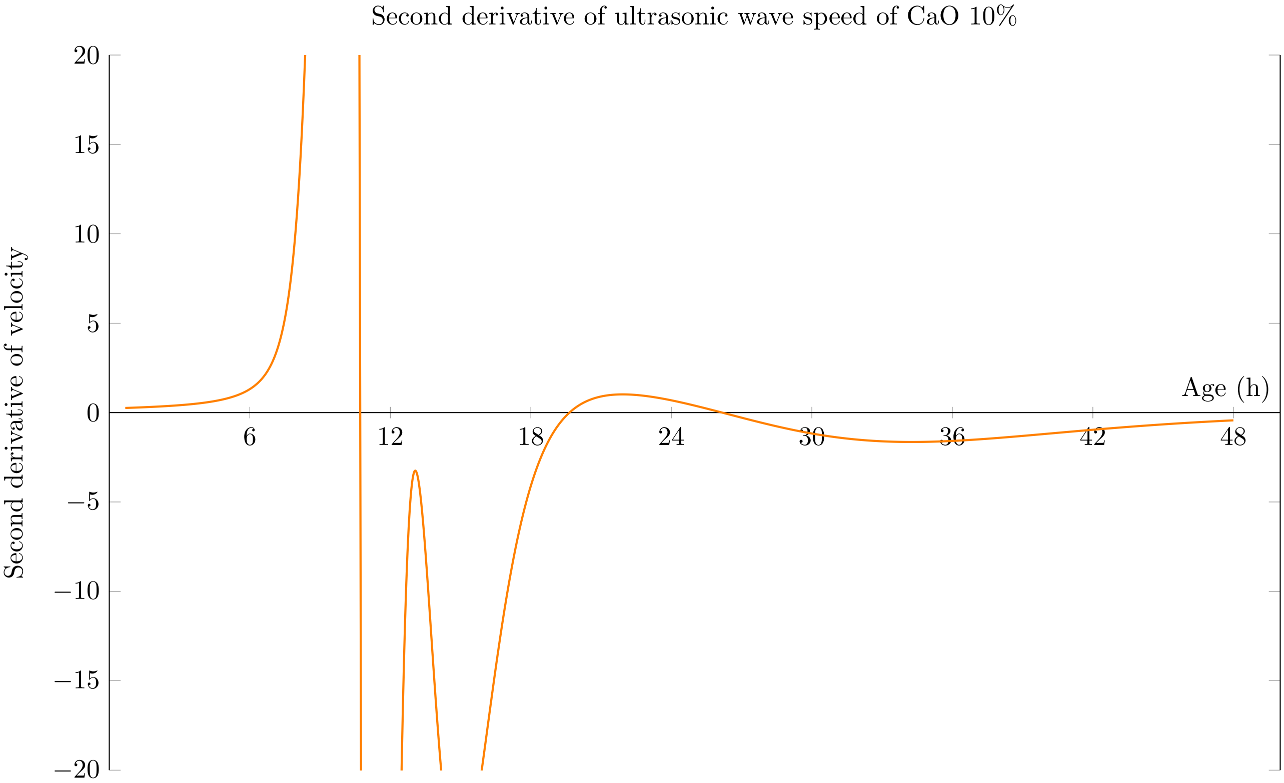

Figure 5.21: Setting curves of CaO 10%

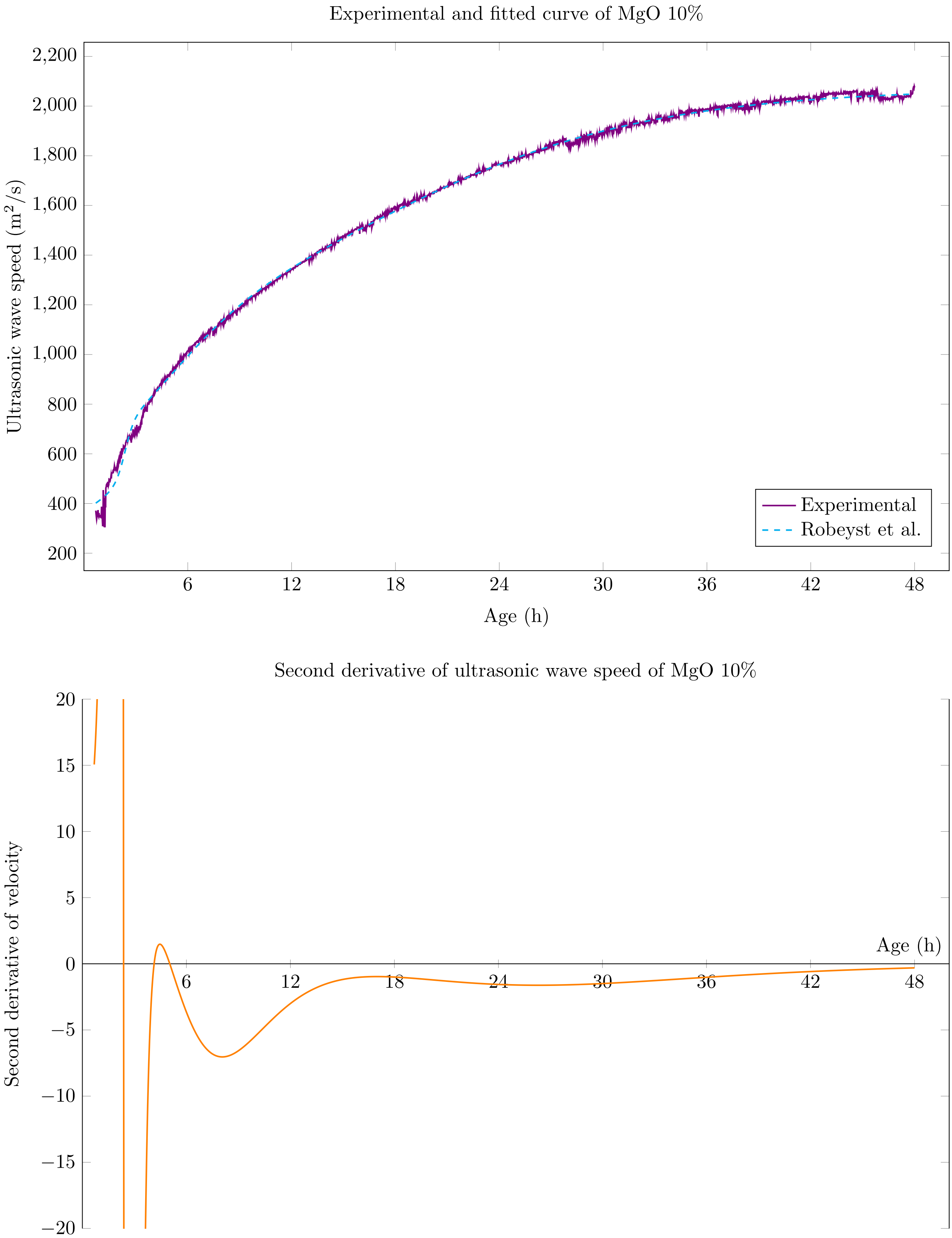

Figure 5.22: Setting curves of MgO 10%

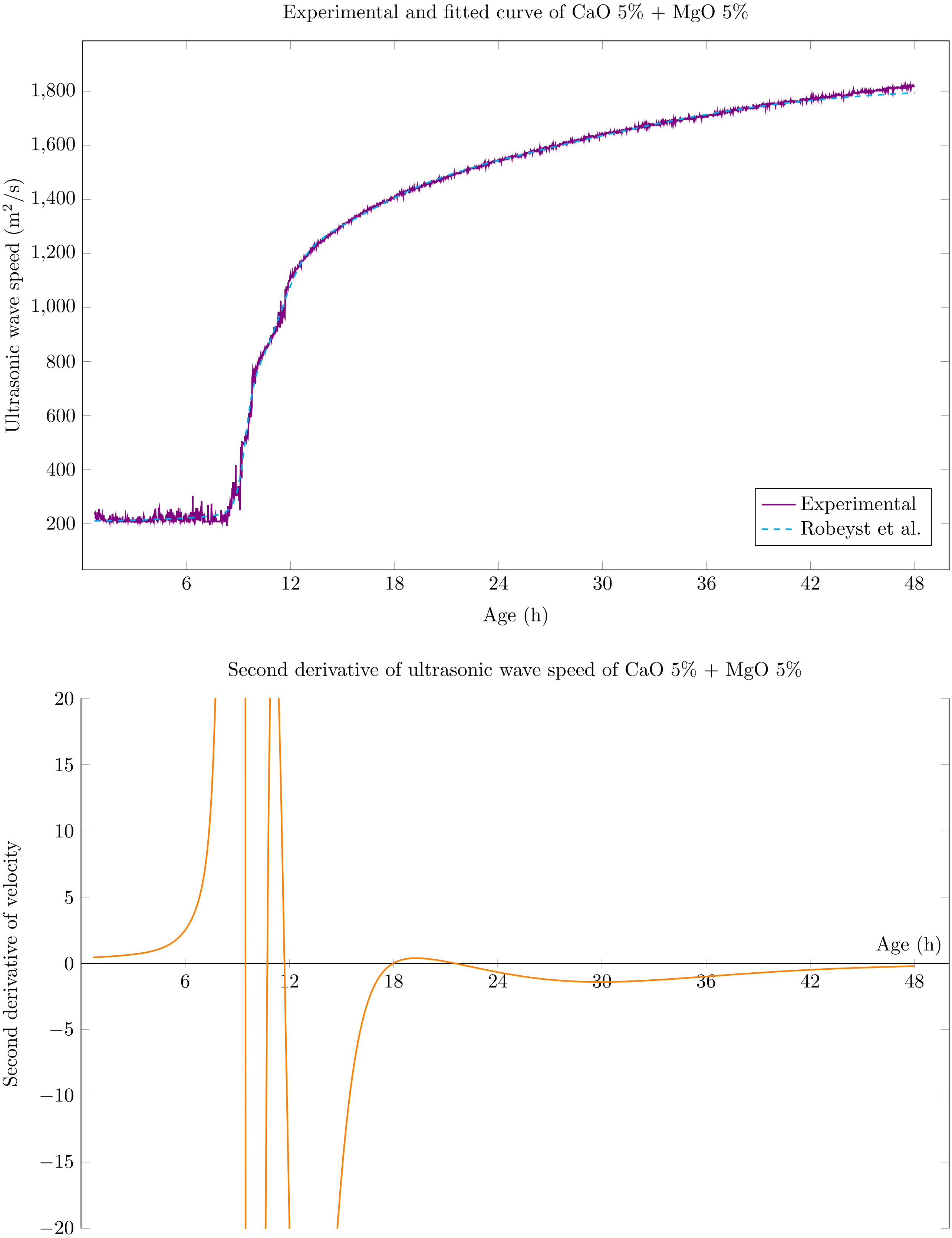

Figure 5.23: Setting curves of CaO 5% + MgO 5%

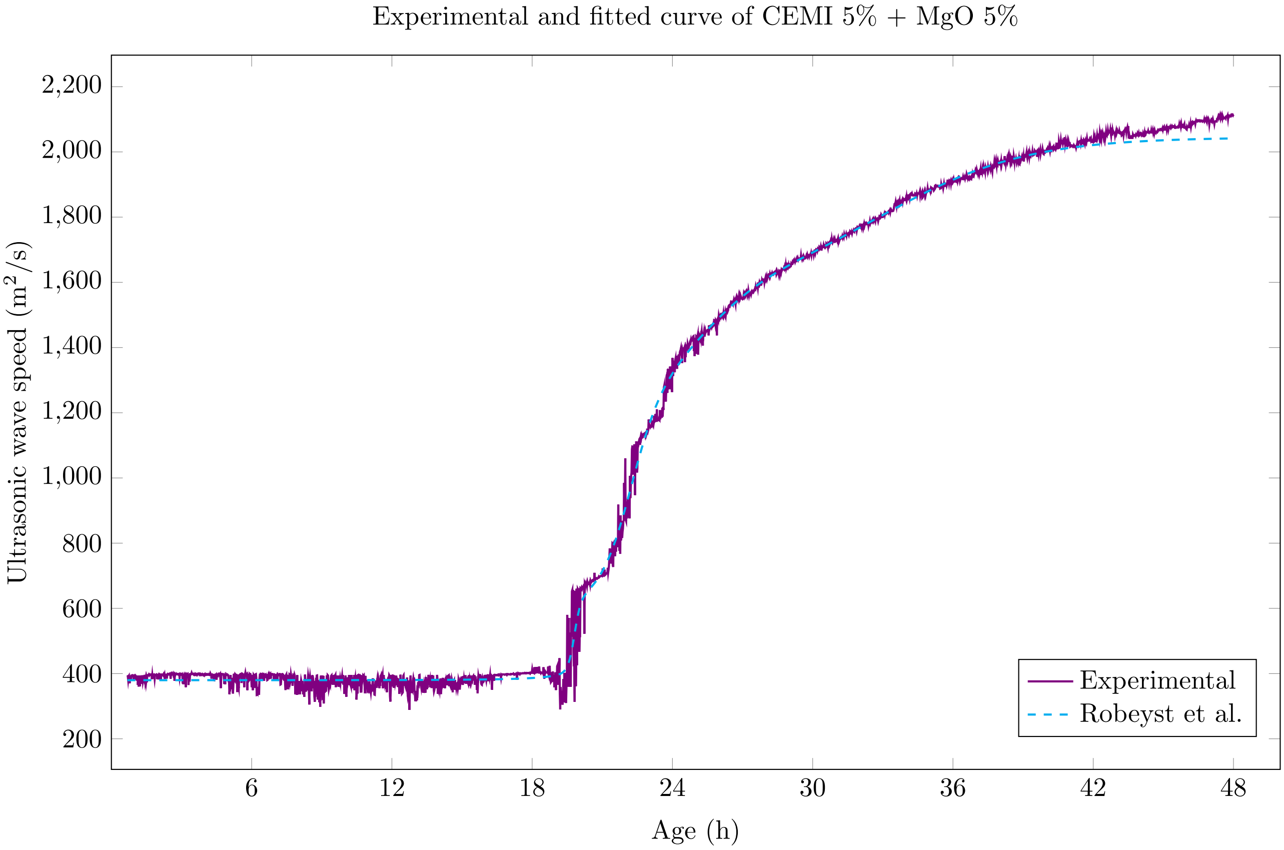

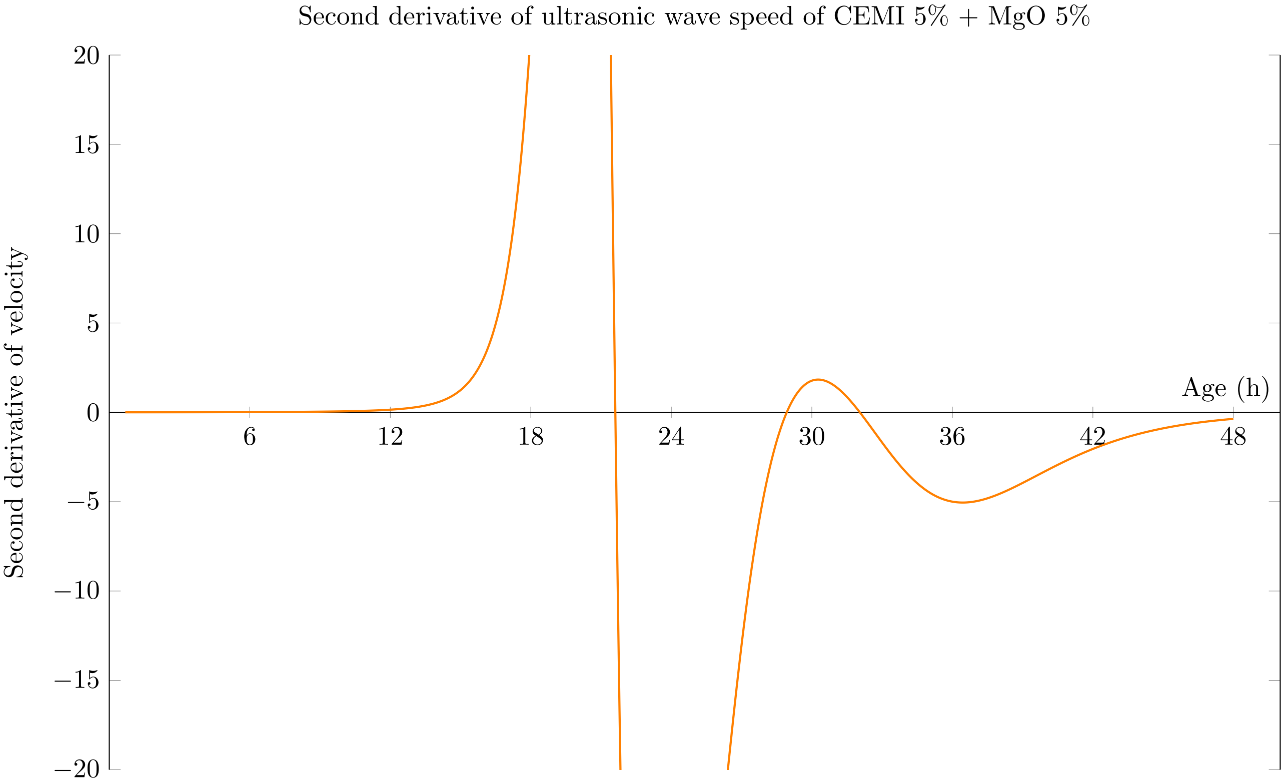

Figure 5.24: Setting curves of CEMI 5% + MgO 5%

5.4.2 Semiadiabatic calorimetry

CaOd 10% and CaO 10% have an initial temperature peak due to the extinction of CaO but the maximum temperatures reached during the hydration of BFS are below 30°C and the peaks are reached after 20 to 30h. CEMI 5% + MgO 5% shows a delayed temperature rise reaching the peak at around 50h and the maximum value is a bit lower than the first two compositions. MgO 10% reaches the maximum temperature of about 36.5°C at 40h, which is the highest temperature reached among all the compositions. With CaO 5% + MgO 5% the initial temperature peak reappears but its value is lower than the other CaO compositions. On the contrary after the extinction of quicklime the temperature path follows the one of MgO 10% albeit reaching a lower peak value (31°C), which is the second highest, at earlier age (20h). The initial temperature peaks of CaO compositions affect the calculation of the cumulated hydration heat which shows a local minimum at early age. We have decided not to reinitialize the calculation at these points of minimum because they occur at different ages (4.16h for CaOd 10%, 7.5h for CaO 10%).

All the compositions but MgO 10% show very similar cumulated hydration heats after 200h, that has been assumed as the endtime of our analysis, which are between 135 and 145 J/g. CaO compositions release most of their heat during the first 60 hours while CEMI 5% + MgO 5% in the first 100h. MgO 10% shows the highest cumulated hydration heat (about 175 J/g) which also develops with the highest rate, being released in the first 60 hours.

The lower final hydration heat of CaO 10% compared to CaOd 10% is bit lower and this result goes in opposite direction with the one obtained by Kim et al., who found that using $Ca(OH)_2$as activator produces more heat than using CaO.

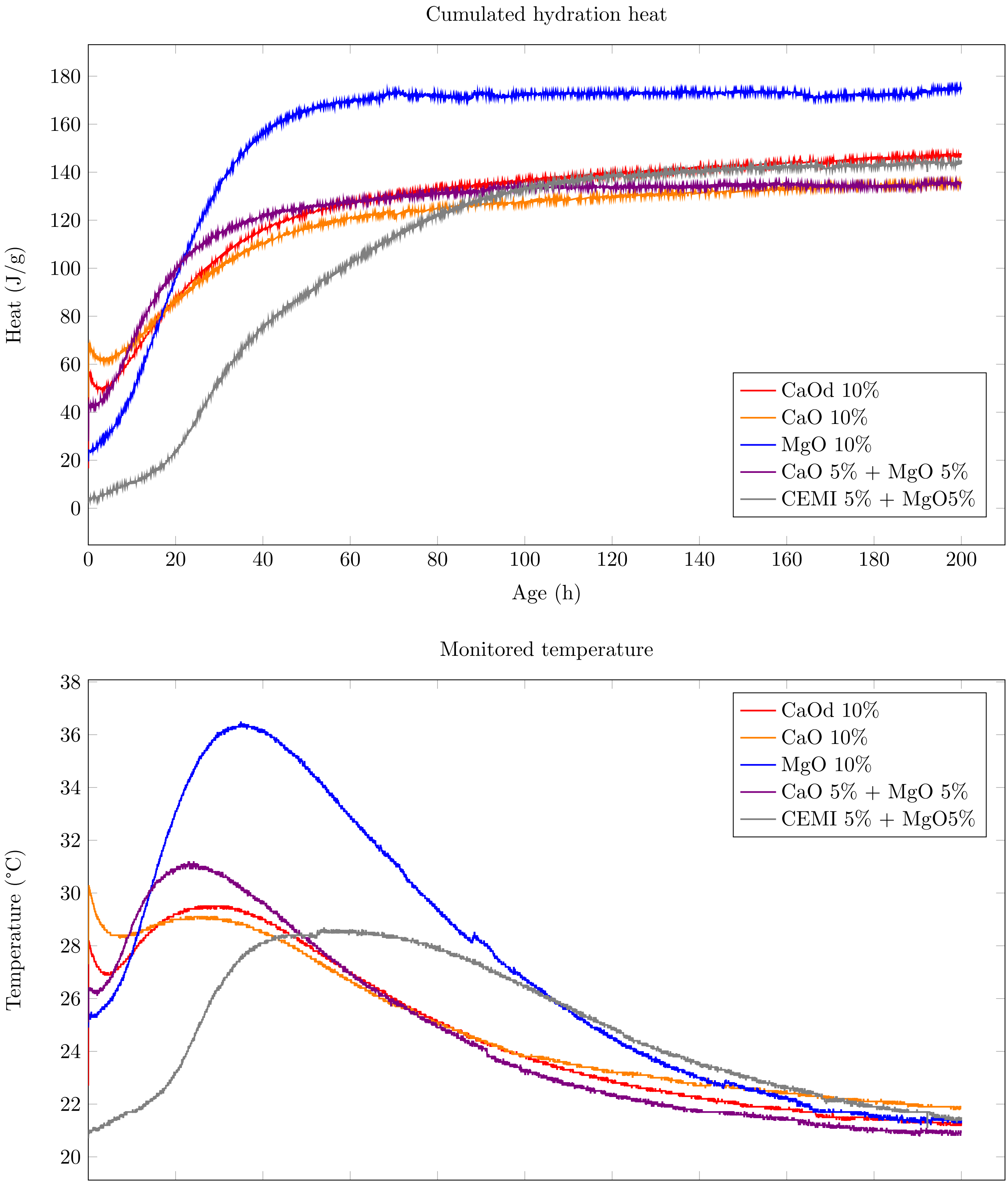

Figure 5.25: Hydration heat curves

5.4.3 Delayed deformations

Delayed deformation in autogenous curing conditions

As shown in fig.5.26, the mass variation of the samples cured in aluminum paper is negligible and for this reasons we can affirm that autogenous conditions have been ensured.
Quicklime compositions show an initial expansion, probably due to the formation of $Ca(OH)_2$, followed by an important shrinkage that occurs in a couple of days and an approximately constant behavior until 35 days. After this age it seems that the cement pastes continue shrinking but the number of measures are not enough to confirm this observation. The two compositions have similar initial expansions but the early-age shrinkage is more important as the used quicklime contains more pure CaO: the shrinkage of CaO 10% composition has the same magnitude of the initial expansion and completely compensates it while the shrinkage of CaOd 10% is more important. MgO 10% has a behavior quite similar to CaOd 10% but, after the first week of curing, the deformation is stable until 28 days and then the shrinkage starts.
The two compositions that use magnesia mixed with lime or Portland cement show a completely different behavior characterized by a more important initial expansion followed by a limited shrinkage until 30 days, unable to compensate the initial expansion, and an apparent subsequent expansion.

Delayed deformations in water excess curing conditions

Fig.5.27 shows that the compositions can be divided in two groups based on the deformative behaviors: compositions using CaO in the activator mixes and compositions that does not use CaO.
The first group presents an initial expansion that takes place in the first 7 days followed by a stabilization of the deformation. CaO 5% + MgO 5% seems to expand less than the other CaO-based compositions.
MgO 10% and CEMI 5% + MgO 10% on the contrary show monotonically expansive behaviors reaching deformations higher than 400 $\mu m/m$. The compositions containing CEMI expands more in the first 35 days of curing than MgO 10% but the measures have been stopped sooner. Likely the CEMI compositions would show a more important expansion compared to MgO 10% if we continued measuring at later ages.
On the side of the variation of mass a distinction can be done between compositions that use mixes of activators of different natures or activators of the same types. All the compositions tend to gain mass and the initial mass loss of CaO 5% + MgO 5% and CEMI 5% + MgO 5% may be due to a measure mistake. In particular MgO 10% is the compositions having the highest mass increment. The mass increments are due to both the formation of hydration products both the spread of carbonation.

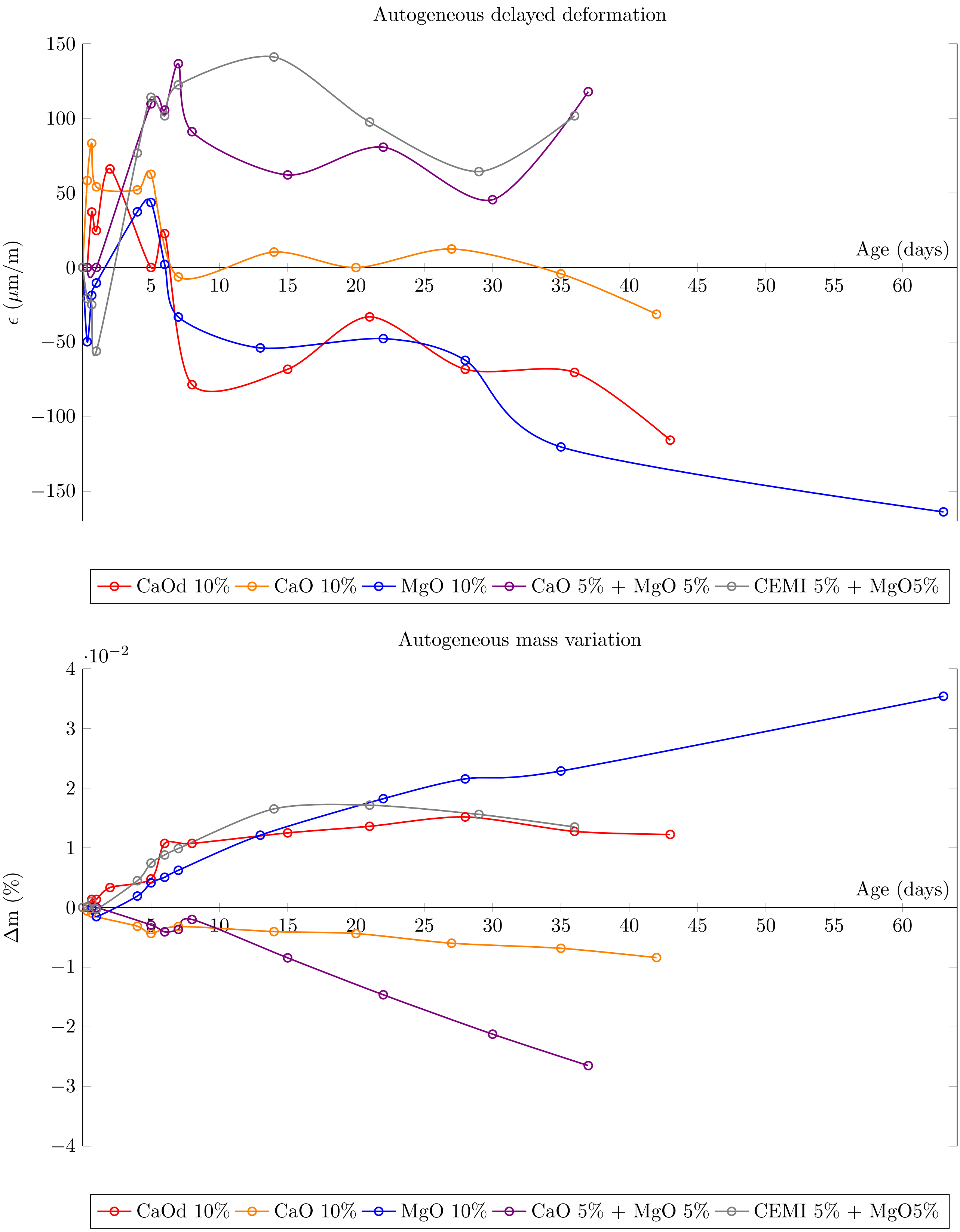

Figure 5.26: Autogenous delayed deformations

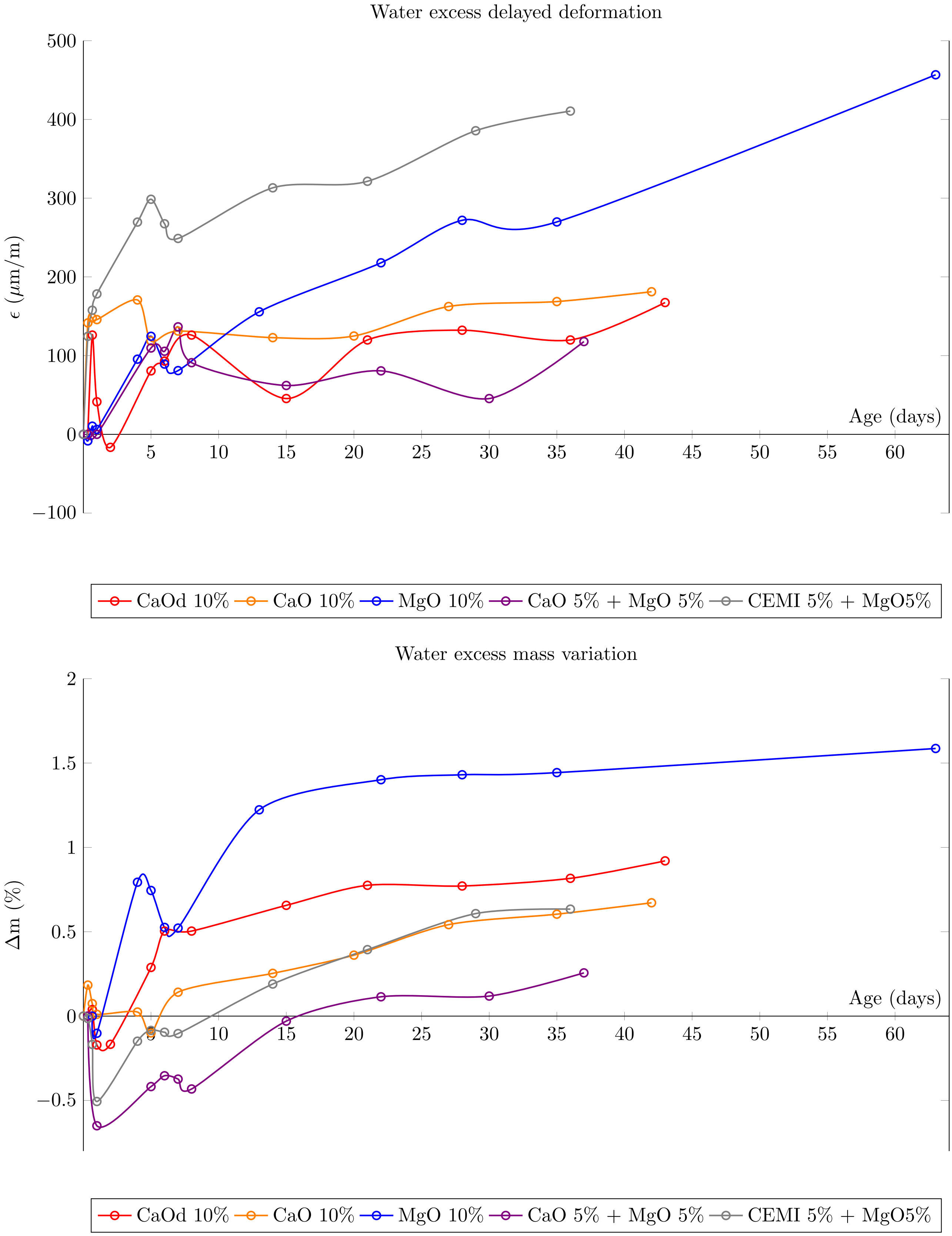

Figure 5.27: Water excess delayed deformations

5.4.4 Conclusions

Despite of the high reactivity of CaO when mixed with water, MgO seems to be able to better activate the hydration of BFS, except when it is mixed with Portland cement. In this case it would be interesting to study the effects of different MgO and Portland cement dosages.

The setting of MgO 10% is much faster compared to the other compositions and does not present the initial dormant phase. MgO 10% produced also the highest hydration heat and reached the highest temperature recorded by the calorimeter. On the side of delayed deformations it is well known that brucite provokes expansion and its formation is well evident in the case of water excess curing conditions while in endogenous curing condition the lower quantity of water available limits its formation and shrinking behavior occurs.

Mixing MgO with the uncalcinated quicklime changes a lot the behavior of the composition. The dormant phase reappears and the setting is delayed; the cumulative hydration heat is reduced to values comparable with the other CaO compositions and the peak temperature is reduced as well; the delayed deformations are characterized by an initial expansion followed by a stable phase of similar magnitude no matter the curing conditions. This delayed deformation behavior may be related to the initial slump, which is more than 3 times higher than MgO 10%, meaning that more free water is available for the formation of brucite, and the higher accessible porosity, which leaves space for the precipitation of brucite without causing expansive phenomena.

Mixing MgO and CEMI has effects that are on certain aspects similar to the mix with CaO and on others to the use of only MgO. The dormant phase is twice longer than the CaO-MgO mix and the initial setting time is 10 hours delayed, but the setting phase requires 7 hours in both cases; the cumulative hydration heat after 200h is a bit higher but the peak of temperature is reduced and delayed by 40h. The delayed deformations behave as CaO-MgO in endogenous conditions but, when an excessive quantity of water is present, an expansive behavior with deformation magnitude higher that MgO 10% has been observed. Compared to CaO-MgO mix, CEMI-MgO has a similar slump, so a quantity of free-water that allows the formation of brucite in endogenous conditions is available, but the porosity is lower, comparable to CaOd 10% and this may justify the different behavior in water excess conditions.

Both the quicklime-based compositions have a dormant phase that is 1 hour shorter in the case of uncalcinated quicklime. The use of calcinated quicklime seems to both decelerate the setting and to delay it by a couple of hours. Despite the higher mixing temperature of CaOd 10%, the initial temperature of CaO 10% measured by the calorimeter is lower and the hydration heat in the first 20h is a bit higher; after 200h uncalcinated CaO produces both higher cumulative heat and higher peak temperature, despite the differences are not very relevant. Using uncalcinated quicklime seems to limit the magnitude of shrinkage in endogenous conditions, albeit not changing the deformative behavior, probably because of the higher quantity of free water related to the higher slump, while no important difference has been noted in water-excess conditions.

Compared to OPC, whose delayed deformations are shown in fig.5.28, the autogenous delayed deformations have a much lower magnitude.

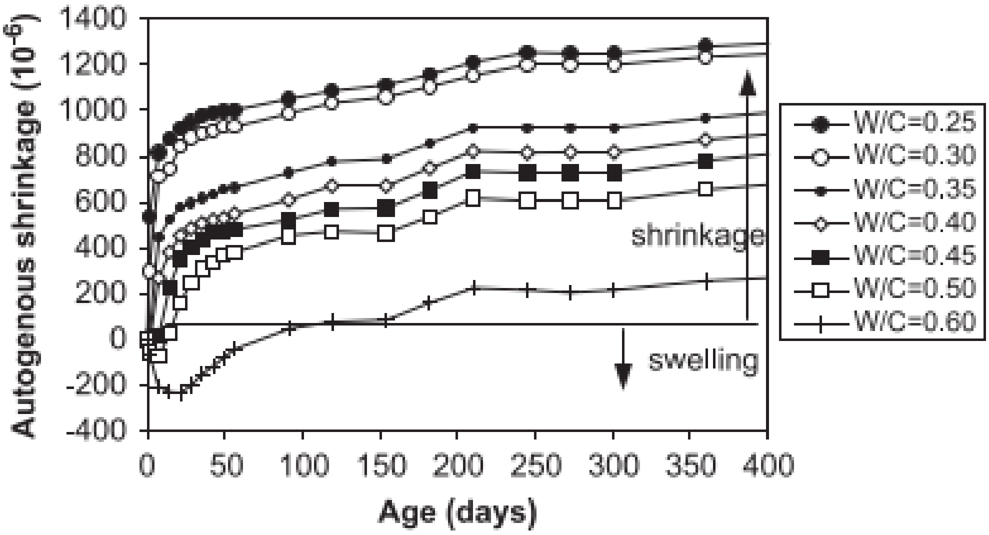

Figure 5.28: Shrinkage of ordinary Portland cement [26]

5.5 Physical and mechanical characteristics

5.5.1 Dynamic Young's modulus

The estimation of the dynamic Young's modulus using ultrasonic waves is a procedure that contains a lot of uncertainties that are due to variables like the presence of trapped air and voids in the hardened sample, the irregularity of the surfaces, the quantity of glycerol, the positions of the emitter and the receiver but is able to provide a good qualitative estimation.
CEMI+MgO composition is the only one showing a 3 days Young's modulus too low to be detected, which is coherent with the results of the ultrasonic hardening test, that rapidly increases in the first month of curing.
According to the results reported in fig.(5.29) CaO gives a good stiffness after 3 days but the increment between 7 and 28 days is very little (the decrement in CaO 10% may be due to measure mistakes or issues in the sample) while after 90 days calcinated CaO allows to reach a higher stiffness, at the same level of CEMI+MgO. The CaO+MgO mix floows the same path of CaO 10% but starts with a lower stiffness after 3 days of curing.
MgO 10% has no stiffness gain between 7 and 90 days. On the contrary the randomness of the measure grows enormously. It is worth noting that the mechanical essays on MgO 10% at 90 days have been repeated on 3 more samples in order to eliminate any eventual issues in fabrication, curing and measure, but the results were confirmed: no stiffness gain and high randomness. The suspects of internal cracking due to the precipitation of brucite become more concrete.

5.5.2 Flexural and Compressive strength

The strength of the compositions is shown in fig.5.30 and fig.5.31.
After 28 of curing calcinated lime, magnesia and CEMI-MgO mix provide the same compressive strength and CEMI+MgO has the biggest gain in the first 7 week of curing. MgO 10% shows a

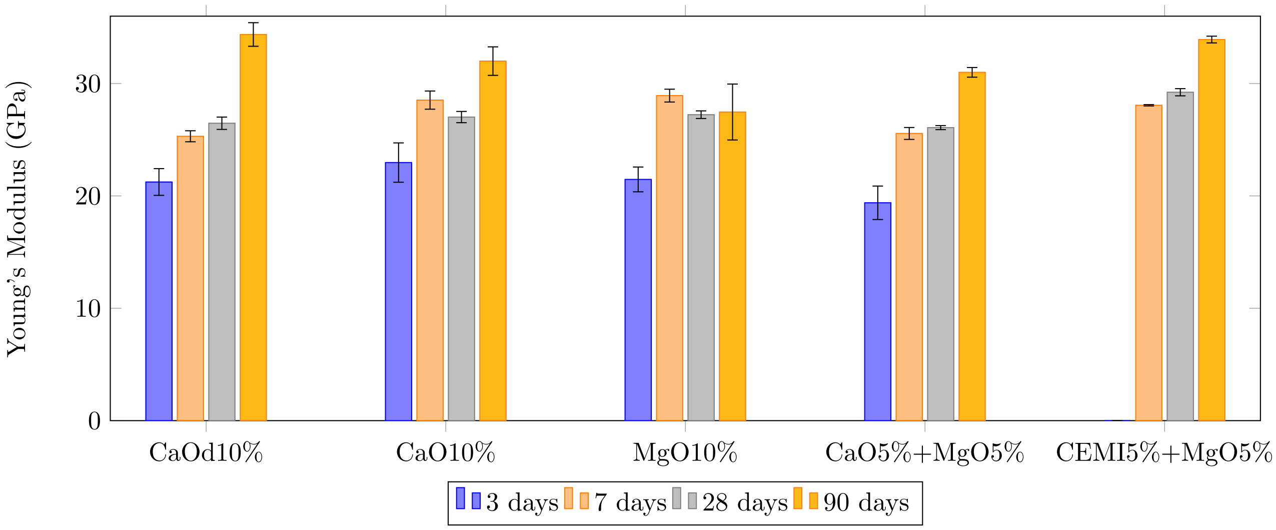

Figure 5.29: Dynamic Young's modulus

decrease of compressive strength after 90 days together with a great randomness, showing that the formation of brucite does compromise the paste soundness and integrity.
The use of uncalcinated quicklime reduces the compressive strength, coherently with the results of Kim et al. and mixing CaO and MgO in equal parts does not improve the strength compared to the use of uncalcinated quicklime.
MgO 10% shows the highest flexural strength after 7 and 28 days but then it looses performances. The loss of strength occurs to CaO+MgO composition too, probably because of the precipitation of brucite. CEMI+MgO gains most of its flexural strength between 7 and 28 days which is quite unexpected compared to the important gain of compressive strength in the first 7 days. The use of uncalcinated quicklime decreases the performances in this case too and the mix of CaO and MgO does not remediate to this loss but is detrimental for the flexural strength at late age.

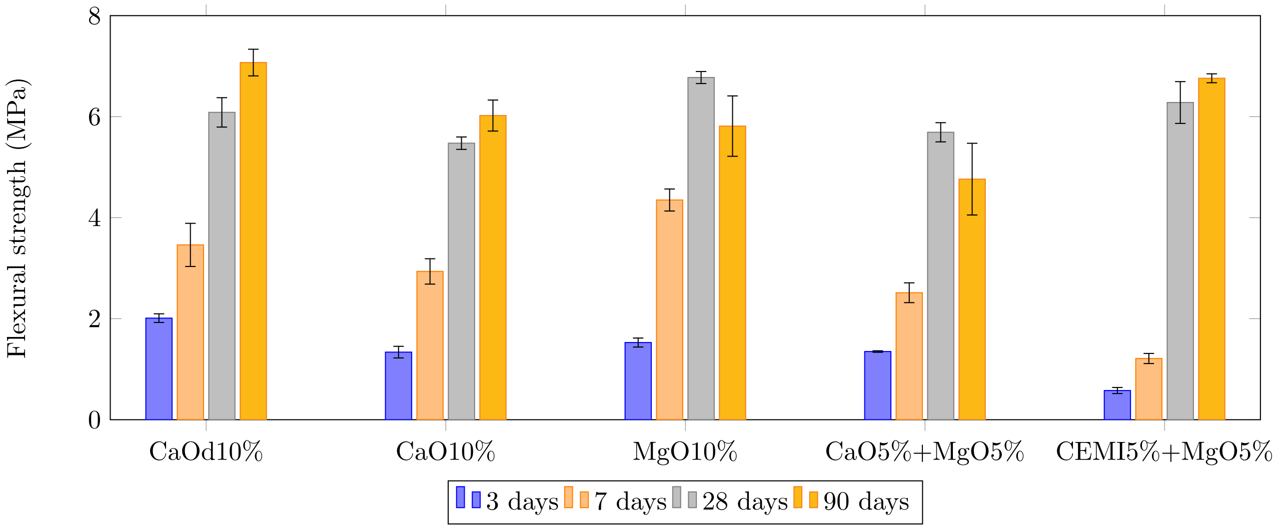

Figure 5.30: Flexural strength

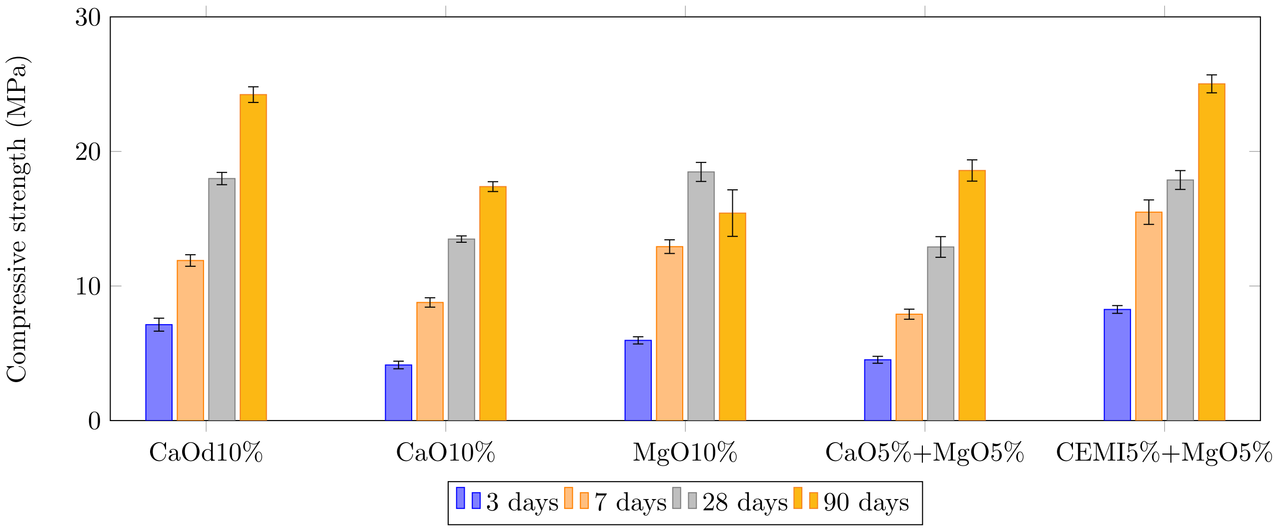

Figure 5.31: Compressive strength

5.5.3 Measure of the pH

All the compositions have a intial pH above 12. Quicklime compositions have almost constant pH along the entire curing period, with the one of CaO-MgO mix being a bit higher. The pH of MgO 10% starts below 12.5 and then increases until the same level of quicklime compositions. On the contrary the pH of CEMI-MgO composition reaches the maximum after 7 days of curing and then it starts decreasing. Maybe the sample tested after 90 of curing was carbonated or carbonation spread during the preparation.

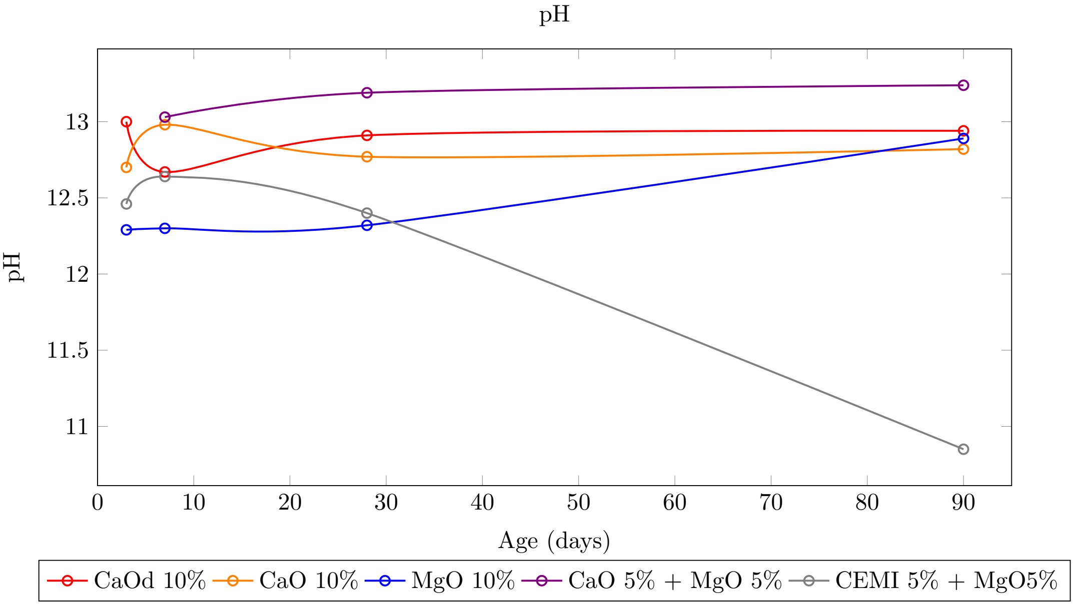

Figure 5.32: pH

5.6 Effects of reduction of the w/b ratio

The w/b has been set at 0.55 because it is the minimum value that allows the CaOd and MgO compositions to be casted without the use of plasticizing additives. This ratio is very high for the others compositions and gives problem of stability of the mortar during the Abrams' cone essay and some segregation.

A tentative to maximize the mechanical performances has been done on compositions CaO 10% and CEMI 5% + MgO 5% which have margins for the reduction of the w/b ratios. The ratios have been reduced until the slump was 3.5 cm for CaO composition (there is some more margin to reduce the slump to 2 cm) and 2 cm for the CEMI+MgO composition. The mechanical tests have been performed at the usual curing ages and the results are shown in fig.5.33 and fig.5.34. In the case of CaO 10% composition the reduction of the w/b ratio benefits the strength at every age and provides performances that are very similar to CaOd 10% and, considering that the slump can be further reduced, more improvements can be achieved. The reduction benefits CEMI+MgO composition in a more complicated way: only the flexural strength improves in the first week while the compressive strength decreases but, after 28 days the flexural strength is reached and then overpassed while the compressive strength is higher and, after 90 days, it reaches 30 MPa, the highest value obtained in the present study.

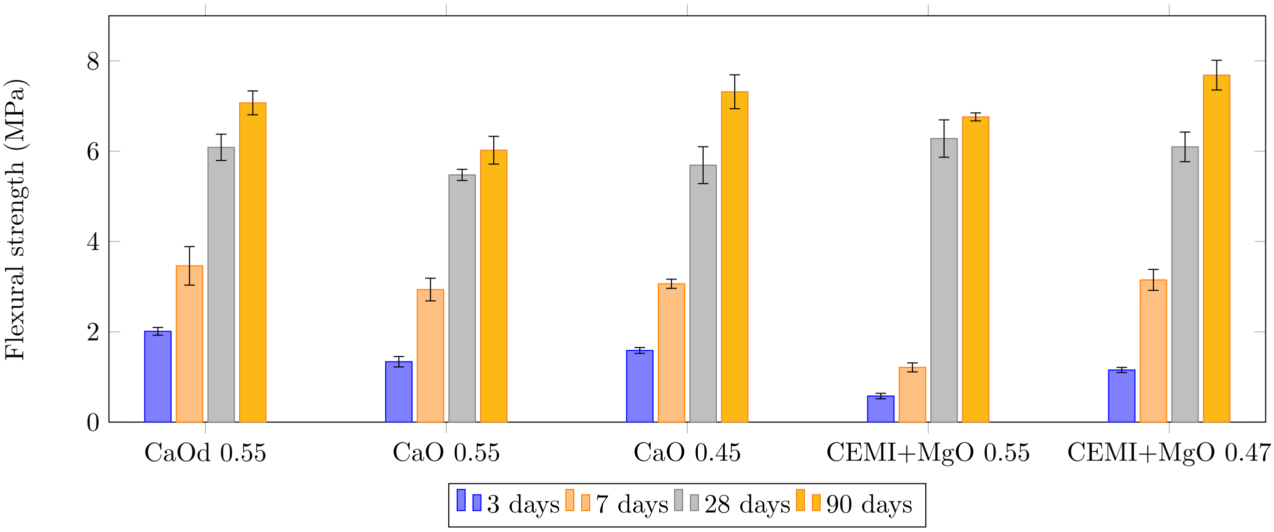

Figure 5.33: Flexural strength of the optimized compositions

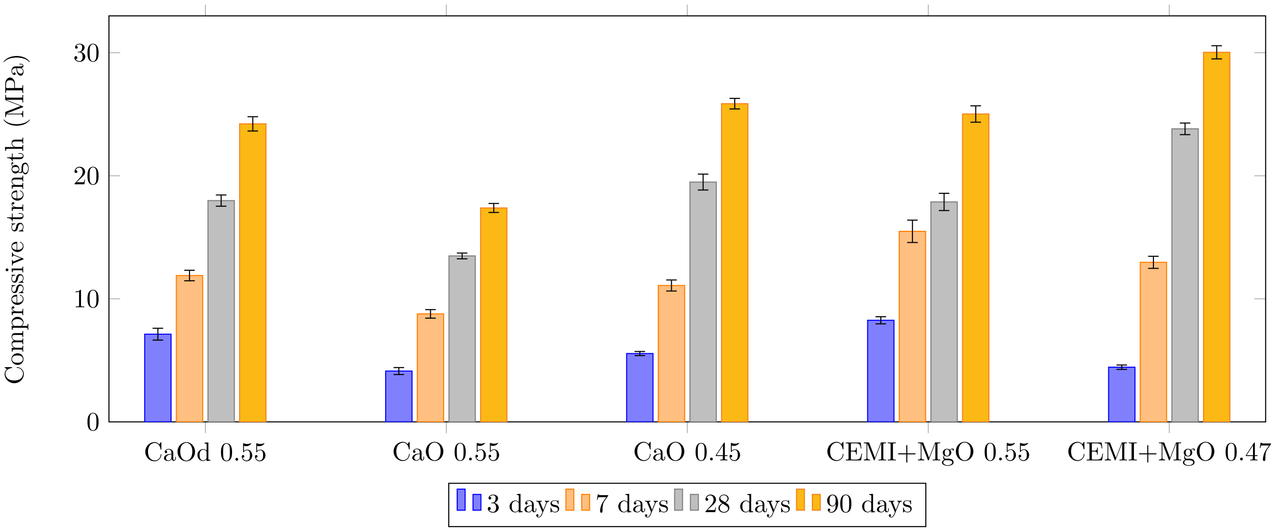

Figure 5.34: Compressive strength of the optimized compositions

Chapter 6

Conclusions

6.1 Perspectives and critical aspects of the use of CaO

The interest in using quicklime as activator for BFS is manly due to the fact that it is a very cheap and widely available material, while traditional studied activators as sodium hydroxide are much more expensive: Kim et al. [24] report that in South Korea the price of CaO and $Ca(OH)_2$was US$90 per ton while the price of NaOH was US$590 per ton in 2013. In addition to that CaO is safer to handle compared to NaOH.

At the same w/b ratio CaO has been reported to be more effective than $Ca(OH)_2$but the present study shows that relation between the nature of the activator, the w/b and the strength is more complicated because it is possible to reach the same strength using partially hydrated lime by calibrating the w/b. The dissolution of the amorphous structure of BFS occurs in an alkaline environment which is generated by the dissolution of $Ca(OH)_2$in Ca^{2+} and OH^- ions. CaO reacts with bulk water forming $Ca(OH)_2$which then dissolves in the remaining free water increasing the pH. Part of the bulk water is thus incorporated into the activator and the w/b ratio is thus reduced. We shall conclude that the lower strength obtained by Kim et al. is not due to the nature of the activator but to the higher effective w/b ratio of $Ca(OH)_2$composition compared to the CaO composition.

This observation may simplify eventual practical applications of quicklime-activated BFS because CaO is able to react with the water steam present in the air, so it does not seem necessary to stock the quicklime in humidity controlled environments or to calcinate it before use because it is possible to match the same performances of pure CaO by calibrating the w/b ratio. Furthermore the partial hydration of lime does not seem to have significant effects on the setting time nor on the hydration heat and peak temperatures. It would be interesting to study the use of extinguished quicklime as activator because it is mainly $Ca(OH)_2$(some carbonation occurs and the achievable reaction degree is below 100%) and this could provide a good control of the w/b ratio.

Another critical aspect is the composition of the BFS and its specific surface area. It seems that higher SSA and lower MgO content allow to reach better mechanical performances: the first aspect has been studied by Burciaga-Díaz [17] while, comparing its studies with the ones made by Kim et al. and Gu et al., lower MgO content seem to provide higher mechanical strength.

Shrinkage in autogenous conditions seems to be reduced compared to OPC while in water excess conditions the behavior is stable.

In is quite hard to imagine eventual applications of CaO activated BFS. The achieved strength are low compared to the important quantities of binder that have been used and the calibration of the w/b according to the quantity of water needed to extinguish the quicklime is problematic. The concern on the use of CaO as activator for BFS hydration is quite recent and many progress can be achieved by exploring different CaO dosages, different BFS characteristics and different activator preparation techniques that may include the quicklime extinction ad drying before mixing with BFS. Because of the low hydration heat and shrinkage compared to ordinary Portland cement may result in applications as reparation mortars.

6.2 Perspectives and critical aspects of the use of MgO

The main issue that we have found is the high reactivity of the MgO compared to the BFS. Among the studied products MgO is the one that activates the BFS the fastest, as we can see from the setting times, produces the highest hydration heat and reaches the highest peak temperature. Despite a fast strength gain the use of this MgO product results in a cement paste that has a low porosity but that is also unstable and looses strength.

Additive and inherent MgO are consumed, after the activation of the BFS, to form hydrotalcite by combination with alumina but the XRD and DTGA tests have shown that a little hydrotalcite is present while the presence of brucite is important, meaning that the consumption rate of MgO to form hydrotalcite is very low compared to the rate of formation of brucite. Brucite is an expansive product and can be used to compensate shrinkage [39, 1] but its presence can be detrimental for the paste soundness because, precipitating in a low porosity medium, the tensile forces that appears as consequence provoke the formation of cracks. The BJH pore size distribution, the water porosity test and the measures of delayed deformations confirm that this is the cause of the observed loss of strength.

Mixing MgO and CEMI seems to compensate the detrimental effect of brucite precipitation by increasing the porosity, which leads to the best compressive strength after 7, 28 and 90 days of curing but a delayed development of stiffness and flexural strength. The addition of CEMI also delays the setting and reduces the peak temperature but does not reduce the cumulative hydration heat.

The hydration of MgO takes an important quantity of water because of the high SSA (around 4 times the CaO) and this is visible from both the little slump and the shrinkage behavior: in autogenous conditions the samples shrink while in wet room curing conditions brucite keeps forming and the result is an expansion. The mix with CEMI leads to a compensation of the shrinkage in autogenous conditions but increases the expansion in wet room conditions, maybe because the higher porosity allows more water to penetrate inside the mortar and react with the MgO. A SEM analysis should be done to confirm the presence of cracks.

The mix with CaO instead of CEMI makes the composition behave more similarly to CaO ones in terms of porosity, setting times, hydration heat and strength, but some signs of instability are visible because of the loss of flexural strength after 90 days of curing.

In general the achieved strength are not very high probably because of the high w/b ratio, the wrong slag composition, the too low dosage of MgO and CEMI, the los SSA of BFS. It would be interesting to try changing these parameters to see if the results improve.

Acronyms

AAC	alkali-activated cements
BET	Brunauer-Emmett-Teller
BJH	Barrett-Joyner-Halenda
C(A)SH	calcium aluminum silicate hydrates
CSH	calcium silicate hydrates
GGBFS	Ground-granulated blastfurnace slag
FA	Fly ashes
LOI	loss on ignition
MSH	magnesium silicate hydrates
OPC	ordinary portland cement
SEM	scanning electron microscopy
DTGA	differential thermogravimetric analysis
XRD	X-ray powder diffraction

Bibliography

Books

[1] Abir Al-Tabbaa and Fei Jin. “Magnesia in Alkali Activated Cements. From formulation to application”. In: Mark Alexander Shand et al. *Magnesia Cements.* Ed. by Elsevier. 2020. ISBN: 9780123919250.

[2] Kalliopi Aligizaki. “Gas adsorption. Testing, interpretation and requirement”. In: *Pore Structure of Cement-Based materials.* Ed. by Taylor Francis. 2006. ISBN: 0419228004.

[3] Kalliopi Aligizaki. “Introduction. Testing, interpretation and requirement”. In: *Pore Structure of Cement-Based materials.* Ed. by Taylor Francis. 2006. ISBN: 0419228004.

[4] Kalliopi Aligizaki. “Specimen pretreatment. Testing, interpretation and requirement”. In: *Pore Structure of Cement-Based materials.* Ed. by Taylor Francis. 2006. ISBN: 0419228004.

[5] Luca Bertolini. *Materiali da costruzione. Degrado, prevenzione, diagnosi, restauro.* Ed. by Città Studi. Vol. 2. 2012. ISBN: 9788825173680.

[6] Luca Bertolini and Maddalena Carsana. *Materiali da costruzione. Struttura, proprietà e tecnologie di produzione.* Ed. by Città Studi. Vol. 1. 2014. ISBN: 9788825173963.

[7] William I.F. David. “Powder Diffraction: By Decades”. In: *Uniting electron crystallography and powder diffraction.* Ed. by Springer. 2012. ISBN: 9789400755857.

[8] Lynne McCusker and Christian Baerlocher. “Structure Solution - An Overview”. In: *Uniting electron crystallography and powder diffraction.* Ed. by Springer. 2012. ISBN: 9789400755857.

[9] Mark Alexander Shand. “Manufacture of magnesium oxide for magnesia cements”. In: Mark Alexander Shand et al. *Magnesia Cements.* Ed. by Elsevier. 2020. ISBN: 9780123919250.

[10] Mark Alexander Shand and Fei Jin. “Introduction - Characterization of MgO. From formulation to application”. In: Mark Alexander Shand et al. *Magnesia Cements.* Ed. by Elsevier. 2020. ISBN: 9780123919250.

[11] Peter W. Stephens. “Rietveld Refinement”. In: *Uniting electron crystallography and powder diffraction.* Ed. by Springer. 2012. ISBN: 9789400755857.

[12] Pamela Whitfield. “Laboratory X-ray Powder Diffraction”. In: *Uniting electron crystallography and powder diffraction.* Ed. by Springer. 2012. ISBN: 9789400755857.

Articles

[13] Rehab O. Abdel Rahman and Michael I. Ojovan. “Life cycle of nuclear cementitious structures, systems, and components”. In: *Sustainability of Life Cycle Management for Nuclear Cementation-Based Technologies* (Jan. 2021), pp. 89–121. DOI: `10.1016/B978-0-12-818328-1.00012-5`.

[14] Mohammad Reza Asef and Mohsen Farrokhrouz. “A semi-empirical relation between static and dynamic elastic modulus”. In: *Journal of Petroleum Science and Engineering* 157 (2017), pp. 359–363. ISSN: 0920-4105. DOI: `10.1016/J.PETROL.2017.06.055`.

[15] Emad Benhelal, Ezzatollah Shamsaei, and Muhammad Imran Rashid. “Challenges against CO2 abatement strategies in cement industry: A review”. In: *Journal of Environmental Sciences (China)* 104 (2021), pp. 84–101. ISSN: 18787320. DOI: `10.1016/j.jes.2020.11.020`. URL: `https://doi.org/10.1016/j.jes.2020.11.020`.

[16] William Henry Bragg and William Lawrence Bragg. “The reflection of X-rays by crystals”. In: *Proceedings of the Royal Society* 88 (1913), pp. 428–438. DOI: `10.1098/rspa.1913.00400`. URL: `https://royalsocietypublishing.org/doi/10.1098/rspa.1913.0040`.

[17] Oswaldo Burciaga-Díaz. “Parameters affecting the properties and microstructure of quicklime (CaO)- Activated slag cement pastes”. In: *Cement and Concrete Composites* 103.March (2019), pp. 104–111. ISSN: 09589465. DOI: `10.1016/j.cemconcomp.2019.05.002`.

[18] Jean-Michel Commandre, Sylvain Salvador, and Ange Nzihou. “Reactivity of laboratory and industrial limes”. In: *Chemical Engineering Research and Design* 85 (2008), pp. 473–480. DOI: `10.1205/cherd06200`. URL: `https://hal.archives-ouvertes.fr/hal-01634390`.

[19] Kai Gu et al. “Mechanical and hydration properties of ground granulated blastfurnace slag pastes activated with MgO-CaO mixtures”. In: *Construction and Building Materials* 69 (2014), pp. 101–108. ISSN: 09500618. DOI: `10.1016/j.conbuildmat.2014.07.032`. URL: `http://dx.doi.org/10.1016/j.conbuildmat.2014.07.032`.

[20] Deborah N. Huntzinger and Thomas D. Eatmon. “A life-cycle assessment of Portland cement manufacturing: comparing the traditional process with alternative technologies”. In: *Journal of Cleaner Production* 17.7 (2009), pp. 668–675. ISSN: 09596526. DOI: `10.1016/j.jclepro.2008.04.007`. URL: `http://dx.doi.org/10.1016/j.jclepro.2008.04.007`.

[21] Yeonung Jeong et al. “Influence of slag characteristics on strength development and reaction products in a CaO-activated slag system”. In: *Cement and Concrete Composites* 72 (2016), pp. 155–167. ISSN: 09589465. DOI: `10.1016/j.cemconcomp.2016.06.005`. URL: `http://dx.doi.org/10.1016/j.cemconcomp.2016.06.005`.

[22] Fei Jin, Adel Abdollahzadeh, and Abir Al-Tabbaa. “Effect of different MgO on the hydration of MgO-activated granulated ground blastfurnace slag paste”. In: *Third International Conference Sustainable Construction Materials and Technologies*. Vol. 2013-Augus. 2013, pp. 1–10.

[23] Fei Jin, Kai Gu, and Abir Al-Tabbaa. “Strength and hydration properties of reactive MgO-activated ground granulated blastfurnace slag paste”. In: *Cement and Concrete Composites* 57 (2015), pp. 8–16. ISSN: 09589465. DOI: `10.1016/j.cemconcomp.2014.10.007`. URL: `http://dx.doi.org/10.1016/j.cemconcomp.2014.10.007`.

[24] Min Sik Kim et al. "Use of CaO as an activator for producing a price-competitive non-cement structural binder using ground granulated blast furnace slag". In: *Cement and Concrete Research* 54 (2013), pp. 208–214. ISSN: 00088846. DOI: `10.1016/j.cemconres.2013.09.011`. URL: `http://dx.doi.org/10.1016/j.cemconres.2013.09.011`.

[25] Yiliang Liu et al. "Research Progress on Controlled Low-Strength Materials: Metallurgical Waste Slag as Cementitious Materials". In: *Materials* 15.3 (2022), pp. 1–35. ISSN: 19961944. DOI: `10.3390/ma15030727`.

[26] Tianshi Lu, Zhenming Li, and Klaas van Breugel. "Modelling of autogenous shrinkage of hardening cement paste". In: *Construction and Building Materials* 264 (2020), p. 120708. ISSN: 09500618. DOI: `10.1016/j.conbuildmat.2020.120708`. URL: `https://doi.org/10.1016/j.conbuildmat.2020.120708`.

[27] Nabilla Mohamad et al. "Environmental impact of cement production and Solutions: A review". In: *Materials Today: Proceedings* 48.xxxx (2021), pp. 741–746. ISSN: 22147853. DOI: `10.1016/j.matpr.2021.02.212`. URL: `https://doi.org/10.1016/j.matpr.2021.02.212`.

[28] L. Moretti and S. Caro. "Critical analysis of the Life Cycle Assessment of the Italian cement industry". In: *Journal of Cleaner Production* 152 (2017), pp. 198–210. ISSN: 09596526. DOI: `10.1016/j.jclepro.2017.03.136`. URL: `http://dx.doi.org/10.1016/j.jclepro.2017.03.136`.

[29] Solmoi Park et al. "Hydration kinetics and products of MgO-activated blast furnace slag". In: *Construction and Building Materials* 249 (2020), p. 118700. ISSN: 09500618. DOI: `10.1016/j.conbuildmat.2020.118700`. URL: `https://doi.org/10.1016/j.conbuildmat.2020.118700`.

[30] Nicolas Robeyst, Elke Gruyaert, and Nele De Belie. "Ultrasonic monitoring of setting and hardening behaviour of concrete and mortar with blast furnace slag cement". In: *Chemistry of Cement, 12th International congress, Proceedings*. 12th International Congress on the Chemistry of Cement (Montreal). Ed. by Lirias. 2007.

[31] Joonho Seo et al. "Effect of CaO incorporation on the microstructure and autogenous shrinkage of ternary blend Portland cement-slag-silica fume". In: *Construction and Building Materials* 249 (2020). ISSN: 09500618. DOI: `10.1016/j.conbuildmat.2020.118691`.

[32] Roy Trittschack, Bernard Grobéty, and Pierre Brodard. "Kinetics of the chrysotile and brucite dehydroxylation reaction: A combined non-isothermal/isothermal thermogravimetric analysis and high-temperature X-ray powder diffraction study". In: *Physics and Chemistry of Minerals* 41.3 (2014), pp. 197–214. ISSN: 03421791. DOI: `10.1007/s00269-013-0638-9`.

[33] Lianyong Wang et al. "Flight dynamics and sensible heat recovery of granulated blast furnace slag". In: *Open Fuels and Energy Science Journal* 8 (2015), pp. 356–360. ISSN: 1876973X. DOI: `10.2174/1876973X01508010356`.

[34] Shao Dong Wang and Karen L. Scrivener. "Hydration products of alkali activated slag cement". In: *Cement and Concrete Research* 25.3 (1995), pp. 561–571. ISSN: 00088846. DOI: `10.1016/0008-8846(95)00045-E`.

[35] Frank Winnefeld et al. “Influence of slag composition on the hydration of alkali-activated slags”. In: *Journal of Sustainable Cement-Based Materials* 4.2 (2014), pp. 85–100. ISSN: 21650381. DOI: 10.1080/21650373.2014.955550.

PhD and Master Thesis

[36] Zineb Bajja. “Influence de la microstructure sur le transport diffusif des pâtes, mortiers et bétons à base de CEMI avec ajout de fumée de silice”. Unversité Paris-Saclay, 2017.

[37] Ellina Bernard. “Magnesium Silicate Hydrate (M-S-H-) characterization: temperature, calcium, aluminium and alkali”. Phd thesis. Université Bourgogne Franche-Comté, Nov. 2017.

[38] William Hunnicut. “Characterization of Calcium-Silicate-Hydrate and Calcium-Alumino-Silicate-Hydrate”. Phd thesis. University of Illinois, Urbana-Champaign, Aug. 2013.

[39] Zhenming Li. “Autogenous shrinkage of alkali-activated slag and fly ash materials : From mechanism to mitigating strategies Master of Engineering in Structural Engineering”. 2021. ISBN: 9789464212792.

INSA Rennes Teaching Material

[40] Cyr Martin. *Identifiation des minéraux.* Book chapter. June 2013.

[41] Laurent Molez. *BVII - Comportement du Béton Durci.* Teaching material INSA Rennes. 2015.

Online Resources

[42] *Bragg’s law.* URL: https://en.wikipedia.org/wiki/Bragg%27s_law.

[43] *Calcium carbonate, calcite ($CaCO_3$.* URL: http://www.matweb.com/search/datasheet_print.aspx?matguid=bea4bfa9c8bd462093d50da5eebe78ac.

[44] *Calcium dihdroxide.* URL: https://webbook.nist.gov/cgi/cbook.cgi?ID=C1305620&Mask=FFF&Type=JANAFG&Table=on#JANAFG.

[45] *Calcium oxide.* URL: https://webbook.nist.gov/cgi/cbook.cgi?ID=C1305788&Type=JANAFS&Table=on#JANAFS.

[46] *Calcium Oxyde.* URL: https://en.wikipedia.org/wiki/Calcium_oxide.

[47] *Ground granulated blast furnace slag.* URL: https://ibmd.tatasteel.com/index.php/products/granulated-blast-furnace-slag/.

[48] *Magnesium hydroxide.* URL: https://en.wikipedia.org/wiki/Magnesium_hydroxide#:~:text=Magnesium\%20hydroxide\%20is\%20the\%20inorganic,such\%20as\%20milk\%20of\%20magnesia..

[49] *Magnesium oxide.* URL: https://webbook.nist.gov/cgi/inchi?ID=C1309484&Type=JANAFS&Table=on#JANAFS.

[50] *Powder diffraction.* URL: https://en.wikipedia.org/wiki/Powder_diffraction.

[51] *Properties of water.* URL: `https://en.wikipedia.org/wiki/Properties_of_water`.

[52] *Quicklime.* URL: `https://smamineral.se/en/product/quicklime/#:~:text=Quicklime%20is%20produced%20by%20heating,milled%20to%20the%20appropriate%20fraction.`.

Standards

[53] *NF EN 12350-1. Méthode d'essai pour béton frais - Prélèvement et appareillage commun.* Norm AFNOR. 2019.

[54] *NF EN 12390-13. Essais pour béton durci - Détermination du module sécant d'élasticité en compression.* Norm AFNOR. 2021.

[55] *NF EN 12504-4. Essais pour béton dans les structures - Détérmination de la vitesse de propagation des ultrasons.* Norm AFNOR. 2021.

[56] *NF EN 196-1. Méthode d'essai des ciments - Détermination des résistances mécaniques.* Norm AFNOR. 2006.

[57] *NF EN 197-1. Cement - Composition, specifications and conformity criteria for common cements.* Norm AFNOR. 2012.

[58] *NF EN 206/CN. Béton - Spécification, performance, production et conformité - Complément national à la norm NF EN 206.* Norm AFNOR. 2014.

[59] *NF P 18-459. Essai pour béton durci - Essai de porosité et de masse volumique.* Norm AFNOR. 2010.